VELOCITY PLUME PROFILES FOR HALL THRUSTERS USING LASER DIAGNOSTICS

THESIS

Daniel B. Lee, Captain, USAF

AFIT/GA/ENY/10-J01

DEPARTMENT OF THE AIR FORCE
AIR UNIVERSITY

AIR FORCE INSTITUTE OF TECHNOLOGY

Wright-Patterson Air Force Base, Ohio

AFIT/GA/ENY/10-J01

VELOCITY PLUME PROFILES FOR HALL THRUSTERS USING LASER DIAGNOSTICS

THESIS

Presented to the Faculty

Department of Aeronautics and Astronautics

Graduate School of Engineering and Management

Air Force Institute of Technology

Air University

Air Education and Training Command

In Partial Fulfillment of the Requirements for the

Degree of Master of Science in Aeronautical Engineering

Daniel B. Lee, BS

Captain, USAF

June 2010

AFIT/GA/ENY/10-J01

VELOCITY PLUME PROFILES FOR HALL THRUSTERS USING LASER DIAGNOSTICS

Daniel B. Lee, BS

Captain, USAF

Approved:

_____	_____
Richard D. Branam, Lt Col, USAF (Chairman)	Date
_____	_____
Carl R. Hartsfield, Lt Col, USAF (Member)	Date
_____	_____
Richard E. Huffman, Lt Col, USAF (Member)	Date
_____	_____
Dr. William A. Hargus III (Member)	Date

Abstract

This research built a non-intrusive laser diagnostic tool using Laser Induced Fluorescence (LIF) and absorption techniques to measure the velocity and density plume profiles of low powered Hall thrusters. This tool was then applied to a Busek 200W Hall thruster to validate the performance against previous research on the same thruster. A laser frequency sweep through 834.72 nm produced LIF signals for ionized xenon – collected at 541.9 nm – in the thruster plume and absorption data outside the plume at a neutral transition at 834.68 nm. The absorption data provided a baseline reference to calculate the axial and radially velocity of the ions in the thruster plume using the Doppler shift. Initial results compared favorably to published values.

Acknowledgements

First and foremost, I would like to thank my wife and children for putting up with the long hours holed up at AFIT and in the basement. They provided me the motivation to complete the program while keeping me sane. I would like to thank Dr. Hargus at AFRL/RZ who always had the right suggestions whenever I hit a roadblock. The ENY techs, especially Wilbur Lacy and John Hixenbaugh, ensured the equipment and SPASS lab ran smoothly – even after I broke a few items – and Greg Smith of ENP provided a world of insight into lasers, optics and electronic equipment used. And for the mentoring, troubleshooting, and loose purse strings – again, broken items – thanks to LtCol Branam even though he first "Branamed" me one month into AFIT after suggesting this thesis topic with the following, "Oh this topic is easy, all you need is this lamp and new laser…." He never realized how close „Heidi' (the new laser) came to playing the role of printer in my version of "Office Space."

D. Bruce Lee

Table of Contents

Page

List of Figures

Page

List of Tables

Page

Nomenclature

F	Force (Newton)
m	Mass (kg)
q	Electric charge (coulombs)
E	Electric field (V/m)
v	Velocity (m/s)
B	Magnetic field (Tesla)
w	Larmor or cyclotron frequency (Hz)
r_L	Larmor radius (m)
J	Current density (A/m^2)
A	Constant for emission current density (ideally 120 A/cm^2K^2)
T	Temperature (K)
k	Boltzman constant (1.3806504E-23 J/K)
φ,	Work function (eV)
N_i	Ion number density ($\#/m^3$)
N_e	Electron number density ($\#/m^3$)
T_e	Electron temperature (K)
e	Electron charge (1.602176487E-19 C)
κ	Constant for current density (ideally 0.5)
φ_{eff}	Work function due to Schottky effect
ε_0	Permittivity of free space (F/m)
ΔE	Change in energy (J)
E_2	Higher Energy Level
E_1	Lower Energy Level
f	Frequency of electromagnetic radiation (Hz)
h	Planks Constant (7.135E-15 eV-s)
c	Speed of Light (299,792,458 m/s)
λ	Wavelength of electromagnetic radiation
I_o	Reference laser beam intensity

I_t	Beam intensity after absorption
L	Path length (m)
N_i	Number density of the atoms (#/m^3)
σ_{abs}	Cross-sectional area for absorption (m^2)
A_{21}	Einstein coefficient for spontaneous emission (s^{-1})
g_i	Degeneracy terms
N_i	Number density of the atoms (#/m^3)
B_{12}	Einstein coefficient for simulated absorption (s^{-1})
B_{21}	Einstein coefficient for simulated emission (s^{-1})
Δf	Change in frequency (Hz)
f_o	Original frequency (Hz)
Δf_{FWHM}	Full width at half maximum (Hz)
T	Thrust (Newton)
m_p	Mass of propellant (kg)
$\dot{m}_p$	Mass flow rate of propellant (kg/s)
v_{ex}	Velocity of gas at thruster exit (m/s)
v_i	Ion velocity (m/s)
V_b	Beam Voltage (volts)
M	Mass of the ions (kg)
I_b	Beam current (A)
θ	Divergence average half-angle
v_{axial}	Ion velocity in the axial direction (m/s)
$v_{radiall}$	Ion velocity perpendicular to axial direction (m/s)
N_{tot}	Total number density (#/m^3)
A_e	Area of discharge chamber exit (m^2)
N_N	Neutral number density (#/m^3)
N_{++}	Double ionized number density (#/m^3)
I_{sp}	Specific Impulse (seconds)
g_0	Standard gravity constant (9.81 m/s^2)
Δv	Total velocity change (m/s)

m_f	Full mass of satellite with propellant (kg)
m_e	Empty mass of satellite without propellant (kg)
η_T	Overall efficiency
P_{in}	Input power (W)
P_K	Keeper power (W)
P_A	Anode power (W)
P_M	Magnet power (W)
FSR	Free Spectral Range (GHz)
d	Separation distance of mirrors in etalon (m)
V_{psd}	Amplitude of the DC signal (V)
V_{sig}	Amplitude of input signal (V)
V_L	Amplitude of reference signal (V)
θ_{sig}	Phase of input signal
θ_{ref}	Phase of lock-in reference
$f/\#$	Focal ratio or flux density of light
f	Focal length of lens (m)
D	Lens diameter (m)
S_1	Distance of object lens (m)
S_2	Distance of image from lens (m)
NA	Numerical Aperture
n_f	Index of refraction for fiber core
n_c	Index of refraction for cladding wrapped around fiber core
θ_{max}	Acceptance angle of fiber optics
$b.f.l.$	Back focal length (m)
d	Distance between lens (m)
f_1	Focal length of lens closest to object (m)
f_2	Focal length of lens closest to image (m)
d	Grating spacing
α	Angle between grating normal and incident light
β	Angle between grating normal and reflecting light

m	Diffraction order
L	Length between diode laser facets (m)
N	Integer number denoting mode of diode laser
λ_N	Wavelength of diode laser mode
σ	Statistical error variance
A	Multiplier from Student-t distribution
σ_n	Variance of sample
$\Delta v_{\cdot}$	Bias of the diagnostic tool
n	Sample size
n_{air}	Index of refraction for air
λ_{air}	Wavelength in air

VELOCITY PLUME PROFILES FOR HALL THRUSTERS USING LASER DIAGNOSTICS

I. Introduction

Motivation

In 1993, a US Government structured program, the Integrated High-Payoff Rocket Propulsion Technology (IHPRPT), set its sights on doubling US rocket capacity by 2010 [1]. The Department of Defense (DOD), NASA, universities and private industry worked together to establish the goals of IHPRPT; to reduce launch costs and improve performance and reliability across all propulsion formats including boost, orbit transfer, spacecraft and tactical propulsion.

This research will focus on spacecraft electric propulsion (EP), specifically, the Hall Effect Thruster. The IHPRPT payoff for improved spacecraft propulsion hopes to extend the life expectancy by 45%, increase the satellite size by 45% or improve the repositioning capability by 500%. The Russians have flown over 140 Hall thrusters since 1971 [2]. Several European built satellites have used these Russian thrusters. American companies are starting to produce indigenous thrusters and flying them on DOD satellites. The Busek BHT-200 (200W) thruster is the first US produced system flown in space [3]. Aerojet is space qualifying their BPT-4000, 4.5kW thruster for Advanced EHF and NASA missions [4-5]. These Hall thrusters will provide propulsion for orbit transfer from a LEO to GEO orbit, North-South Station Keeping (NSSK) and potentially deep space exploration missions.

The appropriate selection of the EP type to meet mission requirements depends on three main performance characteristics, thrust, specific impulse and efficiency. Another consideration is durability; the thruster lifetime must exceed the expected mission lifetime.

Problem Statement

Many techniques used to measure the plasma plume emanating from the Hall thruster require a probe to be inserted into the plume. These intrusive probes interact with the plasma altering the data collected. Other non-intrusive instruments using microwaves or thrust stands do not afford detailed spatial resolution or characteristics of the plume. Laser Induced Fluoresce (LIF) provides a technique to non-intrusively characterize the particle velocities in the plasma, which in turn, provides basic performance measurements of the Hall thruster.

With the ability to characterize Hall thruster metrics, one can investigate different aspects of improving the thruster lifetime, design, and performance. One consideration for thruster lifetime is the durability of the hollow cathode. Current cathode inserts are made with impregnated tungsten, which is susceptible to poisoning from water vapor and oxygen. In addition, tungsten inserts have a lifetime limited by the evaporation rate dependent on the impregnate evaporation rate. Cathode inserts made with alternate materials have demonstrated more robustness and longer operating times than tungsten inserts but require more energy to produce electrons. It is unknown if replacing the cathode inserts will have an effect on performance and efficiency.

Another important consideration is real estate and weight on a satellite is very limited. Any incremental gains by integrating and packaging the propulsion subsystem can relieve restrictions on other areas of the satellite. The same applies to improving propulsion performance and efficiency; increases will save on mass and power requirements.

Research Objectives

The objectives of this research are:

1. Complete the construction of a LIF set-up and baseline this diagnostic tool to previously tested 200W Hall thruster profiles.
2. Adapt the tool to measure absorption within the plasma by neutral and singly ionized xenon.
3. Map the velocity profile of a 1500 W thruster using different cathode placements and inserts.
4. Compare the 1500 W thruster performance measurements with data previously collected using intrusive probes

Research Focus

The primary focus of this research is to complete the laser diagnostic tool allowing for non-intrusive measurements of the Hall thruster plasma plume while using xenon as a propellant. Also of importance is to document all the procedures and lessons learned while developing this tool as to provide a reference for future users of this technique.

After completing the tool, it needs to be validated by collecting data on a baseline thruster. The tool will characterize a 200W thruster already mapped out through previous research to compare accuracy and limitations of the tool.

Finally, the tool will be used to interrogate the plume profile of a thruster, a Busek 1500W thruster, which has not been mapped previously. Different cathode inserts will be used and the cathode will be placed in different locations to study its influence of the plasma plume. The data collected will be compared to previous data collected at AFIT using different diagnostic tools.

Investigative Questions

The primary question for this experiment is: will this diagnostic tool be able to determine velocity information on the Hall thruster using LIF and the Doppler shift? How will these results compare to other research using the same technique? Also, will the absorption data collected determine neutral and singly ionized density population? Once this tool is validated, the tool can be employed in other thrusters to test cathode insert material and placement. Finally, similar data has been collected using intrusive probes; how will the data collected by two different techniques, one intrusive, the other non-intrusive, correlate?

II. Literature Review

Electromagnetic Force

EP thrust generation starts with the Lorentz force

$$\vec{F} = m\frac{d\vec{v}}{dt} = q\ \ \vec{E} + \vec{v} \times \vec{B} \tag{1}$$

where *F* is the force in Newtons, *m* the mass of the ion or electron, *v* the instantaneous velocity of the particles in m/s, *q* the electric charge in coulombs, *E* the electric field in volts per meter, and *B* the magnetic field in Tesla [6]. This equation breaks down into components to determine how a change in the *E* or *B* affects the force.

Constant Electric Field in the Absence of Magnetic Field (E≠0, B=0)

In the absence of a magnetic field, the Lorentz equation simplifies to

$$\vec{F} = m\frac{d\vec{v}}{dt} = q\vec{E} \tag{2}$$

The force generated is proportional to the strength of the electric field and the particle's charge and is directed parallel to the electric field depending on the polarity of the particle, positive or negative.

Constant Magnetic Field in the Absence of Electric Field (B≠0, E=0)

Setting *E=0* reduces the Lorentz equation into

$$\vec{F} = m\frac{d\vec{v}}{dt} = q\left(\vec{v} \times \vec{B}\right) \tag{3}$$

The velocity components can be expressed as parallel and perpendicular component in relation to the magnetic field. The cross product makes $\frac{dv}{dt}$ and $\vec{B}$ orthogonal to each other. The magnetic field does not perform work on the particle, so any acceleration parallel to the field is zero. Therefore, only a particle's velocity component perpendicular to the magnetic field contributes to the particle's acceleration [6].

$$\frac{d\vec{v}_{\parallel}}{dt} = 0 \tag{4}$$

$$\frac{d\vec{v}_{\perp}}{dt} = \frac{q}{m}\ \vec{v}_{\perp} \times \vec{B} \tag{5}$$

Applying a magnetic field in the B_z direction, equation(5) divides into [6]:

$$F_x = m\frac{dv_x}{dt} = qBv_y \tag{6}$$

$$F_y = m\frac{dv_y}{dt} = -qBv_x \tag{7}$$

$$F_z = m\frac{dv_z}{dt} = 0 \tag{8}$$

Performing an equation of motion analysis and simplifying, these forces results in a harmonic, circular motion with frequency of motion ω, known as the Larmor or cyclotron frequency, equal to equation (9) and shown in Figure 1 [6-7].

$$\omega = \frac{|q|B}{m} \tag{9}$$

The radius of the oscillatory motion is the Larmor radius and defines the frequency of oscillation and the perpendicular velocity [6].

$$r_L = \frac{v_\perp}{\omega} = \frac{mv_\perp}{|q|B} \tag{10}$$

Positively charged particles rotate clockwise around the magnetic field lines and negatively charged particles rotate counterclockwise. If the particle originally has a v_z component, the particle moves with the magnetic lines in a helix motion.

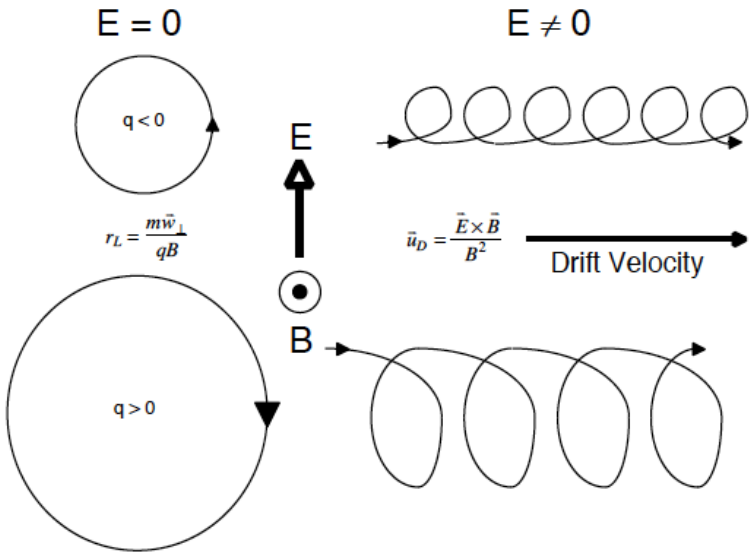

Figure 1. Larmor Radius and Drift Velocity [7].

Constant Electric and Magnetic Field (E≠0, B≠0)

For a general simplified case, consider constant electric and magnetic fields orthogonal to each other. The particle continues to oscillate around the magnetic lines but the electric field alters the particles motion. If a positively charged particle has a velocity component along the electric field, the electric field accelerates and contributes more kinetic energy to the particle. This behavior increases $v_\perp$ and therefore, the r_L. Eventually, oscillation causes the particle to travel against the electric field, decreasing the kinetic energy, $v_\perp$ and r_L. This resulting motion, as seen in Figure 1, is called the drift

velocity. The drift velocity travels along the **E** × **B** direction, regardless of particle polarity equal to equation (11) [6].

$$\vec{v}_{Drift} = \frac{\vec{E} \times \vec{B}}{B^2} \tag{11}$$

Hall Thruster

A typical Hall thruster, shown in Figure 2, is a shallow cylindrical thruster with a coaxial annular dielectric cavity. The enclosed upstream end consists of an annular anode and propellant injection into the chamber. Electromagnets, outside the cylinder and inside along the central axis, create radial magnetic field lines within the thruster chamber. A negatively biased external hollow cathode provides the electrons and is located near the opening downstream end. The positive-biased anode inside the chamber attracts the electrons. The electrons migrate upstream to the anode, creating an electric field parallel to the axis of the thruster within the chamber.

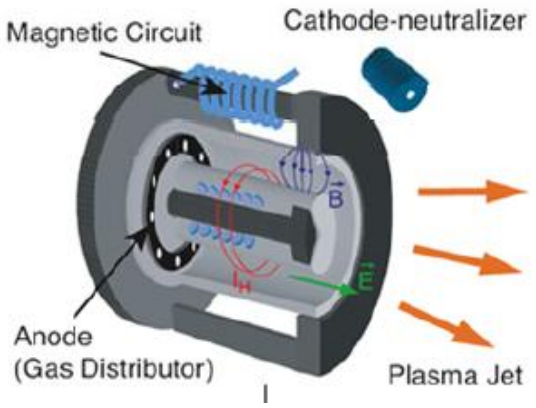

Figure 2. Cutaway Picture of a Hall Thruster [8].

As the electrons enter the channel, they encounter radial magnetic lines. The magnetic forces change the electron path of travel and start spiraling around the magnetic

field lines. With the addition of an electric field, the electrons start to drift azimuthally around the cylinder as shown in Figure 3 where the electric field is aligned with the x-axis, the magnetic field along the r-axis and the drift following the E×B direction. The rotation of the electrons around the cylinder is also known as the Hall current. This is how the thruster received its name. In addition, Hall thrusters are referred as closed-drift thrusters.

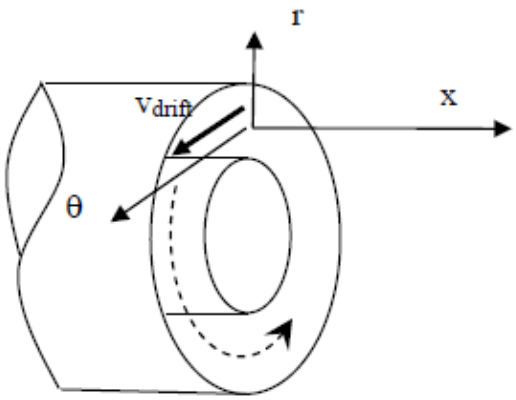

Figure 3. Azimuthal Drift in Hall Thruster [6].

The gaseous propellant passes through a diffuser to spread evenly throughout the thruster chamber. The neutral propellant does not interact with either the electric field of magnetic lines until the electrons trapped in the magnetic field ionize them. Once ionized, the Lorentz force accelerates the positively charged ions to high velocities along the electric field lines and out the chamber, creating thrust. The magnetic fields do not affect the ions as the larger mass ensures an ion Larmor radius larger than the channel length of the thruster [7]. On the other hand, the depth of the channel must be larger than the electron Larmor radius or the electrons will reach the anode before the electrons have a chance to ionize any of the propellant.

The electrons eventually migrate to the anode and are collected. The power supply adds power and cycles the electrons to the hollow cathode. The hollow cathode requires about 10% of the propellant to create electrons. Only a small portion of the cathode electrons enters the chamber. The majority of the electrons combine with the positive ions downstream to form neutral plasma.

Hollow Cathode

Cathodes provide the electrons required by the Hall thruster to ionize the propellant within the thruster chamber and neutralize the plasma downstream. Several types of cathodes have been employed to satisfy this system requirement. The simplest is a wire, i.e. tungsten filament, passing a current until it heats up and starts emitting electrons. This cathode was last used for space applications in the 1960s due to the high temperatures required for electron emissions, which resulted in short lifetimes from evaporation and sputter erosion [2].

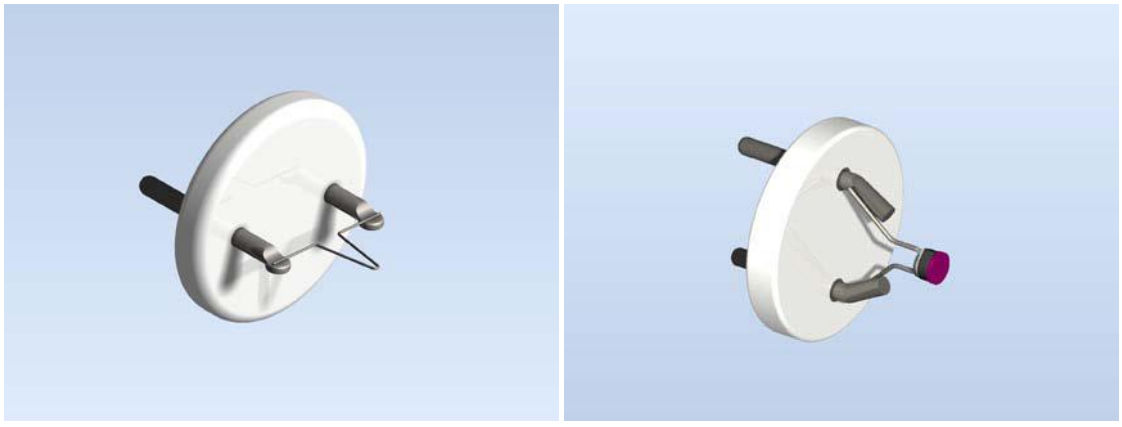

Figure 4. Tungsten Filament Cathode (l) and LaB_6 Single Crystal Emitter (r) [12].

Another cathode is the single crystal emitter, widely used in electron microscopes, lithography and electron beam welding [9]. Common crystals include lanthanum-

hexaboride (LaB_6) and cerium-hexaboride (CeB_6) [10]. Studies are considering these cathodes for a miniature EP thruster [11].

Both of these cathodes employ Ohmic heating to release the electrons. The Richardson–Dushman equation describes the emission current density, J, in equation (12)

$$J = AT^2 e^{\frac{-q\phi}{kT}} \tag{12}$$

where A is, ideally, a constant with a value of 120 A/cm^{2}K^2, T, the temperature in K, q, the charge, k, Boltzmann's constant and φ, the work function in eV [2]. The work function is a material characteristic property and the energy required to liberate an electron from the surface of a solid. For example, the work functions for tungsten, LaB_6 and CeB_6 are 4.5, 2.70 and 2.62 eV, respectively [11]. According to equation (12), tungsten's higher work function requires a higher temperature and more power in order to achieve the same emission current density as LaB_6 or CeB_6.

Current cathodes used with EP are the hollow cathode design. An upper bound of the maximum electron current density exists due to the physics of the plasma. The current emission may be "space charge limited" instead of thermally limited due to a double-sheath cathode; when two plasmas are in contact but at different potentials. The current emission is then best described using equation (13) [14].

$$J_e = \frac{\kappa}{2} N_i e \sqrt{\frac{kT_e}{m}} \propto \frac{1}{4} N_e e \sqrt{\frac{kT_e}{m}} \tag{13}$$

The current density depends on the ion density, N_i, as well as the electron temperature, T_e. The constant κ is usually about 0.5.

How a Hollow Cathode Operates

A common hollow cathode design is the orificed hollow cathode. This design consists of a hollow refractory tube capped by an orifice plate. The orifice plate is a simple disk with a hole in the center, sized to optimize temperatures to accommodate both stable operation and long life [15]. Inside the tube and next to the orifice is a cylindrical shaped insert. The inner surface material has a low work function, as this portion contacts the plasma. A heater filament wraps around the insert. Foil made of refractory metal, such as tantalum, surrounds the assembly to increase the heat transferred to the insert, reducing the radiative losses.

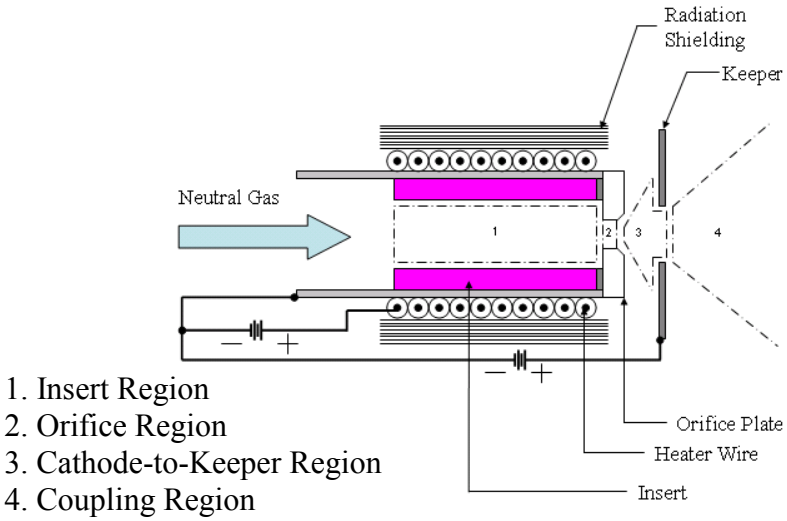

Figure 5. Orificed Hollow Cathode [16].

Instead of using Ohmic heating to release electrons, the filament externally heats the insert to the required temperatures for electron emissions. A neutral gas flows into the insert region and the high temperatures transition it into plasma. Electrons emitted from the insert ionize the plasma creating more electrons. A positively biased and

electrically isolated electrode, the keeper, encases the foil-wrapped assembly. The keeper attracts the electrons from this plasma through the orifice. This process establishes an electric field within the insert region creating a phenomenon known as the Schottky effect. The Schottky effect lowers the work function of the insert material as shown in equation (14)

$$\phi_{eff} = \phi - \sqrt{\frac{q|E|}{4\pi\varepsilon_o}} \tag{14}$$

where ε_0 is the permittivity of free space and E is the strength of the electric field [2].

The keeper merely acts as an anode to the plasma inside. Therefore, the design is kept simple – only requiring an opening for the plasma and electrons to pass through – and fabricated from a conductive material such as metal or graphite. This material is positively biased to attract the electrons.

The simplest of designs is often referred to as an open-geometry cathode or keeper, where the inter-electrode gap between the tube subassembly and the keeper subassembly is radially open [15]. Another design is the enclosed-geometry keeper, where another cylinder is placed over the cathode tube and heater subassemblies encapsulating them as shown in Figure 6 [15]. The downstream end near the orifice plate contains a hole for the plasma and electrons and the upstream portion is open to attach to the base of the cathode. Although more complicated, this design provides for more efficient use of the neutral gas.

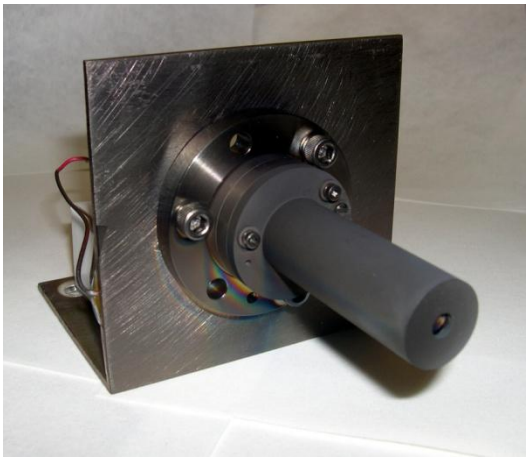

Figure 6. A Hollow Cathode with an Enclosed Geometry Keeper [9].

Once lit, the cathode operates in self-heating mode allowing the user to turn off the heater, saving and improving overall electrical and power efficiency. Three mechanisms contribute to self-heating, (1) orifice heating, (2) ion heating, and (3) electron heating [2]. In orifice heating, a small, restrictive orifice produces a high internal pressure in both the insert and orifice regions. The plasma discharge passing through the orifice is very restrictive. Through convection, a significant amount of power transfers in from orifice plasma to the orifice walls. The walls then conduct and radiate this energy to the insert. Ion heating occurs as the positively charged ions fall through the sheath potential at the insert surface and bombards the insert, generating heat. Finally, high plasma pressures and discharge currents create a Maxwellian distribution of electron energy where the tail of the electron distribution has enough energy to pass through the wall sheath and transfer their energy to the insert. The geometry of the cathode determines heating mechanism that dominates and ultimately, depends on the internal neutral gas pressure in the insert and orifice regions, and the discharge current.

Cathode Insert Materials

The ideal cylindrical insert is made of a material with a low work function with a long operating life. Original inserts were made of pure tungsten but the work function of 4.55 eV required heating to very high temperatures before emitting electrons.

To reduce heating requirements, the tungsten inserts were coated with oxide layers reducing the work function to ~2 eV. Compounds such as barium oxide were deposited on the insert surfaces but ion bombardment quickly depleted these deposits. To improve operating life, inserts were manufactured to be porous and impregnated with oxides such as barium oxide (BaO), calcium oxide (CaO), and aluminum oxide (Al_2O_3) [11]. This technique provided a reservoir of oxide material to continuously resupply the low work function surface layer, increasing the lifetime from tens of hours to thousands compared to surface coated inserts [2].

The main drawback to impregnated tungsten inserts are their susceptibility to poisoning from water vapor and oxygen. These inserts may cease plasma generation if operated in an environment with oxygen partial pressures as low as 10^{-6} torr and water vapor partial pressures of 10^{-5} torr. [18] As the propellant flows directly through, the inserts require "propulsion-grade" propellant of 99.9995% purity, increasing costs.

Current research is turning to other types of materials to fabricate inserts, particularly LaB_6 or CeB_6. These materials have a higher work function then impregnated tungsten requiring higher temperatures to produce the same electron emissions. On the other hand, at the same emission current density, LaB_6 inserts can operate in oxygen partial pressure two orders of magnitude higher than tungsten making them much less susceptible to poisoning permitting use of the crudest grade of xenon

available (99.99% purity) [19]. Compared to tungsten, evaporation rates improve by an order of magnitude, increasing operational lifetime [19-20]. Other research shows CeB_6 with very similar properties to LaB_6 and a longer lifetime than LaB_6 [21-23].

Cathode Placement

Previous studies on high powered Hall thrusters, 8kW, demonstrates improved efficiency when mounting the cathode in the center as opposed to externally, the current method used with Hall thrusters [24]. These studies shows center-mounted cathodes provide a more collimated and symmetric plume. The collimated plume has a smaller divergence; less propellant momentum is directed radially and more aligned with the thruster axis. The symmetric plume leads to less erosion of the discharge chamber, increasing the thruster lifetime. Other research using a 1500W thruster operating at 600W indicates an increase in double and triple ionized xenon, leading to performance loss in efficiency [9].

Theory of Absorption

Take a continuous spectrum of white light and pass it through a prism. The prism spreads the light into the component wavelengths forming a rainbow pattern. Shine the light through a gas comprised of different atoms and molecules before the prism and the rainbow spectrum now contains narrow black lines. These black lines, or spectra lines, are specific wavelengths absorbed by the gas. The wavelengths absorbed are unique characteristic of the component atoms comprising the gas.

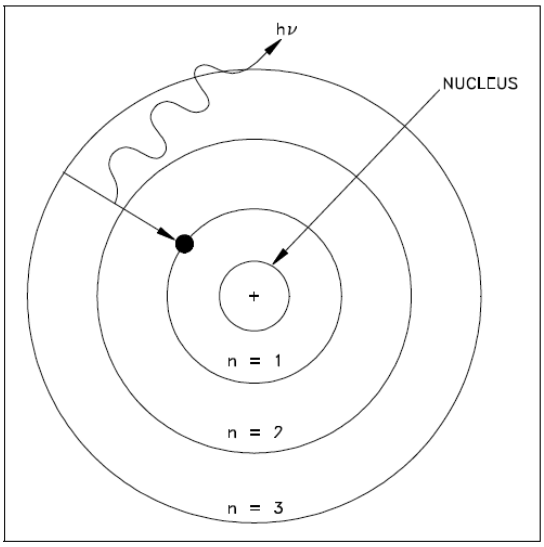

Figure 7. Bohr Model of Hydrogen Electron Releasing a Photon [25].

The Bohr model explains spectral lines for hydrogen atoms. The model approximates hydrogen as a proton at the center with an electron orbiting the proton and everything held together by electrostatic forces. The electron can only reside in fixed atomic orbits and is in the ground state if unexcited. Applying energy at discrete intervals excites the electrons to the next atomic orbit. Eventually the electron frees itself from the atom and the atom becomes ionized. The transition from one state, $E_{1,}$ to another, $E_{2,}$ requires a specific amount of energy, ΔE, per equation (15) [25].

$$\Delta E = E_2 - E_1 \tag{15}$$

Under the dual wave-particle theory, light is characterized as individual photons and waves with various wavelengths. Each photon carries energy, E, dependent on the wavelength according to equation (16) where h is Planck's constant and equals $4.13566733 \times 10^{-15}$ eV-s, f is the photon frequency, c is the speed of light and λ is the wavelength [26].

$$E = hf = \frac{hc}{\lambda} \tag{16}$$

When the light passes through the hydrogen gas, the gas absorbs certain photons, specifically, those with energy levels matching the energy required to transition an electron from one level to another according to equation (15). The absorbed photons result in the black lines in the rainbow spectrum.

Every atom or molecule has a characteristic set of line spectrums. Absorption can determine the number density of the atoms by passing a laser through the volume of atoms. A laser is a collimated collection of photons at a specific wavelength. When the laser wavelength matches the line spectra of the medium, the atoms absorbs part of the laser, reducing the laser's intensity according to Beer's Law or the Beer-Lambert law for absorption [26].

$$I_t = I_o e^{-\sigma_{abs} l N_i} \tag{17}$$

I_o is the reference laser beam intensity before absorption, I_t is the beam intensity after absorption, l the path length through the absorbing material, N_i the number density of the atoms and σ_{abs} the cross-sectional area for absorption. Equation (18) defines σ_{abs} [26].

$$\sigma_{abs} = \frac{A_{21} c^2}{8\pi f^2} \frac{g_2}{g_1} \tag{18}$$

A_{21} is the Einstein spontaneous emission rate coefficient and g_i is the degeneracy terms related to the transitioning energy levels of the atoms.

Solving for the number density in equation (18) yields equation (19). This equation allows one to experimentally determine the number density of atoms by

comparing the ratio of the reference beam intensity to the laser intensity passing the medium.

$$N_i = \frac{-\ln\left(\frac{I_t}{I_o}\right)}{\sigma_{abs} l} \tag{19}$$

Theory of Laser Induced Fluorescence

When an atom absorbs a photon, it resides in an excited state. Eventually, the electron "relaxes" and drops down to its original state releasing the energy as a photon with wavelength determined by equation (16). This spontaneous emission is also called fluorescence. A laser tuned to the energy difference between the excited states of the electron results in continuous absorption and emission of photons. Unlike absorption, which occurs along the path of the laser, the motion of the atom and electrons causes an even distribution of photons in all directions, 4π steradians.

The Einstein coefficients for simulated absorption, B_{12}, and simulated emission, B_{21}, relate the absorption and emission rates along with the spontaneous emission coefficient, A_{21}. The simulated coefficient only applies in the presence of electromagnetic radiation, i.e. a laser. Equations (20) and (21) relate all three coefficients [27].

$$B_{12} = \frac{g_1}{g_2} B_{21} \tag{20}$$

$$A_{21} = \frac{8\pi h^3}{c^3} B_{21} \tag{21}$$

Simulated emission requires the atom to be in an excited state. A photon then induces the excited atom to release another photon resulting in a net of two photons when the atom returns to the ground state, the basis of a laser.

This tool uses simulated absorption to excite the atoms and observes the spontaneous emissions to measure velocity using the Doppler shift.

Doppler Equation

An excited "stationary" atom emits a photon at a frequency dependent on its energy transition per equation (22). If the atom is moving, the frequency of the fluorescence shifts due to the Doppler effect with the magnitude of the shift dependent on the particles velocity. The change in frequency is described by equation (22)

$$\Delta f = \pm f_o \frac{v}{c} \tag{22}$$

where f_o is the original frequency, v, the velocity of the particle and c, the speed of light [28]. Particles travelling towards the observer increases in frequency and is referred to as a "blue" shift as the higher frequency results in a shorter wavelength compared to the original. The atom moving away produces a "red" shift as the frequency decreases and the wavelength increases. The terms "red" and "blue" shift relates back to the visible spectrum; red light has a longer wavelength than blue light.

Line Spectrums and Transitions

A hydrogen electron can excite to seven states before ionizing. When the electron relaxes, it returns to any of the lower states as shown in Figure 8 emitting a photon with a specific wavelength corresponding to the energy drop. The electrons that transition to the ground state, n = 1, are part of the Lyman series and produce photons in the UV range. Those transitioning to n = 2 are called the Balmer series and produce light in the visible range. Other hydrogen transitions produce different line spectrums in the IR spectrum.

This same principle applies to other atoms allowing for a plethora of transition lines for selection. The NIST Atomic Spectra Database lists the transition lines for different atoms and their ions. In addition to providing the spectra lines, the database identifies the configuration of the transition states and the relative intensity determined by spontaneous emission rate coefficient.

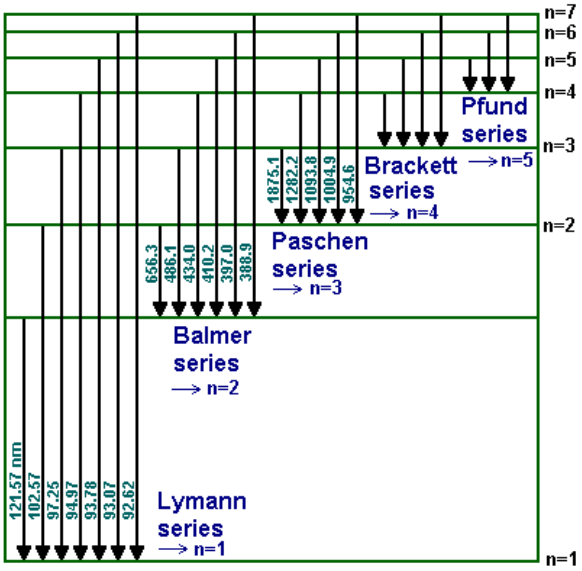

Figure 8. Diagram Listing the Electron Transition for a Hydrogen Atom [29].

This research targets xenon transitions previously used by Manzella and Hargus [7]. A meta-stable neutral transition occurs at 823.162 nm in air from the $6s[3/2]_2^0 - 6p[3/2]_2^0$ transition. A laser tuned at 834.724 nm in air excites the ionic transition of $5d[4]_{7/2} - 6p[3]_{5/2}$ within the thruster plume. Xenon at an upper state of $6p[3]_{5/2}$ also yields a very strong transition line when relaxing to another upper state $6s[3]_{3/2} - 6p[3]_{5/2}$ resulting in fluorescence at 541.9 nm in air. Finally, the neutral transition at 834.682 nm, $6s[1/2]_1^0 - 6p[3/2]_2$ in air provides a stationary reference on the optics tables.

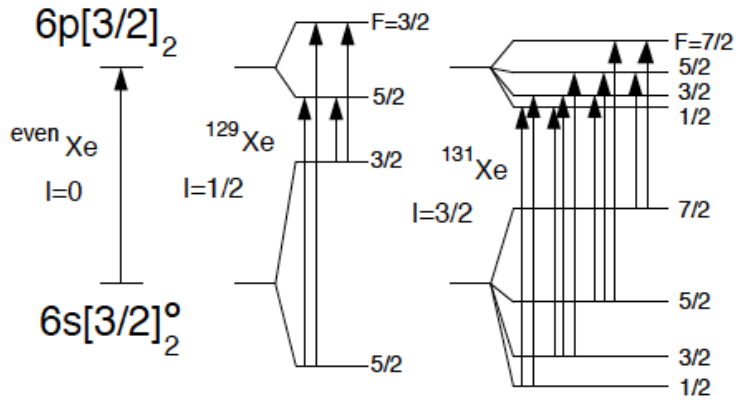

Figure 9. Electron Transitions for Xe^{+} at 834.72 nm [7].

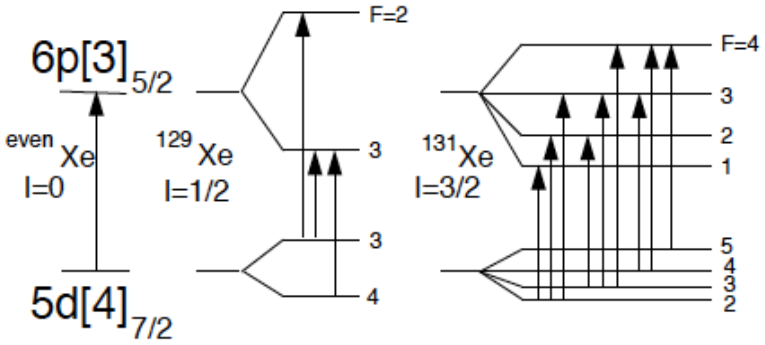

Figure 10. Electron Transitions for Neutral Xenon at 823.18 nm [7].

Hyperfine Splitting

Energy level transitions may divide into sub-levels, a result of hyperfine structure splitting. Hyperfine structure occurs due to the energy from the magnetic interactions of the electrons with nuclear magnetic poles and the nuclear spin caused by the distribution of charge within the nucleus by the protons and neutrons [30]. Elements may have multiple naturally occurring isotopes and the differences in neutrons results in nucleuses with a variety of masses and nuclear charge densities. These combinations lead to small splits in the energy levels, especially if the isotopes contain an odd number of neutrons, and a shift in the line spectrum. This shift is on the orders of MHz in frequency [7].

Figure 11 shows an absorption curve of neutral xenon with multiple absorption peaks due to the naturally occurring isotopes and resulting hyperfine splitting.

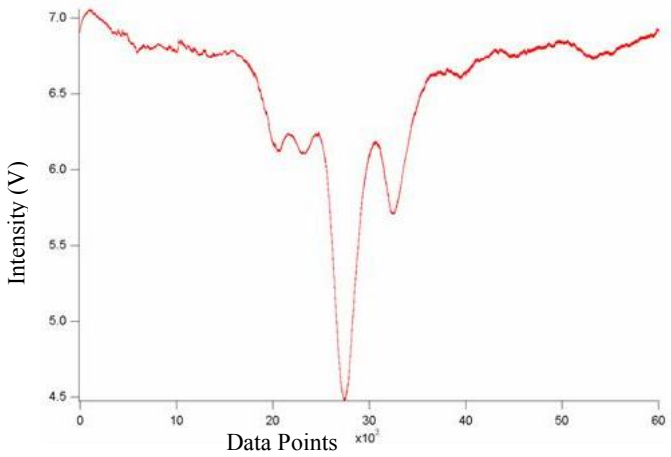

Figure 11. Absorption Curve of Neutral Xenon at 823.16 nm [25].

Line Shapes

A spectra line should be a monochromatic line with a specific wavelength and frequency. In reality, the spectra line comprises a range of frequencies caused by natural broadening. The energy levels of the atoms, collisions and temperature influence the natural line shape.

An excited atom spontaneously decays to its ground state implying an excited atom has a finite natural lifetime. The energy level of each individual atom cannot be determined but the Heisenberg uncertainty principle can explain the spread of energy [30]. Collision broadening or pressure broadening results as atoms or molecules collide, transferring energies between each other. The different energy levels and pressure broadening produce Lorenztian line shapes as shown by the blue curve in Figure 12.

In the low-pressure plasma of the Hall thruster, kinetic temperature of the species plays the largest factor in determining line shape. The thermal motion of the molecules takes on a Maxwellian velocity distribution resulting in a Gaussian line shape as shown by the red curve in Figure 12 [31]. The full width at half maximum (FWHM) characterizes the shape by describing the width of the curve when the intensity is at half the maximum intensity. The FWHM for a purely Doppler line broadened shape is given by equation (23)

$$\Delta f_{FWHM} = \frac{f}{c}\sqrt{\frac{8\ln 2kT_{kin}}{m}} \tag{23}$$

where m is the mass of the molecule, and T_{kin} the kinetic temperature of the molecules [7].

The resulting overall line shape is a convolution of both the Doppler and Lorenztian curves, also known as a Voigt profile. The actual shape depends on the individual curves but the Doppler curve dominates the center while the Lorenztian curve influences the "wings" [30].

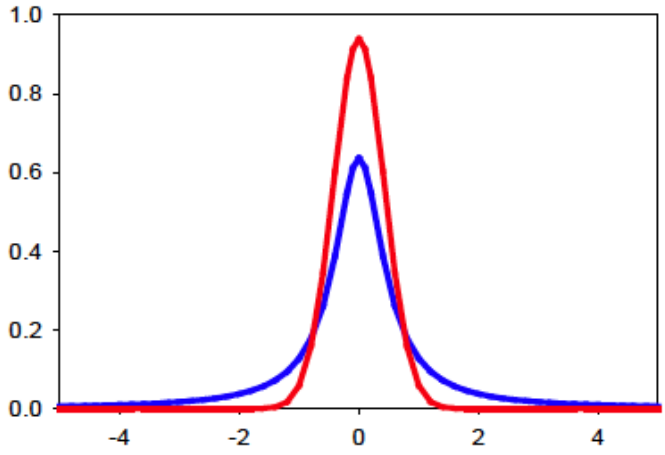

Figure 12. Comparison of Lorenztian (red) and Gaussian (blue) Line Shapes [25].

This line shape will also contribute to velocity error calculations of ±500 m/s. The error results from two main factors, the inability to determine the neutral and ionic transition energies and uncertainty in determining the peak fluorescence of the broadened line shape [32].

Performance Metrics

The major performance metrics for EP devices are thrust, I_{sp} and efficiency. Thrust is the amount of acceleration the thruster can impart on the satellite. I_{sp} is analogous to fuel economy. I_{sp} determines the propellant required to meet the total velocity change needed over the lifetime of the satellite. Efficiency provides an estimate of how well the device uses power and indirectly provides an idea of how much mass the propulsion system will require. Mission needs will ultimately dictate if the performance metrics make the thruster a suitable candidate.

Thrust

Starting with Newton's Second Law, the force, or thrust, onto the satellite by the Hall thruster derives from the momentum rate of change using

$$T = \frac{d}{dt}\ m_p v_{ex}\ = \dot{m}_p v_{ex} \tag{24}$$

where m_p is the mass of the propellant in kg, $\dot{m}_p$ is the mass flow rate in kg/s and v_{ex} the exit velocity of the propellant in m/s [33].

For the Hall thrusters, $v_{ex} \approx v_i$, the ion velocity,

$$v_i = \sqrt{\frac{2qV_b}{M}} \tag{25}$$

where M is the ion mass, q the charge of an electron, and V_b the net voltage through which the ion accelerates [2]. The mass flow rate of the ions is

$$\dot{m}_i = \frac{I_b M}{q} \tag{26}$$

where I_b is the beam current [2].

Substituting v_i and $\dot{m}_i$ into equation (24) yields the theoretical maximum thrust, in Newtons, for a Hall thruster is

$$T = \sqrt{\frac{2M}{e}} I_b \sqrt{V_b} \tag{27}$$

where q replaces one electron charge, e, and equals $1.6\text{x}10^{-19}$ C [2]. This equation applies to a singly ionized, mono-energetic beam of ions traveling in the axial direction and does not account for losses due to due beam divergence, multiple ionization of the propellant or momentum imparted by neutral xenon.

Beam divergence is the angular measurement of the plume as the diameter of the plume increases downstream from the exit plane, forming a conic shape. The divergence equates to a loss in thrust, as the ions do not travel parallel with the thrust axis. Equation (28) quantifies the beam divergence average half-angle, θ

$$\theta = \tan \frac{v_{radial}}{v_{axial}} \tag{28}$$

where v_{axial} is the ion velocity in the axial direction and v_{radial} the ion velocity perpendicular to the axial direction. The v_{radial} accounts for the ion momentum loss not aligned with the thrust axis.

Multiple ionization results in a loss since equation (27) shows doubly ionized velocity increases only by a factor of $\sqrt{2}$ even though it contributes twice to the beam current. Measuring thrust of double ionized requires information on number density.

The total number density includes the neutral, singly ionized and doubly ionized densities while ignoring the contribution from particles with higher ionizations. Absorption data provides the number density for neutral, N_N, and singly ionized, N_+ xenon. The total number density at the thruster face output is

$$N_{tot} = \frac{\frac{\#\text{ of particles}}{s}}{v_{ex} A_e} \tag{29}$$

where A_e is the area of the discharge chamber exit. The velocity is determined using LIF data assuming the average neutral velocity calculated is the same velocity of the propellant entering the system. Equation (30) converts flow rate of SCCM to # of particles per second for xenon [2].

$$1sccm = 4.477962 \times 10^{17} \left[\frac{atoms}{s} \right] = 0.0983009 \left[\frac{mg}{s} \right] \tag{30}$$

Therefore, the doubly ionized number density, N_{++}, is equal to

$$N_{++} = N_T - N_N - N_i \tag{31}$$

The total thrust is the sum of equation (24) applied to the neutral, single and double ionized xenon particles. LIF provides velocity information for neutral and singly ionized particles. Since immeasurable, doubly-charged ion velocity is assumed to increase by $\sqrt{2}$ over the singly ionized velocity particles. Equations (29) and (30) convert the number densities into a flow rate.

Specific Impulse

Specific Impulse (I_{sp}) measures the ratio of the thrust to the propellant used

$$I_{sp} = \frac{T}{\dot{m}_p g_o} \tag{32}$$

where g_o is standard gravity [2]. Dividing by standard gravity standardizes I_{sp} to units of seconds and one can directly compare between propulsion devices regardless if original terms are in SI or metric units. Specific Impulse relates to mission requirements through the ideal rocket equation in Equation (33)

$$\Delta v = I_{sp} g_0 \ln\left(\frac{m_f}{m_e}\right) \tag{33}$$

where Δv is the total velocity change given the ratio of the full mass, m_f, and empty mass, m_e. A higher I_{sp} results in more Δv given the same satellite and propellant mass.

Efficiency

Efficiency provides a measurement for the overall performance. Using historical data, efficiency indicates the propulsion subsystem power requirements and mass when performing "back of the envelope" initial design assessments. Equation (34) provides an overall efficiency equation for all EP thrusters

$$\eta_T = \frac{T^2}{2\dot{m}_p P_{in}} \tag{34}$$

where P_{in} is the input power required to operate the thruster [2]. The input power includes the discharge power and losses by the keeper (P_K), anode (P_A) and magnets (P_M).

$$P_{in} = P_A + P_K + P_M \tag{35}$$

III. Methodology

Facility Set-up

Vacuum Chamber

Testing took place within a vacuum chamber located at the AFIT Space Propulsion Analysis and System Simulation (SPASS) laboratory. The 2.5 m long by 2.0 m diameter stainless steel chamber provides a volume of ~6.5 m^3, numerous feedthroughs and view ports for observing operations within the chamber.

The six 10-inch viewports are located on the sides, doors and top of the chamber. The feedthroughs pass gaseous propellant, electrical power, cooling water, USB adapters, fiber optic cables and the many instruments into the chamber.

A rotary vane mechanical pump, Leybold Trivac D65B, removes air until the pressures reaches approximately 100 millitorr. At this crossover point, the mechanical pump disengages, a valve seals off the chamber and four CVI Torrmaster TM500 cryopumps take over to further reduce chamber pressure. The pump assemblies include air-cooled compressors connected to the cryo-head through flex lines to compress liquid helium and cool the cryo-heads to temperatures of 16-22 K. A Lakeshore Model 211 monitors cryo-head temperatures. The remaining gas molecules in the chamber condense and freeze to the cryo-head, reducing chamber pressure down to 10^{-8} torr. These pumps can handle up to 4,000 l/s of xenon gas per unit for a total chamber pumping speed of 16,000 l/s. The pumping speed accommodates Hall thrusters operating up to 600 W while maintaining pressures below $5x10^{-5}$ torr. In this closed-system, the xenon

propellant accumulates on the cryo-heads reducing pumping capacity over time. This degradation correlates with a rise in cryo-head temperatures.

To increase pumping speeds and decrease pump-down time, the chamber added a CVI Torrmaster TM250 cryopump and CVI Torrmaster CRG012 internal cooled plate. These additions increased overall chamber pumping speed to 20,900 l/s. To decrease the pump-down time, the TM250 has a gate-valve between the chamber and pump, isolating the cryopump from the chamber when closed. When pump-down initiates, a separate roughing pump brings the gate-valve cavity to 100 mTorr much faster than the entire chamber. The TM250 activates and the cryo-head reaches 12 K by the time the main chamber reaches crossover. At crossover, the gate valve opens and the remaining gas molecules freezes onto the TM250, bringing chamber pressure down to 10^{-5} Torr within minutes, well before the four TM500 cryopumps have time to cool.

A Kurt J. Lesker 300 Series Convection vacuum gauge and Extorr XT Series RGA measures the chamber pressure. The Lesker gauge uses a convection-enhanced Pirani gauge to monitor the pressures during the roughing pump. Able to measure atmosphere down to 10^{-4} torr, this gauge sends the signal to the power control box to initiate the switch from the mechanical pump to the cryopumps at crossover.

The Extorr XT Series Residual Gas Analyzer (RGA) model XT100 incorporates three gauges into one integrated unit; a Pirani gauge, a hot cathode ion gauge, and a quadrapole gauge. This gauge measures pressures from atmospheric all the way down to 10^{-11} torr. Extorr's VacuumPlus software controls the RGA and automatically switches between the different gauges based off pressure. In addition, the RGA provides a partial

pressure of the gas species in the vacuum chamber, discriminating by atomic mass as shown in Figure 13 with the peaks labeled by gas type.

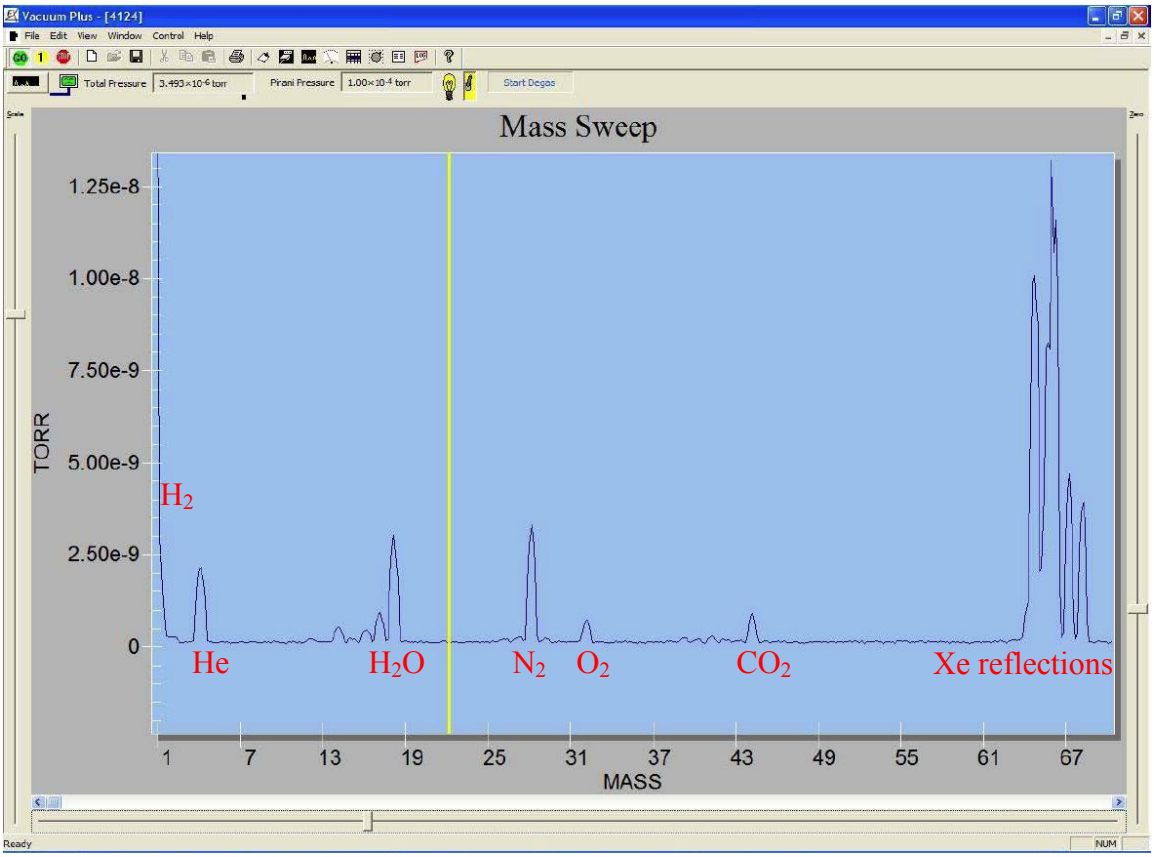

Figure 13. Screenshot of VacuumPlus Software.

A LabVIEW® program records the temperatures from the Lakeshore Model 211 and Lesker vacuum gauge. The data file contains the temperature in K and a voltage from the vacuum gauge. An Excel spreadsheet converts the voltage to a pressure and plots the graphs as seen in Figure 14. For a typical pump-down, crossover occurs after two hours. About 15 minutes pass crossover, pressure reduces to 10^{-5} Torr allowing the start of cathode conditioning, a 3.5 hour process. After ~5.5 hours, the main cryopumps reach operational temperatures of 18-20K and total pressure is at 10^{-7} Torr.

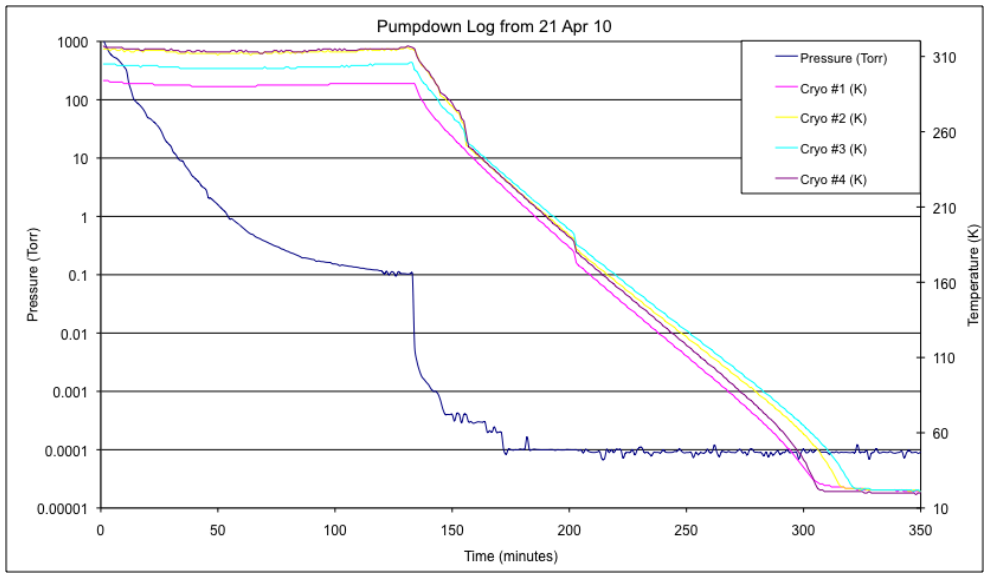

Figure 14. Pumpdown Log Showing Pressure and Cryo-head Temperatures.

Test Assembly

Three independent Aerotech® translation stages provide a 60 cm range sub-millimeter location accuracy in the X-, Y- and Z- axis. This set-up currently has no rotation capability. At start-up, the Aerotech® A3200 software clears the location values regardless of position, requiring independently zeroing of each stage. Attached to the Z-stage is an 80/20® aluminum structure used to hold the thruster, propellants lines and electrical wiring. The design of the box and various mountings must accommodate the translation stage ability to move to a home position.

The thruster mounts to the frame with the axial direction aligned with the X-axis of the chamber and the hollow cathode on the Y-axis. The laser probe beams align parallel to the X-axis and Z-axis for axial and radial measurements, respectively.

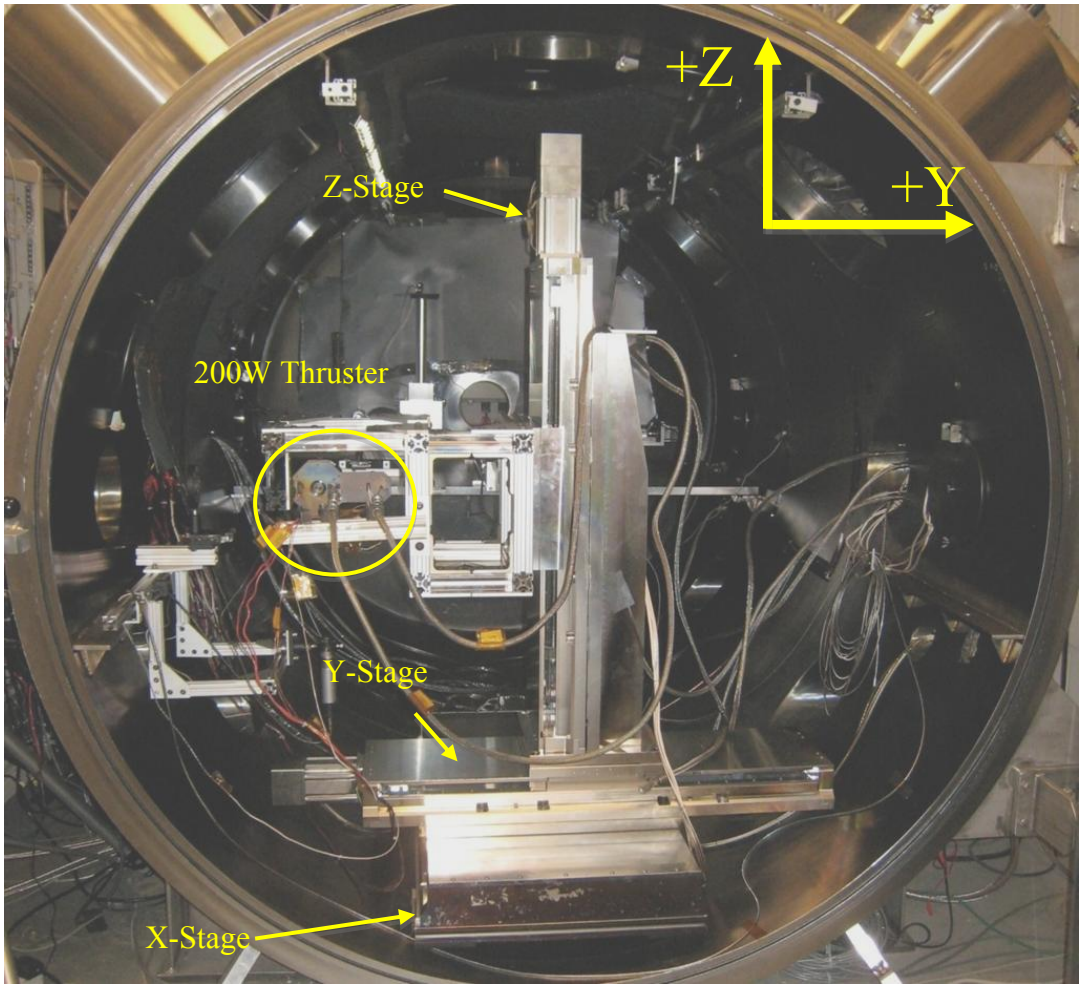

Figure 15. Picture of Translation Stage and Thruster Orientation.

The lab uses propulsion grade xenon at 99.9995% purity and four MKS model 180A flow controllers manage the flow rate. The two controllers provide calibrated flow rates of 0-10 SCCM and 5-50 SCCM of xenon with an accuracy of ≤0.01%. The MKS Type 247 four-channel readout controls the flow rate by adjusting the percentage of SCCM. For instance, the 200W anode ideal setting is 8.54 SCCM, 17.1% of 50 SCCM, so the desired setting is 17.1.

Equipment Used

Hall Thruster

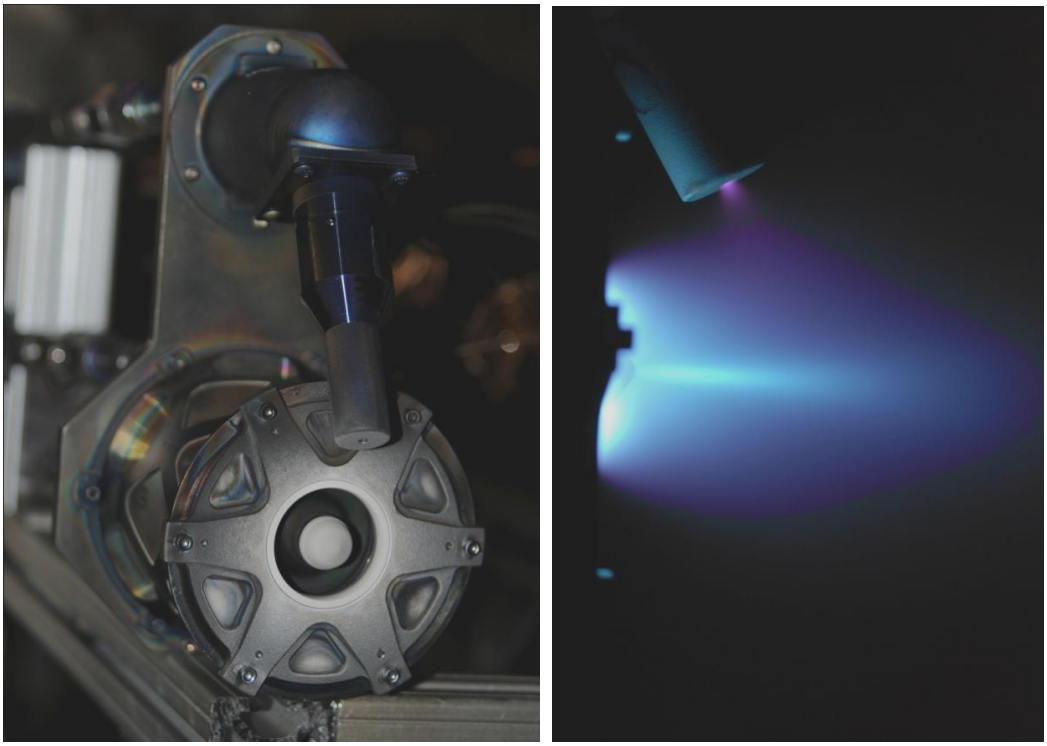

Figure 16. Busek BHT-200 Thruster [40].

Table 1. Nominal Operating Conditions for Busek BHT-200

Anode Flow	840 µg/s (Xe) 8.545 SCCM
Cathode Flow	98 µg/s (Xe) 8.545 SCCM
Anode Potential	250 V
Keeper Current	0.5 A
Magnet Current	1.0 A
Heater Current	0.0 A

The Busek built 200W BHT-200 Hall thruster operates at a discharge voltage and current of 250V and 800mA, respectively. With a propellant mass flow rate of 0.94 mg/sec, this thruster achieves 12.8mN of thrust at an I_{sp} of 1390 seconds with efficiency of 43.5%. The operating conditions for this experiment are listed in Table 1.

Figure 17 shows the coordinate system for data collection. The center point (0,0,0) corresponds to the thruster nose cone tip. The X-axis aligns with the thruster axial velocity. Probing next to the thruster face results in a -X location. The cathode lies on the XY-plane. The radial probe beam is on the Z-axis.

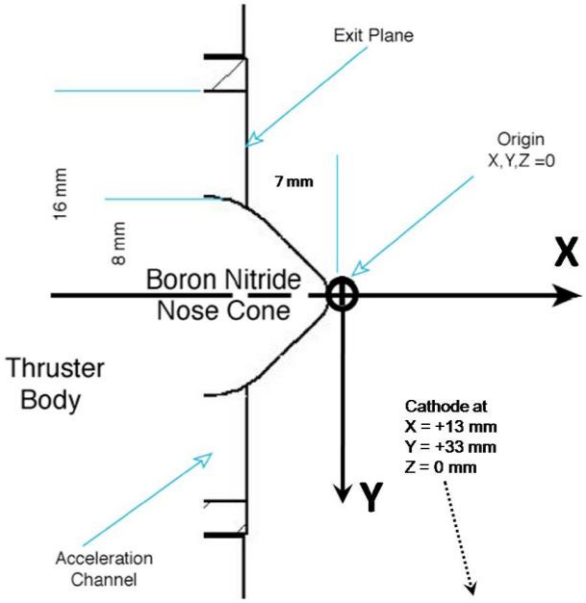

Figure 17. Coordinate System Used for 200W Thruster [32].

A Busek Power Processing Unit (PPU) controls the thruster and is powered by a Sorenson DCS 55-55E. The DCS 55-55E can supply up to 55V and 55A. The PPU requires 28V and ~17A to power the anode in the thruster, the magnets, and the cathode – including the heater. Normal operation without the cathode heater is 28V and ~8.7A for a power draw of ~244W. The interface for the PPU uses a Busek provided LabVIEW®

program with screenshot in Figure 18. Figure 19 shows a flowchart set-up of all the equipment and Figure 20 shows equipment used.

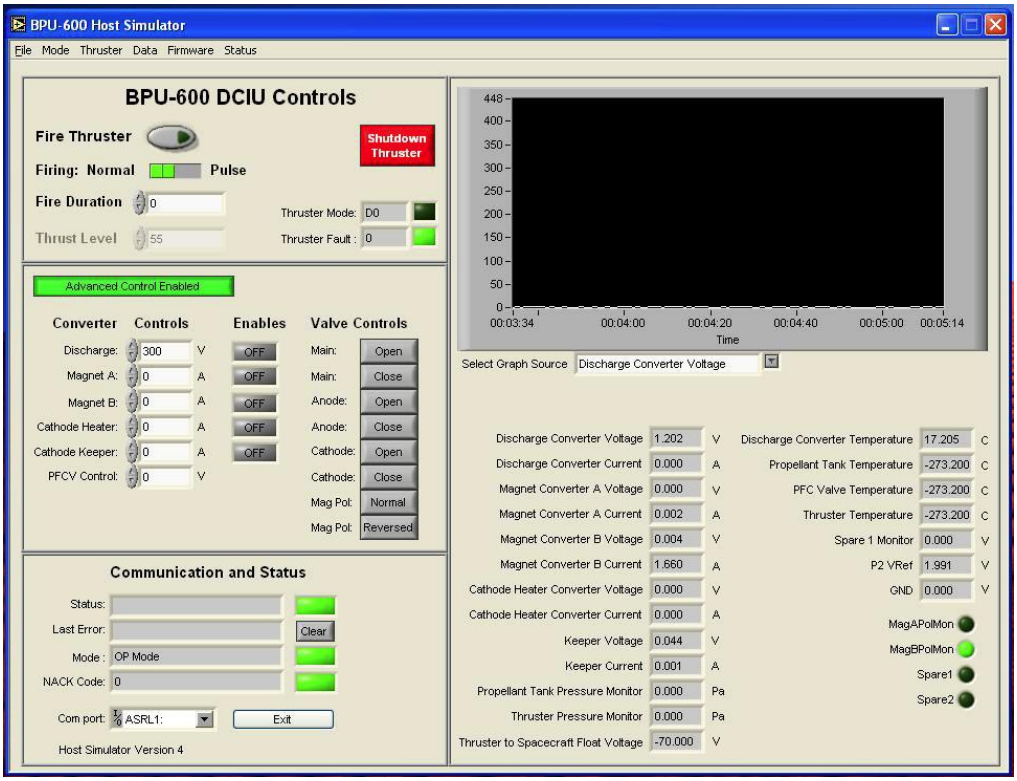

Figure 18. Screenshot of 200W Hall Thruster Controls in LabVIEW®.

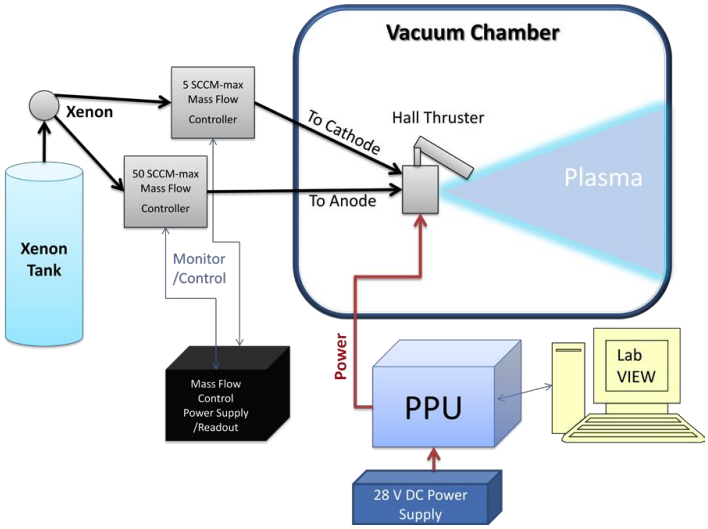

Figure 19. Flowchart of the 200W Thruster Set-up [41].

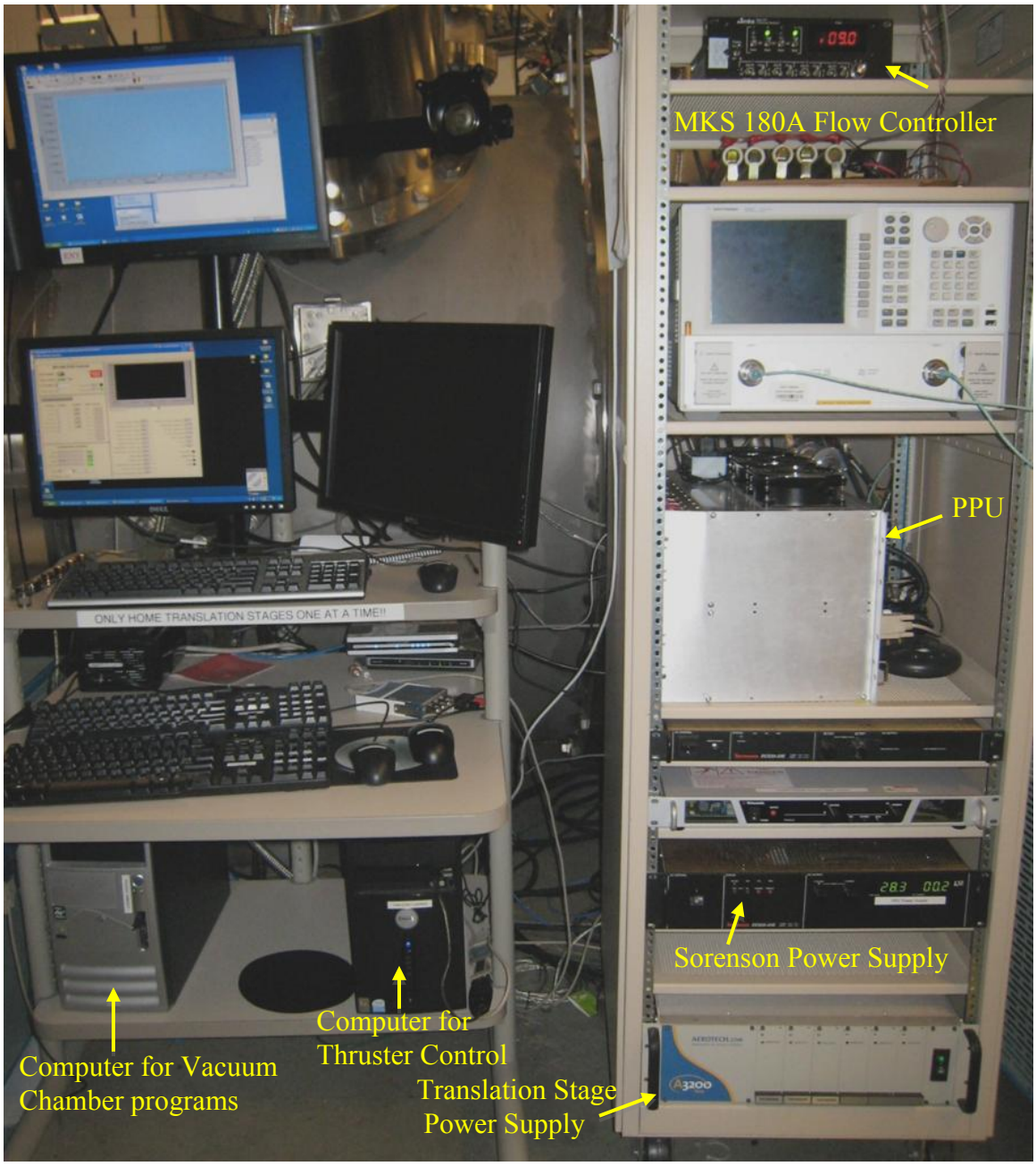

Figure 20. Hall Thruster and Translation Equipment.

Laser

The Sacher Lasertechnik TEC-420-830-1000 combines a Littman-Metcalf laser, TEC-500, and Tapered Amplifier Diode laser, TEC-400. The TEC-500 generates the desired frequency and has a tuning range of 786-843 nm through a coarse tuning screw

and fine-tuning using the piezo actuator. The piezo provides a 2GHz/V tuning rate with a mode-hop free range of 20 GHz. Changing the operating temperature of the diode laser also provides frequency adjustment. The optimized wavelength of 830.4 nm outputs ~30mW of power. The TEC-400 amplifies the incoming laser up to 1W at 834 nm. The TEC-400 can run in constant power or constant current mode. Both lasers employ Thermoelectric Cooling (TEC) to maintain diode laser temperatures.

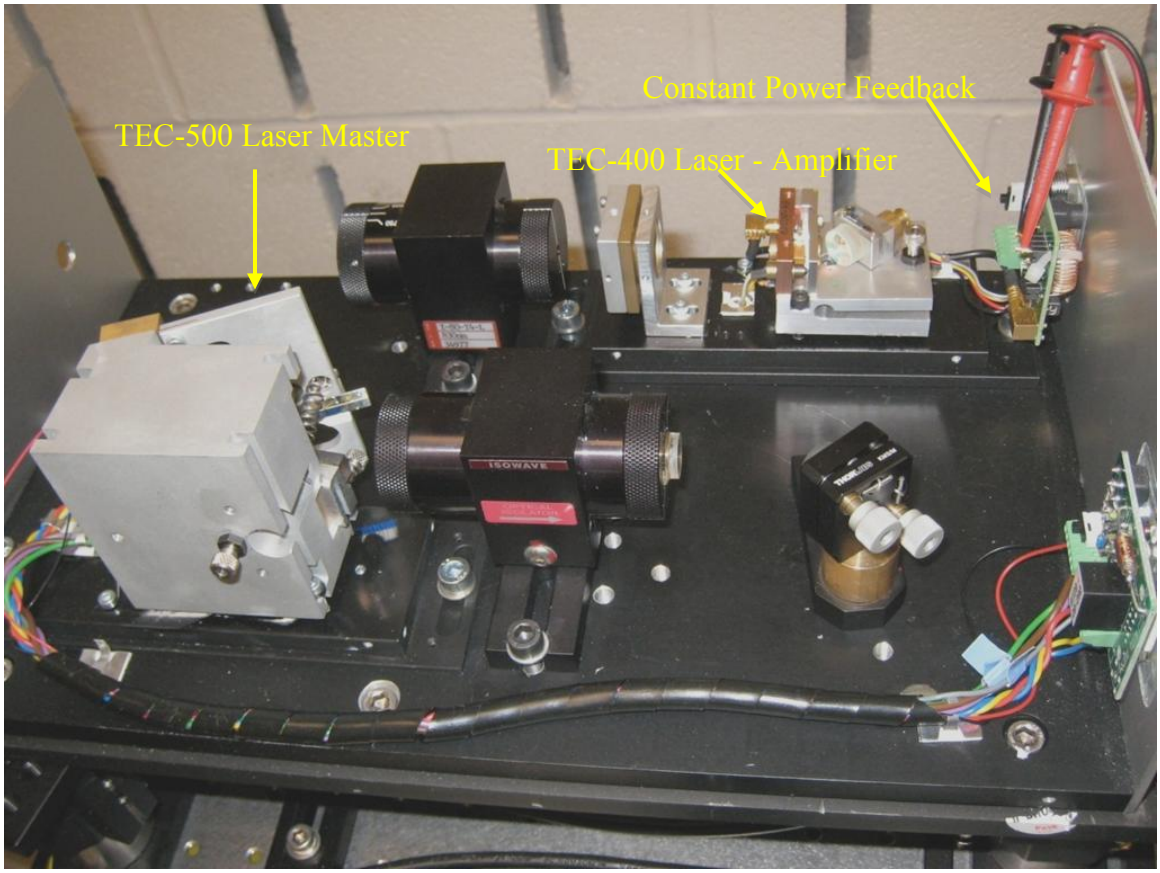

Figure 21. Sacher Laser

The New Focus Vortex 6000 Tunable Diode Laser was tuned to 834.68 nm, rated up to 50 mW and has a frequency range of 60 GHz, controlled through a piezo actuator. The New Focus laser initially provided for set-up and familiarization testing before the Sacher laser arrived.

Fabry Perot Interferometer (etalon)

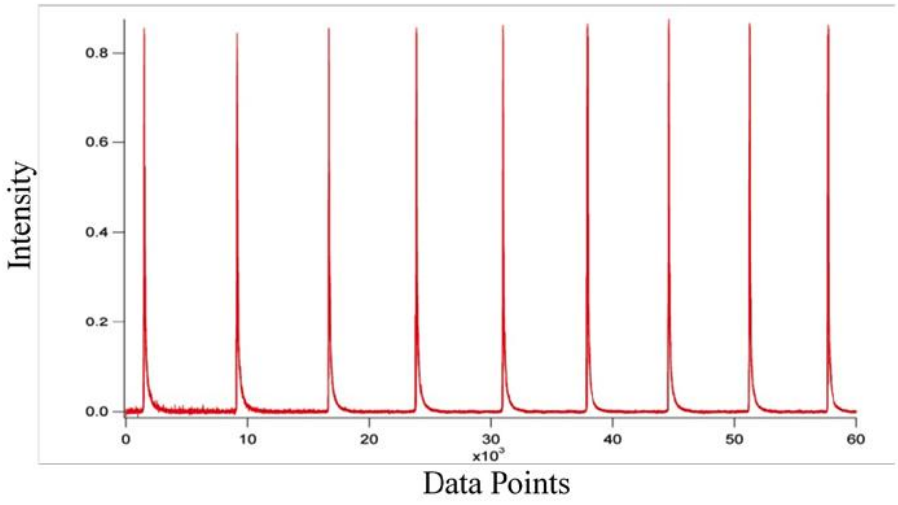

Figure 22. Etalon Trace [25].

The Thorlabs SA200-7A 1.5 GHz Scanning Fabry Perot Interferometer provides the reference to measure the frequency change between the absorption curve and LIF signal. By sweeping the laser frequency into an etalon, the output sends a series of peaks as seen in Figure 22 separated by the Free Spectral Range (FSR), in this case, 1.5 GHz.

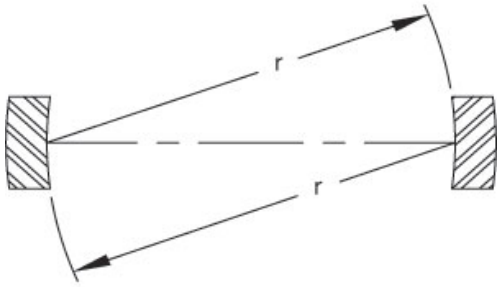

Figure 23. Diagram of Spherical Mirrors Used in a Confocal Etalon [44].

The Thorlabs etalon consists of a cavity formed by two nearly identical spherical lenses with radius, *r*, as defined in Figure 23. The lenses have a highly reflective coating on the inside and broadband anti-reflecting coating on the outside. Light entering a

confocal etalon, offset by a distance, *H,* from the center takes the following path as depicted in Figure 24. The light makes four reflections, at which point, it interferes with the incoming light. If in phase, the light experiences constructive interference and increases in amplitude allowing some light to pass through the back lens onto a silicon detector, producing the sharp etalon trace. Out of phase light experiences destructive interference resulting in minimum transmissions through the back mirror.

The FSR measures the spacing between the etalon traces. Equation (36) and (37) calculates the FSR for a plano-plano etalon and confocal etalon, respectively,

$$FSR = \frac{c}{2d} \tag{36}$$

$$FSR = \frac{c}{4d} \tag{37}$$

d denotes the separation distance of the mirrors [44]. The plano-plano etalon only reflects light twice but light in the confocal traverses the cavity four times, hence, the total round trip is 4*d* vice the 2*d* for confocal.

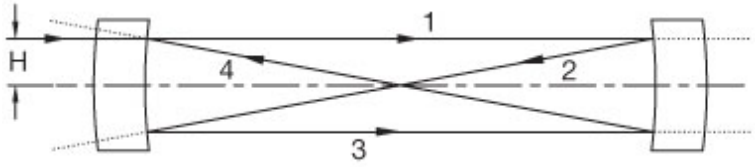

Figure 24. Diagram of Light Path Through a Confocal Etalon [44].

The finesse defines the resolution of the etalon, the ability of the interferometer to resolve closely spaced spectral features. For a narrow spectrum, the resolution is the width of the etalon peaks. Finesse depends upon the mirror reflectivity, mirror surface quality and the beam diameter and alignment. The etalon used has a resolution of 7.5MHz and a minimum finesse > 200.

The confocal design greatly simplifies alignment as the input beam offset distance, *H*, only needs to be a couple of millimeters from the center and input angle less than a few degrees. For a plano-plano etalon, the input angle must be near 0° for the light to fall back on itself.

Aligning the etalon is relatively simple. Connect the output of the etalon to an oscilloscope and vary the input beam position or angle and the etalon kinematic mount until the output signal maximizes. To produce constructive interference, sweep the laser frequency and every 1.5GHz increment produces a trace.

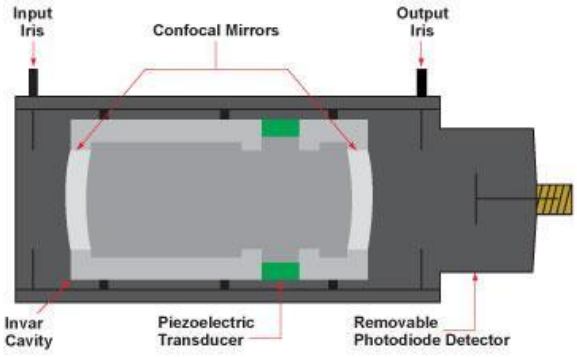

Figure 25. Cutaway Diagram of SA200-7A Fabry Perot Interferometer [45].

Lock-in Amplifier

The Stanford Research Systems (SRS) SR830 Lock-in amplifier detects and measures AC signals down to the nanovolt. The SR830 locks in on measurements even with noise signals thousands times larger than the desired signal. Use of the lock-in amplifier filters out background noise, i.e. the 60Hz frequency of the overhead lights or from the reference lamp. Knowing the proper settings and controls of the SR830 is essential for identifying and collecting the data.

Figure 26. Stanford Research System SR830 Lock-in Amplifier.

The lock-in amplifiers use a technique known as phase-sensitive detection (PSD) to filter out the signal at a known frequency and phase. The SR830 requires a reference signal to act as a baseline. It then takes a signal sine waveform, with amplitude V_{sig}, and multiplies it by a lock-in sine waveform, with amplitude V_L, generated by the amplifier using a phase-sensitive detector or multiplier. This procedure produces two AC signals sent through a low pass filter yielding the following DC signal

$$V_{psd} = \frac{1}{2} V_{sig} V_L \cos\ \theta_{sig} - \theta_{ref} \tag{38}$$

where V_{psd} is the amplitude of the DC signal and θ_{sig} and θ_{ref} is the phase difference of the signal and lock-in reference from the reference input signal. This result only occurs if the frequency of the lock-in waveform, ω_L, is equal to the frequency of the reference signal, ω_r. The PSD attenuates noises with different frequencies. Noise very close to the reference frequency passes through depending on the low pass bandwidth and roll-off settings but only signals matching the reference signal results in a true DC output.

The major settings to consider are the time constant and sensitivity. The time constant ranges from 10 μs to 30 s and determines the amount of time the instrument integrates the data. A short time constant results in erratic data. A long time constant

smoothes outs the data curve, but if set too long, critical transitions, i.e. absorption or LIF signals, are lost.

The SR830 provides a 0-10V output dependent on the sensitivity selected and an offset feature. Ranging from 2nV to 1V, the sensitivity should correspond to the expected voltage input from the signal; too high and any voltage change is indistinguishable; too low and the input signal overloads the SR830. Finally, the SR830 features an auto-gain to adjust the appropriate sensitivity level and auto-offset moves the output voltage to zero.

Photo Detector

The photo detector, Thorlabs DET10A High Speed Amplified Silicon Photo detector, measures the laser intensity. The DET10A has a detector area of 0.8 mm^2 and senses between 200-1100 nm with peak measurement at 740 nm. The rise time is 1.0 ns and is self-amplified with a 12V A23 battery. This detector also includes SM1 threads to attach an iris to reduce background lighting or a fiber coupling to place the fiber opening abutted to the silicon detector.

Figure 27. Thorlabs DET10A Photo Detector.

This photo detector serves two purposes; provide feedback to the laser controller while in constant power mode and measure the laser intensity to determine absorption. The feedback to each laser varies by design. The New Focus laser requires an input of 0-4V from the photo detector with 4V corresponding to maximum output. The Sacher laser directly measures the output current of the photo detector. Since the tapered amplifier provides the power boost, the detector wires directly to controller chip and operates off the "Slave" controller box. Setting the desired current, the controller adjusts the amplification of the laser to maintain the intensity into to the photo detector.

Monochromator and Photomultiplier Tube

A R928 Hamamatsu Photomultiplier tube (PMT) measures the intensity of the fluorescence after the Jobin Yvon Horiba H10 compact monochromator filters the signal.

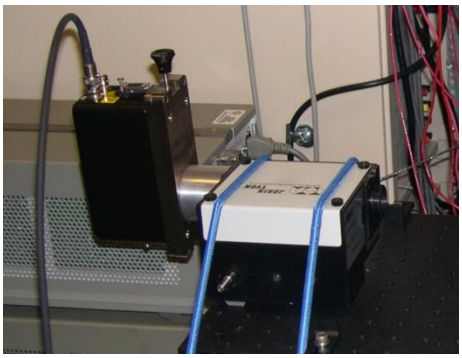

Figure 28. Monochromator and PMT Housing [25].

A monochromator isolates a range of wavelengths from continuous light sources. This device uses holographic diffraction grating of 1200 groove/mm with a linear dispersion of 8.0 nm/mm and has an aperture of *f*/3.5. A rotating mechanism provides a range of <100 nm to 893 nm. Slits at the entrance and exit narrow the band pass as shown in equation (39) [48]. In this experiment, the smallest available slit of 0.5 mm allows a band pass of ~4.0 nm.

$$\text{Band pass} = \text{Linear Dispersion} \times \text{SlitWidth} \tag{39}$$

A Products for Research Inc PRI1405 SHCE holds the PMT. The housing is made specifically for the R928 providing the required circuitry for operation and BNC connections to the PMT, specifically, a place for high voltage supply and a signal out for the PMT current to the lock-in amplifiers. In addition, the housing uses a Buna 2-044 O-ring to help seal the box and a manual sliding shutter over the opening. The housing and monochromator did not connect directly with each other so the AFIT Modeling shop created an aluminum cylindrical adaptor as seen in Figure 29 and attached to the monochromator.

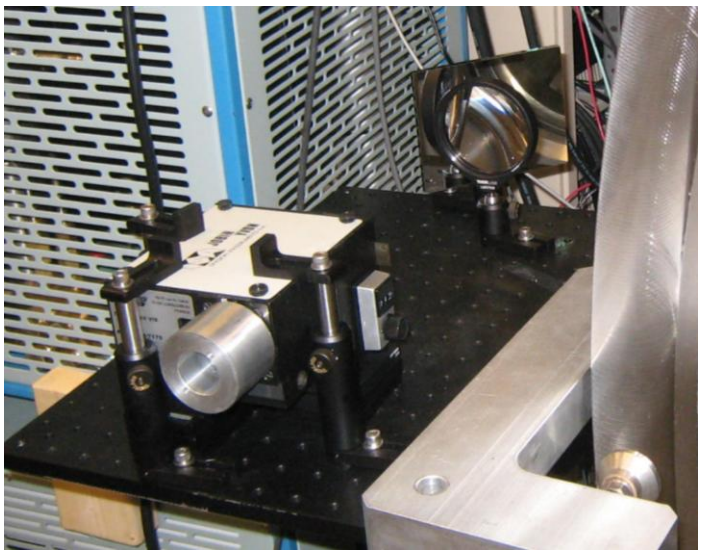

Figure 29. LIF Collection Outside Chamber.

Photomultiplier tubes (PMT) are vacuum tubes, able to detect individual photons of light. Using a wide variety of materials, the PMTs detect light in the ultraviolet, visible, and near-infrared ranges of the electromagnetic spectrum with high-gain, low-noise and high frequency response [49]. Individual photons excite the electrons in the photocathode, releasing photoelectrons into the vacuum. These electrons accelerate and

impact a dynode – a series of electrodes with a higher electrical potential than its predecessor – where secondary electron emissions multiply the amount of electrons. This cascading effect occurs with each successive dynode and generates an output current at the anode. The PMT multiplies the current produced by incident light by as much as 100 million times (i.e., 160 dB) enabling individual photons to be detected when the incident flux of light is very low. The PMT requires a high voltage power supply to create a potential difference between the dynodes.

Figure 30. Hamamatsu R928 Photomultiplier Tube.

High Voltage Power Supply

The SRS PS350 high voltage power supply provides the negative voltage to the PMT. It ranges from -5kV to +5kV with maximum current of 5mA. The PS350 uses a Kings type 1704-1 connector for the output and programmable and automatic trips to protect the PMT.

Figure 31. Stanford Research System PS350 High Voltage Power Supply.

Other Equipment Used

Wavemeter

The Bristol 621a wavemeter displays the lasers frequency or wavelength. In the ~830 nm range, the 621a has an accuracy of ±0.0002 nm or ±0.06 GHz and measures power up to 10 mW. It connects to the collecting collimator with a pre-aligned FC/PC connector (9 μm core diameter) and logs the data at a sample rate of ~4 Hz.

Figure 32. Bristol Wavemeter 621a.

Optical Chopper

The SRS SR540 Optical Chopper chops the laser beams and provides the reference frequency to the lock-in amplifiers to isolate the necessary signals. The SR540 operates from 4 Hz to 3.7 kHz and with two rows on the wheel, one chopper can handle two beams simultaneously. This experiment allocated one chopper for each beam while operating between 1.2-2.8 kHz.

Figure 33. Stanford Research System SR540 Optical Chopper.

Hollow Cathode Lamp

A Heraeus see-through hollow lamp filled with xenon coupled with a C610 power supply provides the baseline absorption curve of neutral xenon to measure the Doppler shift. The 120 mm path provides enough volume for absorption by neutral xenon to occur at both 823.16 nm and 834.68 nm.

Figure 34. Heraeus See Through Hollow Lamp.

Data Acquisition Device

The National Instruments (NI) Data Acquisition (DAQ) devices provide an input/output device from the PC to the equipment used. Specific downloadable equipment driver interfaces with LabVIEW®, a NI graphical programming environment using icons and wires to create a flowchart program to develop sophisticated measurement, test, and control systems.

An NI-9263 provides the ±10V signal from the LabVIEW® program to the laser to control the frequency sweeps. Two 4-channel NI-9215 BNC collects the ±10V signals collected via BNC cables at a maximum sample rate of 100,000 samples per second per

channel. The NI-DAQ9172 carriage houses all three modules and interfaces to the PC through USB cables.

Figure 35. NI-DAQ9172 Carriage (left) and NI-9263 (right).

Voltage Amplifier

The DAQ output voltage to the laser piezo provides a limited output of -10V to +10 V, below the -20 V to 120V piezo range for the Sacher laser. A voltage amplifier with gain set to 12× increases the voltage to provide a full sweep of the piezo. When using an amplifier, ensure the voltage does not exceed the piezo by limiting the DAQ to an output of -1V to +10V.

Testing used two voltage amplifiers, the MLD-1000 supplied by Sacher and a Quick Pack Power Amplifier EL1224 by Active Control Experts. The latter amplifier inverted the signal so; the NI-9263 output was range limited to -10V to +1V.

Low Noise Amplifier

A SRS SR570 Low-Noise Current Preamplifier amplifies the signal coming from the Fabry Perot Interferometer. The signal strength from the etalon depends on the laser intensity and the SR570 increases the signal as necessary, staying within the NI-9215 BNC input limits.

Figure 36. Stanford Research System SR570 Low-Noise Current Preamplifier.

Diagnostic Tools

Pico Ammeter

A Keithley 2400 Sourcemeter/Picoammeter measures the low current signals generated by the PMT. The PMT current depends on the voltage applied to the PMT, the intensity of the fluorescence and the background noise allowed through the monochromator. The picoammeter measures the PMT output current used to determine the appropriate resistance level and corresponding voltage drop measured by the lock-in amplifiers. In addition, the picoammeter helps diagnose for a degraded PMT. The current jumps if the PMT is exposed to any photons. It is prudent to ensure the PMT is not oversaturated when performing this test.

Figure 37. Keithley 2400 Sourcemeter/Picoammeter.

Power Meter

The Ophir Spiricon Vega power meter and 3A-FS power head is an essential tool for aligning the laser. The sensor has a range of 30μW to 30W with an accuracy of ±3% for wavelengths between 190 nm to 20,000 nm. Aligning the laser requires adjusting the appropriate knobs of the laser to maximize the output on the power meter display.

Software

LabVIEW® Code

The National Instruments LabVIEW® code controls the laser frequency sweep and collect the data. Figure 38 shows the front panel. Appendix A displays the back panel and describes the block/wire diagram.

On the front panel, the user specifies the starting and ending ramp voltage ensuring the product with the voltage amplifier gain stays less than the piezo voltage limits. The user also defines the number of data points, scan rate, file name and path. The "# of iteration" and "Time Delay" boxes give the user an option to loop data collection and write to separate sequentially numbered output files while coordinating the timing with the translation stage program to provide for automated data collection.

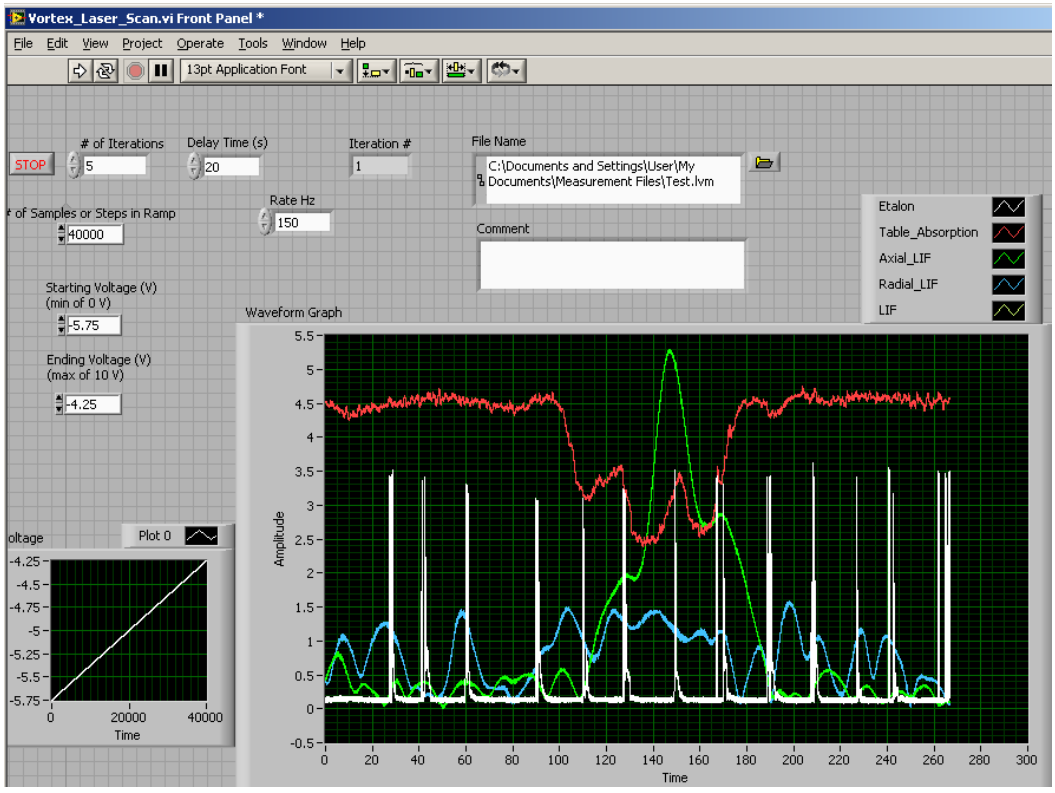

Figure 38. Screenshot of LabVIEW® Code to Sweep and Collect Data.

Aerotech A3200

The Aerotech® program, A3200, operates the translation stages within the chamber with a detailed description in the Appendix B. A3200 can manually move the stages or operate from a script to automate movement. The program also allows the user to define a local coordinate system. In this research, the origin is defined at the tip of the thruster nose cone. At start-up, the A3200 zeros the coordinates regardless of position and the user must "Home" each stage.

Wavemetrics Igor®

The Wavemetrics Igor® Pro specializes in processing large sets of data. Igor® displays the data, smoothes the data, fits the data with curves and plots the data. In addition, a procedure provides a graphical interface to analyze and calculate the velocity determined from the Doppler equation.

This procedure starts by loading the data into waves corresponding to each column in the file. Next, the user must resolve the etalon trace with the assistant of graphs presenting the etalon data in different perspectives. The procedure then displays a plot of the LIF and absorption signals but rescales the signals as the independent axis is converted from data points to GHz based on the processed etalon trace. Igor® can auto fit the LIF and absorption signals with Gaussian curves or the user can manually bracket the signals and fit the curves. Finally, Igor® calculates the velocity by determining the frequency separation of the peaks, subtracting 18.1 GHz and applying equation (22). The 18.1 GHz accounts for the difference between the neutral absorption curve at 834.68 nm and the ionic line at 834.724 nm. The Appendix C contains a more detailed description the procedure.

Optics

Lens

Selection of the optics must take into account the amount of light collected vs. the survivability of the optics. Optics placed close to the target collects more photons per area, a higher irradiance. On the other hand, placing the lens too close to the plume results in highly energized xenon ions traveling at extreme velocities impacting the lens, degrading them. Selection of lens distance and type begins by considering the *focal ratio* or *f/#* of the monochromator. The *f/#* is the flux density at the image plane and is derived in equation (40)

$$f/\# = \frac{f}{D} \tag{40}$$

where D is the diameter of the lens and f the focal length of the lens [60]. A smaller *f/#* means more light reaches the image plane. Since the monochromator chosen has an *f/#* equal to *f/3.5*, ideally, the focal length and diameter of the lens should result in an *f/#* less than 3.5.

To minimize *f/#*, select the largest, practical, diameter lens commercially available made with materials maximizing transmission rate for the wavelength used. In this case, a 75 mm, uncoated N-BK7 lens with a 250 mm focal length from Edmund Optics provides a f/ # equal to *f/3.33*.

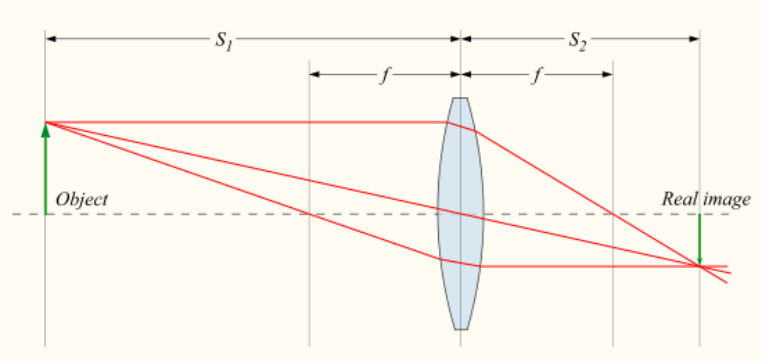

Figure 39. Depiction of Gaussian Lens Equation [61].

The Gaussian Lens Formula determines the placement of the lens as illustrated in Figure 39 and shown in equation (41)

$$\frac{1}{S_1}+\frac{1}{S_2}=\frac{1}{f} \tag{41}$$

where S_1 and S_2 are the distances of the object and image from the lens, respectively [60]. Set S_1, the distance of the lens from the thruster, equal to f, then S_2 must equal infinity resulting in collimated light. Another lens refocuses the collimated light into the monochromator by setting the distance between the lens and monochromator equal to the focal length of the second lens. For this set-up, a mirror reflects the collimated fluorescence signal and then another 75 mm uncoated lens with a 75 mm focal length focuses the signal into the monochromator, Figure 29.

Fiber Optics and Lens Tubes

Earlier set-ups of this LIF system passed the laser through 10 mm thick borosilicate glass located on the chamber door, creating an etalon feature in the signal. Using equation (36) and the properties of the glass, Morgan determined the FSR was 6.24 GHz and could not correct the data taken [25]. This necessitated a change in the LIF set-

up to either a) illuminate the beam through the window at the Brewster angle, the angle minimizing reflection, or b) use fiber optics.

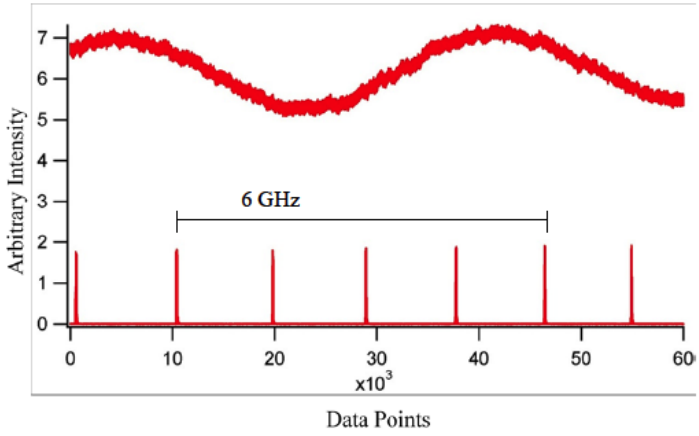

Figure 40. Etalon Issue Through Vacuum Chamber Window [25].

Fiber optics channels light within a long narrow dielectric using internal reflection to prevent photon leakage. When selecting fiber, one must consider the core diameter, the numerical aperture, and if the fiber is single- or multi-mode. A larger diameter fiber allows more light to focus into the fiber but has a larger bend radius.

Equation (42) calculates the numerical aperture, *NA*, the light gathering power of the system

$$NA = n_i \sin\theta_{\max} = n_f^2 - n_c^2 \tag{42}$$

where n_i is the incident medium of index, i.e. air, n_f and n_c the index of refraction for the fiber core and cladding wrapped around the fiber, and θ_{max} the acceptance angle [60]. Light striking the fiber face with angle greater than θ_{max} partially reflects and eventually leaks out of the fiber into the cladding.

Light enters the fiber at different angles resulting in thousands of different ray paths, or modes, by which the light can propagate to the end. These fibers are known as multimode fibers. Single mode fibers are made thinner, typically less than 10 μm, allowing only one ray path along the core. These fibers are more expensive, have a greater attenuation (0.2 dB/km vice 0.1 dB/km) and operate at higher wavelengths, ~1.5 μm.

This set-up selected four low OH 600 μm muti-mode fused silica fibers with a *NA* equal to 0.22 from Multimode Fiber Optics, Inc. The fibers used SMA connectors and were sheathed in flexible stainless steel square-lock to protect the fiber from the plasma in the vacuum chamber. The fibers entered the chamber in four feed-through running though a QF-40 flange. Two of the fibers were designated to bring in the laser from the optics table, one fiber to collect the laser after it passes through the thruster plume to measure radial absorption and the final fiber attached to optics within the chamber to collect the fluorescence signal.

Two 10 mm LC-10N collimators from Multimode Fiber Inc focused the laser into the fiber. To mount the collimators, the AFIT modeling shop created aluminum adapters with screw mounts allowing the collimators to fit within the Thor Labs KS1 mounts as shown in Figure 41.

Figure 41. Collimator with Adapter in a Kinematic Mount.

The laser exiting the fiber diverges according to the θ_{max} dependent on the NA of the fiber. The laser requires refocusing to an acceptable waist size of ~1-2 mm by using combinations of a 1-inch lens in a lens tube. The tube protects the lenses from the plasma with the exception of the outermost lens.

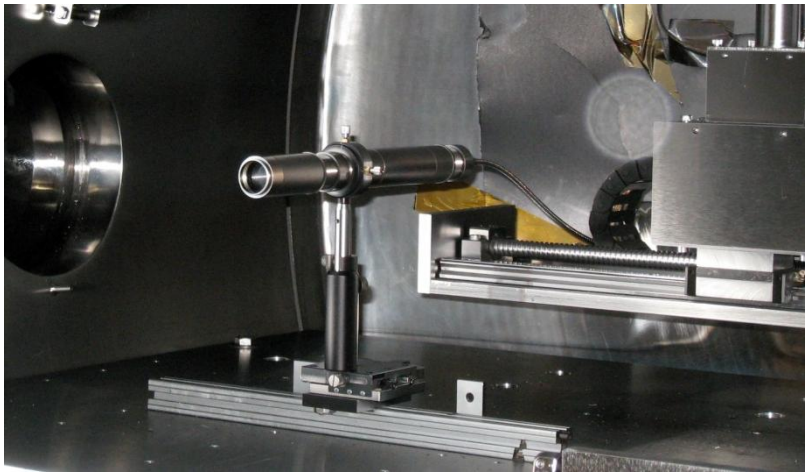

Figure 42. Axial Probe Beam Lens Tube Set-up.

To focus the axial laser, a 100 mm focal length, f_1, plano-convex lens placed ~100 mm from the fiber collimates the light. This light passes through a 50 mm focal length, f_2, plano-concave lens and a 100 mm focal length plano-convex lens. Adjusting the

distance separating the concave and convex lens, *d*, creates the desired back focal length (b.f.l.) of the overall lenses using equation (43) [60].

$$b.f.l. = \frac{f_2(d - f_2)}{d - (f_1 + f_2)} \tag{43}$$

This set-up results in a ~1.5 mm axial beam waist.

For the radial laser, equation (41) used a 100 mm plano-convex lens to create a ~2 mm waist.

After passing through the plume, the absorption signal collects the radial laser using a collimator to focus the laser into the fiber. The other end of the fiber outside the chamber attaches to an SMA adapter connected to the Thor Labs DET10A photo detector, abutting the fiber end to the silicon detector. The detector connects to an SR830 lock-in amplifier referencing the radial laser SR540 chopper through a BNC T-junction connector.

Collecting LIF Using Fiber Optics

Vacuum chamber real estate was shared between this project and an 80/20® structure installed for microwave interferometry as a Hall thruster diagnostic tool. The microwave structure required a specific thruster placement restricting the use of the vacuum chamber windows as a path to collect the LIF signal. To accommodate both projects, a strategy was devised to use fiber optics to collect the LIF signal accomplished previously in other LIF experiments on Hall thrusters [63].

Figure 43 shows the set-up for both projects. The radial probe beam and absorption collimator was attached to the microwave structure with the axial probe beam mounted on the shelf at the back end of the chamber.

The LIF fiber optics were mounted to a ¾" 80/20® bar to create a rigid and portable unit. The set-up was aligned outside of the chamber reducing alignment time within the chamber. The optics were also mounted on Thorlabs kinematic bases to allow for fine tuning. The 50.8 mm collection lens had a 1000 mm focal length and fed into a 50.8 mm lens with a 125 mm focal length. This lens focused the light into the collimator attached to the fiber using an SMA connector.

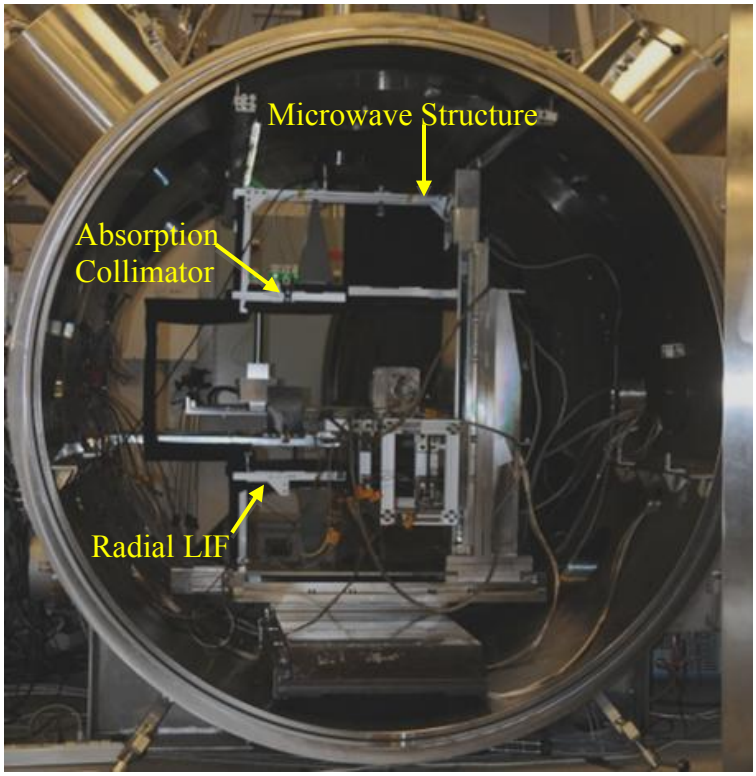

Figure 43. Set-up of Microwave Interferometry Structure.

The selection of optics, a 50.8 mm lens with 1000 mm focal length, resulted in an *f*/20. Couple this with focusing losses into the fiber; the LIF signal was too weak for the PMT to amplify. The LIF-fiber optics set-up managed to collect neutral xenon LIF

signals on the table with the see-through hollow cathode lamp but only at the very strong spectra line at 823.16 nm.

This set-up may succeed if it can collect more photons and focus the photons into the fiber by switching to a 75 mm or larger lens diameter and a fiber core 1-μm or larger.

After completion of the microwave interferometry, the vacuum chamber thruster was set-up to the configuration described in chapter three. The LIF collection optics was placed in an ideal location, within 250 mm of the thruster and focusing directly out of the vacuum chamber window. This minimized the amount of optics within the chamber and provided an *f/#* smaller than the monochromator, ensuring more LIF photons were collected then can pass through the monochromator.

Vacuum Chamber Optics Set-up

The radial lens tube attaches to a post providing coarse movement along the Y-axis and rotation about it. The post mounts to the side of the vacuum chamber using an 80/20® structure shown in Figure 44. The radial laser has the coarsest control and least freedom of movement requiring first set-up.

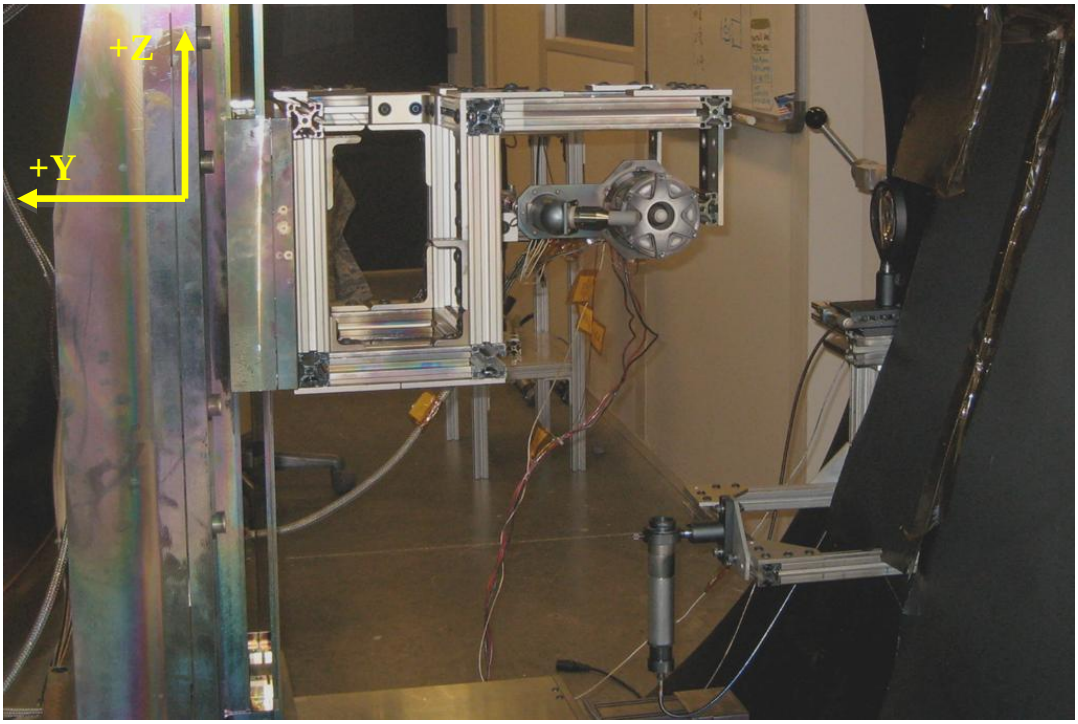

Figure 44. Set-up of Thruster, Radial Beam and LIF Collection Optics.

The axial laser perches on top of a post allowing coarse adjustment in the Z-axis and rotation about it. The post height is set at an approximate height to minimize the radial probe-beam waist size. Moving the Z-axis on the translation stage fine-tunes the center point location. The post sits on a kinematic base allowing fine-tuning along the Y-axis until the axial laser intersects the radial beam. For the X-axis, the base attaches to the shelf in the back of the chamber using 80/20® at a distance equal to the b.f.l. from the thruster, minimizing the axial waist size.

A 75 mm diameter uncoated plano-convex lens with a 250 mm focal length collects the LIF signal from a distance of ~250 mm orthogonal to the intersection of the axial and radial beams. The lens resides on a kinematic base allowing for fine-tuning in the X-axis and the base attaches the vacuum chamber in front of a window using 80/20®. The light passes through the window and a mirror, attached by epoxy onto the kinematic

mount, redirects the LIF signal into the monochromator after being focused by a 75 mm lens with a 250 mm focal length. The monochromator can easily adjust to collect the fluorescence photons at 541, 823, and 834 nm.

The PMT housing screws onto the back of the monochromator and a PS350 high voltage supply provides a negative voltage to the PMT. A laser optics breadboard on top of tripod provides the base for the lens, mirror and monochromator. The PMT output connects to a grounded resistor. The resistor provides a voltage drop for the two SR830 lock-in amplifiers to measure while frequency locked-in to the SR540 optical choppers separating the axial and radial signals. The resistor selection depends on the current output of the PMT and varies from 20kΩ to 100kΩ.

Of note, only three lock-in amplifiers were available and four are required to measure both LIF and absorption in the plume on the same run as one amplifier is dedicated to the table absorption.

Table Set-up

The laser beam first passes through a beam sampler splitting off between 1-10% into the DET10A photo detector. This detector measures and amplifies the current to provide feedback to the TEC-400 when the laser operates in constant power mode.

The beam then passes through a Faraday isolator to prevent feedback to the laser, gets redirected by a mirror and through two irises on the other side. The irises facilitate the installation and alignment of a new laser head.

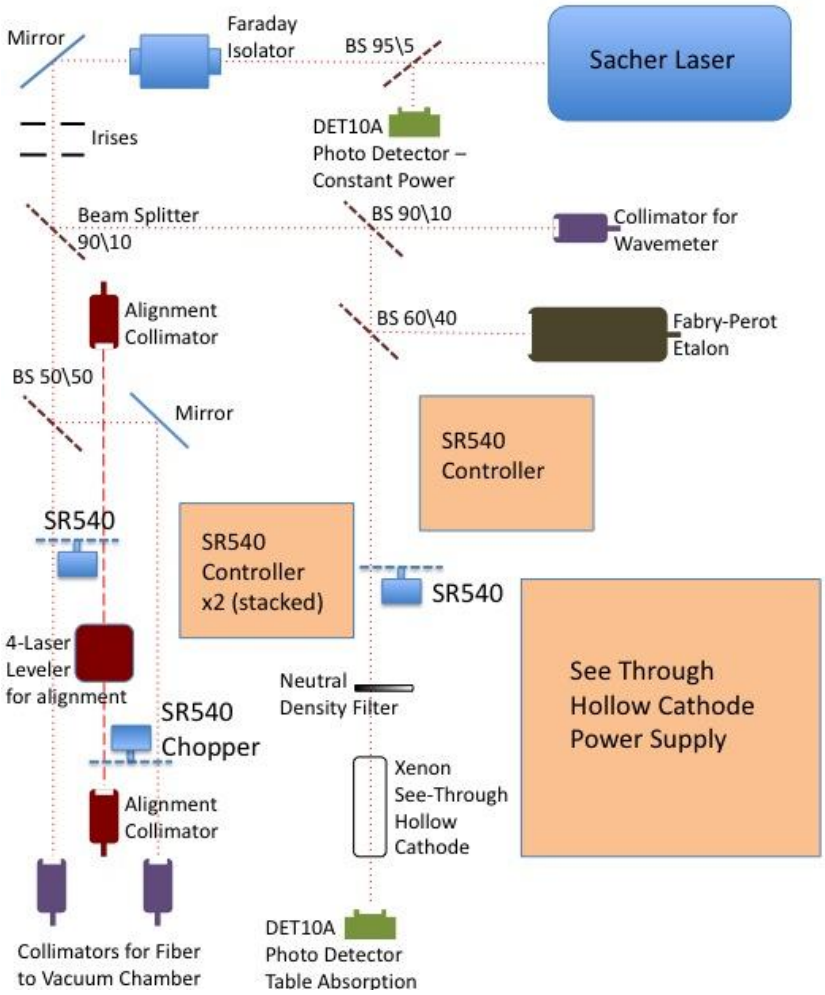

Figure 45. Diagram of Laser Table Set-up.

The laser beam splits off using a 90/10 beam splitter with 90% of the laser power, the probe beams, directed towards the vacuum chamber. A 50/50 splitter divides the probe beam before the beams pass through SR540 optical choppers using a 40 blade wheel and spinning at ~2kHz and ~2.4kHz. Collimators focus the beams into the fiber leading to the vacuum chamber.

The remaining 10% provides the laser input for the reference devices. A 90-10 splitter passes the majority of the beam to the Bristol 621a wavemeter. A 60/40 splitter

sends 40% to the Scanning Fabry-Perot Interferometers and the rest to a SR540 operating at 1.4 kHz before passing through the hollow cathode lamp. A variable neutral density filter wheel reduces the intensity before this beam enters the lamp to prevent oversaturation of the absorption signal by the laser. Finally, a DET10A detector measures the beam power.

Alignment is key for this test set-up and two laser levelers facilitate the process. On the table, a multi-laser leveler and two additional collimators are placed strategically to pass the red laser through the choppers on the table. The additional collimators are dedicated to the alignment laser allowing a quick-change from a NIR to a red laser. Alignment inside the chamber uses the visible red laser by switching the probe beam fiber to the different sets of collimators.

The collection optics also requires alignment. A second laser leveler on top of a tripod is placed behind the monochromator with the PMT housing removed. The monochromator opening slit is cut into a reflective metal. The laser is aligned so the reflection off the metal reflects back onto the laser. The monochromator wavelength knob is rotated until the laser passes though allowing the laser to follow in reverse the path the LIF photons would take forming a red point at the desired collection volume.

All three red dots are then aligned onto a common point using a business card or the nose cone of the 200W thruster. Alignment works best by starting with the laser with the least freedom of motion and coarsest tuning range and working backwards. In this case, the radial LIF stays stationary while adjustments occur on the axial laser and finally the LIF collection mirror taking advantage of the dual-axis kinematic mount. The translation stage then positions the thruster to complete the local coordinate axis.

Laser Induced Fluorescence

Laser Alignment, Multi-moding & Frequency Hops

The Littman-Metcalf design uses a diode laser, tuning mirror and diffraction grating to produce a narrow, tunable single mode laser. The individual components are detailed and then put together to provide background information before discussing the importance of alignment, multi-moding and frequency hop effects.

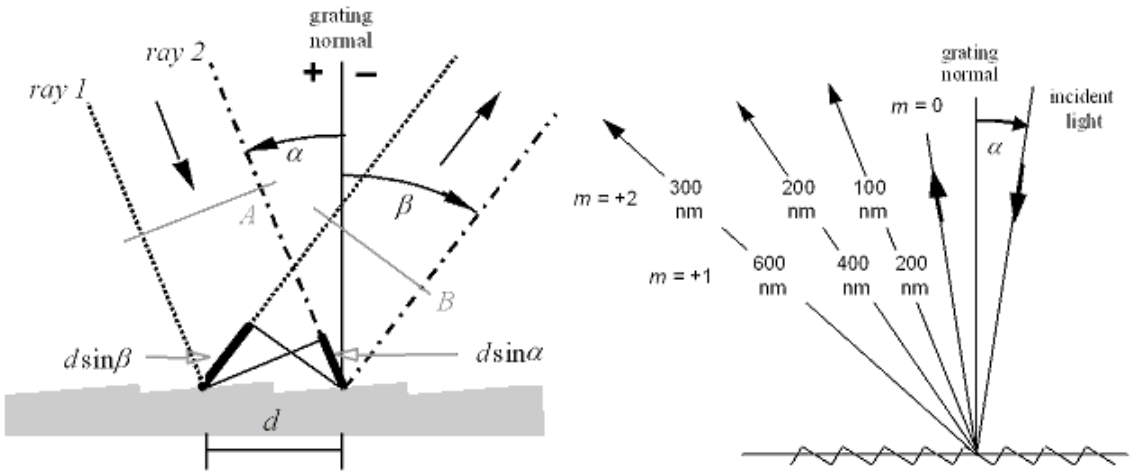

Figure 46. Examples of Diffraction Grating and Spectral Orders [63].

Diffraction Grating

A diffraction grating is a collection of reflecting elements splitting and diffracting light into several beams travelling in different directions. The grating has a sawtooth pattern, as shown in Figure 46 and each grating groove approximates a very small, slit-shaped source of diffracted light, essentially, turning the wave front of the light into individual point sources. The beams combine together. Those in phase result in constructive interference satisfying the diffraction equation

$$d\left(\sin\alpha+\sin\beta\right)=\lambda m \tag{44}$$

where d is the grating spacing, α and β angles shown in Figure 47, λ the wavelength of the laser and m an integer number representing the diffraction order [65]. The zeroth-order corresponds to specular reflection, denoted $m = 0$. Other maxima form with non-zero integers values for m resulting in reflections at different angles. The $m = 1$ maximum is known at the first order [63].

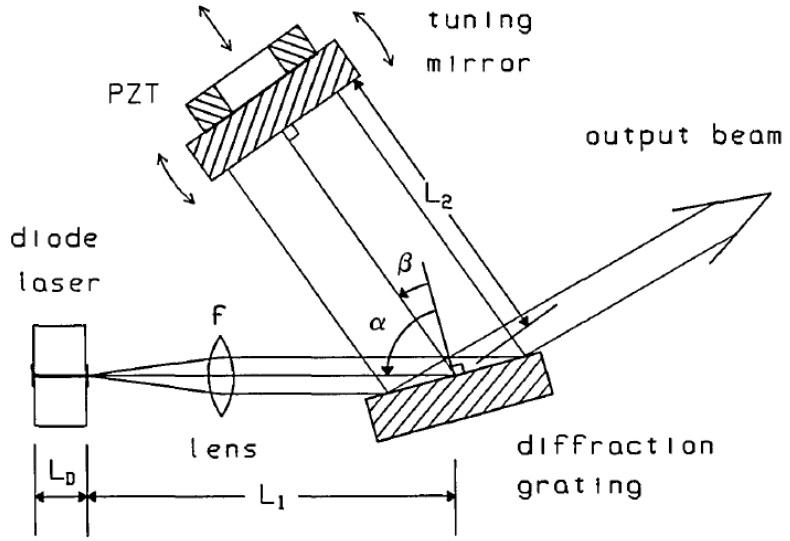

Figure 47. Littman-Metcalf External Cavity Diode Laser (ECDL) [64].

Diode Laser

Diode lasers consists of a basic P-N junction using the crystalline semi-conductor mirror as the facet planes for the end mirror. Placing an anti-reflective coating on the front and highly reflective on the back ensures lasing in one-way.

The diode laser produces photons under the same principles of Light Emitting Diodes (LEDs), from the recombination of the holes being injected in the p-region and electrons coming from the n-region. Unlike the LED, a diode laser has an optical cavity formed using the facets and waveguides built into the crystal surface to confine the photons into a relatively narrow collimated beam with a Gaussian shape [66]. The

waveguide width is a trade-off between power and beam quality. A wider waveguide allows for more power as there is a greater volume of the gain medium but if too wide, the waveguide can support multiple lateral optical modes, and the diode laser can "multi-mode".

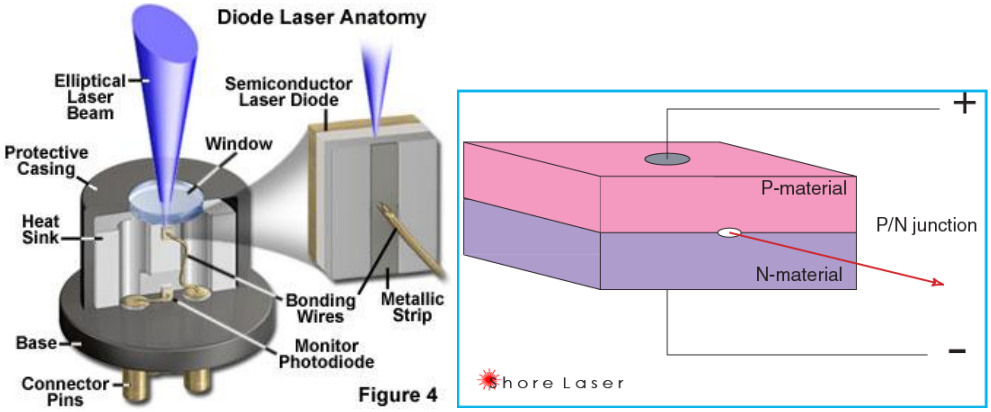

Figure 48. Diagrams of Diode Laser [67-68].

A diode laser wavelength range depends on the bandgap of the materials used. The length between the crystal's facets, L, determines the specific wavelength lines the diode laser can output according to equation (45) [69].

$$L = \frac{N\lambda_N}{2} \tag{45}$$

Those wavelengths, whose half-wavelengths divide evenly into the cavity length (are multiple integers, N, of the length), adds constructively after reflecting off the crystal facets, similar to a Fabry–Pérot interferometer. The result is shown Figure 49, the diode laser features multiple peaks with narrow width under the gain curve of the diode. The intensity of the peaks decreases away from the center wavelength of the diode.

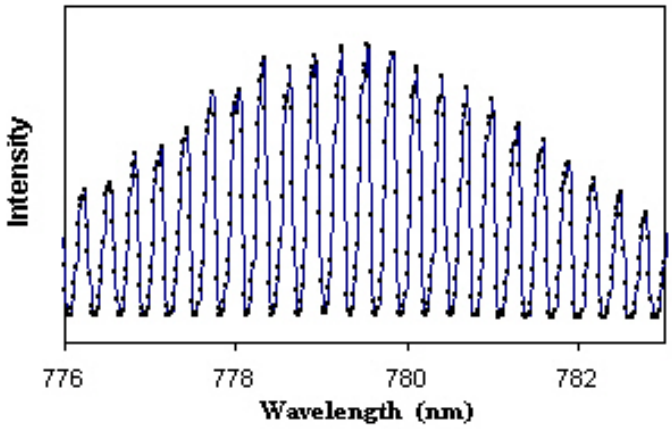

Figure 49. Modes of a Diode Laser and Intensity Versus Wavelength [69].

External-Cavity Diode Lasers (ECDLs)

The ECDL starts with a diode laser with a highly-reflective end mirror on the rear facet of the laser and a high quality anti-reflection coating on the front facet. The diode is the lasing medium and the output light passes through a collimating lens onto a diffraction grating at a grazing incidence ($sin\ \alpha \approx 1$). The zeroth-order reflection is the laser output while the first-order reflection reflects back into the laser by the external mirror to provide feedback. The laser has multiple modes, or wavelengths depending on the cavity length similar to equation (45).

Solving both equations (44) and (45) simultaneously determines the lasing wavelength by adjusting the cavity length, the grating angle and mirror-grating angle. The grating disperses the different laser diode modes except one, resulting in a single wavelength with a very narrow line-width, known as single-mode. Varying the angle between the mirror and grating tunes the coarse wavelength through a screw or piezoelectric actuator for fine-tuning. The mirror rotation point is selected to maintain

the appropriate cavity length while rotating the mirror. This prevents discontinuous tuning or "mode hops".

Alignment and Multimoding

Unlike the New Focus laser, the Sacher TEC 500 has a removable cover allowing access to make adjustments as seen in Figure 21 and Figure 50. One set of knobs controls a mirror aligning the output of the TEC-500 master laser into the input of the amplifying TEC-400. Another screw provides coarse adjustment of the wavelength. Two additional screws adjust the collimation from the diode and angle of the diffraction grating as part of the external-cavity diode laser design.

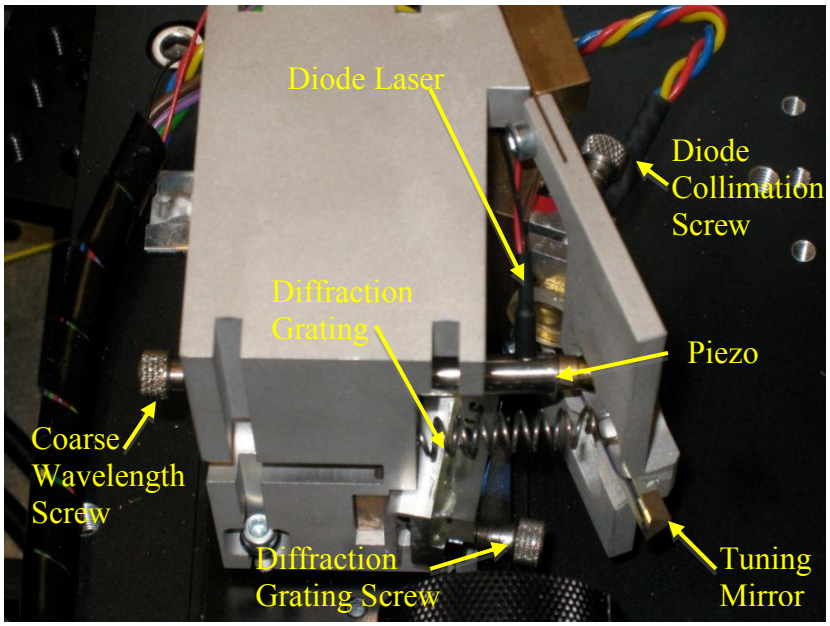

Figure 50. Close-up of the Sacher Laser TEC-500.

The easiest method to check the alignment involves maximizing the output intensity of the laser using the power meter as a reference. A misalignment causes a systematic multi-moding and mode hops seen in the wavemeter output and etalon trace.

The multi-moding results in unevenly spaced etalon traces in Figure 51. The uneven etalon trace is caused by multiple wavelengths hindering the normal constructive interference spikes. Mode hops in Figure 52 show jumps in the green wavemeter output. An aligned plot is shown in Figure 53.

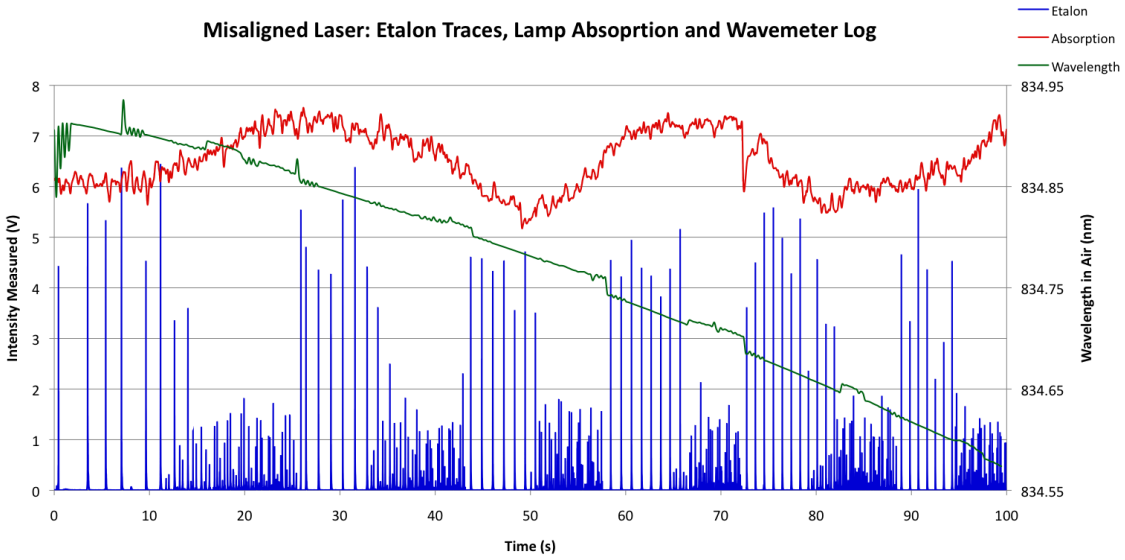

Figure 51. A Misaligned Laser and Corresponding Wavemeter and Etalon Plots.

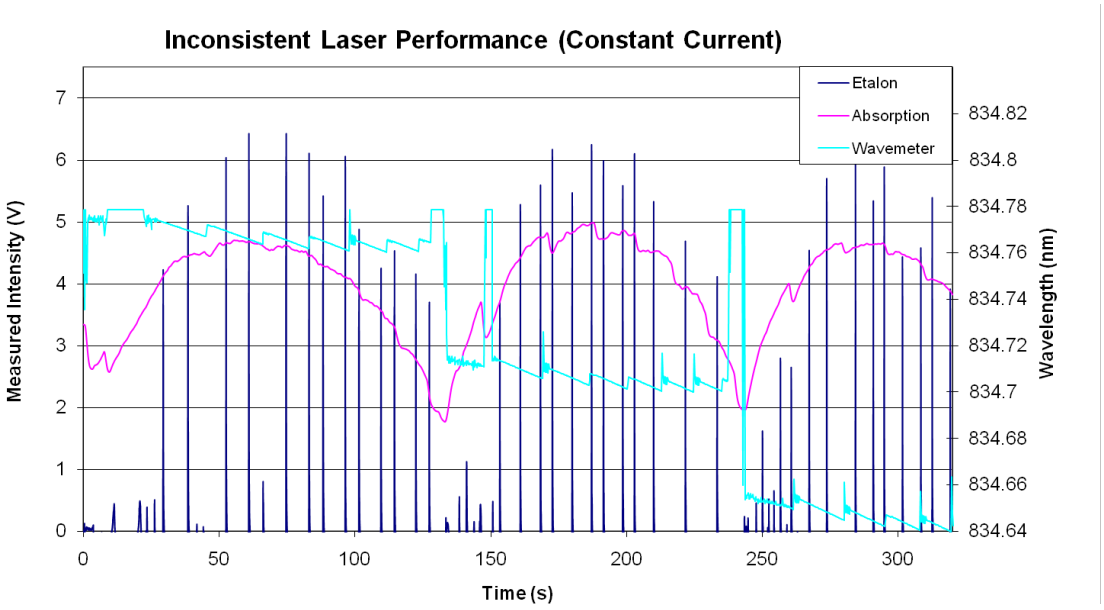

Figure 52. A Misaligned Laser Operating in Constant Current Mode.

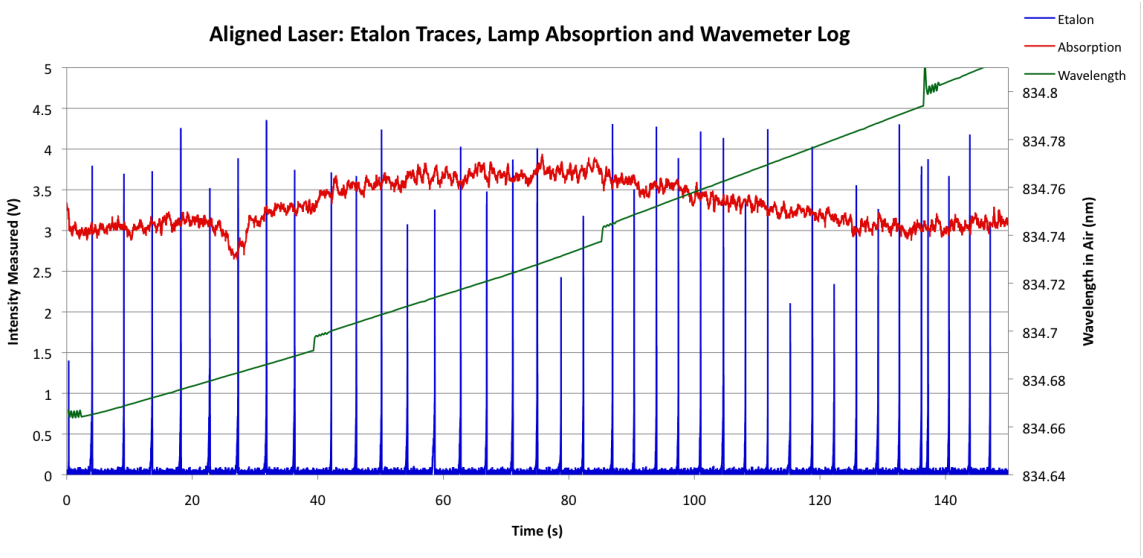

Figure 53. An Aligned Laser and Corresponding Wavemeter and Etalon Plots.

While multi-moding, an absorption signal is difficult to distinguish. Looking at the aligned plot, absorption occurs at 25 seconds in Figure 53. Compared with the unaligned plot in Figure 51, at 72 seconds, the laser stops multi-moding at the same wavelength when absorption occurs. The result is a sharp drop in the absorption curve voltage contrasting the symmetrical, shaped curve in the aligned plot.

Frequency Hops

In all three plots, a jump in the wavelength curve signals a frequency or mode hopping. The Sacher laser has a tuning range of over 20 nm using the coarse tuning screw sweeping through all the discrete wavelengths produced by a similar diode as shown in Figure 49. The piezo actuator fills the gaps providing a continuous spectrum of wavelengths but the piezo cannot cover the entire range. About every 20 GHz, the laser

starts to mode hop as it jumps from one laser mode to another in the diode. The aligned graph, Figure 53, illustrates the mode hop as either a jump in the wavemeter plot, or two peaks spaced farther apart or spaced much closer together in the etalon plot at 40 and 135 seconds respectively.

Effect of Temperature

Temperature greatly affects the performance of a diode laser, especially the output frequency. The frequency fluctuates if the temperature controller cannot maintain a constant temperature. Figure 54 shows a plot of a frequency sweep with the diode laser temperature oscillating ±0.02°C. The wavemeter confirms the slope of the frequency scan but the slight fluctuations caused by the diode temperature results in multiple etalon traces as the frequency traverses back and forth over the constructive interference wavelength.

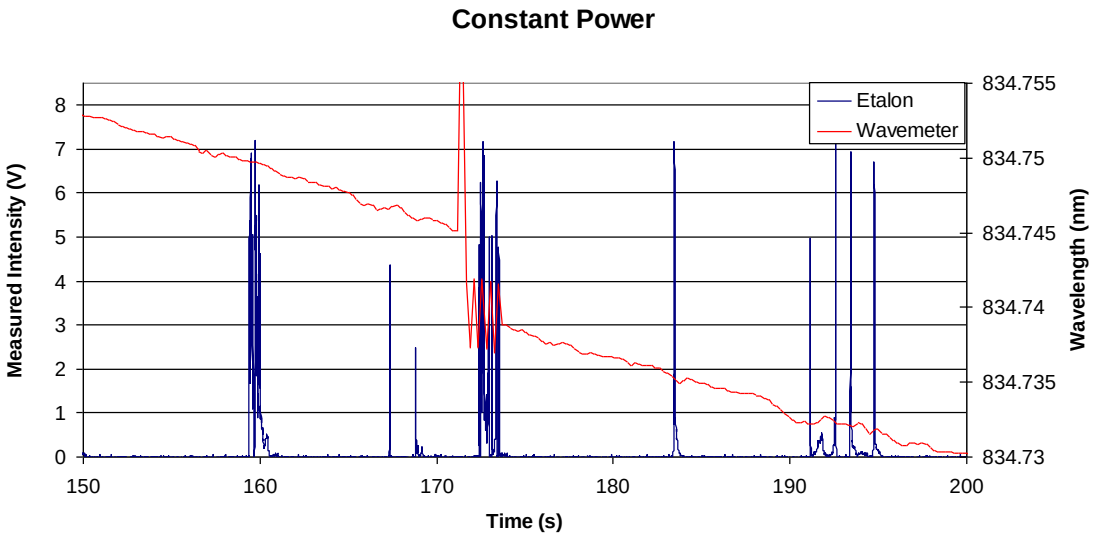

Figure 54. Diode Laser Temperature Oscillation Effect on Etalon Traces.

For data collection, the oscillation averages out in the absorption and LIF signals with a large time constant. The multiple etalon traces affects the data analysis as the additional lines change the spacing of the points.

In addition, the temperature sensitivity limits operating times for the laser, as the environmental systems of the SPASS Lab cannot compensate for the immense waste heat emanating from the cryogenic compressors. On warm days, the laser over heats and shuts off.

Laser Effect on Data Post-Processing

Laser Power Drift

The Sacher laser power drifts over time seen in Figure 53 by observing the table absorption signal plotted in magenta. Note the intensity fluctuates from 5 V to almost 6 V during the middle of the scan. This drift prevents Igor® from automatically curve-fitting and determining the peak frequency location. Fortunately, the procedure includes a gating option allowing the user to manually bracket the absorption signal and calculate peak location. Also, the curve fit command in Igor® allows the user to define specific ranges within the data to fit a curve. Using constant scan settings keeps the absorption curve in the same relative position, providing a range for the curve fit command.

Frequency Hops

The Sacher laser also experiences frequency hops every ~21 GHz or 13-14 etalon resulting in a discontinuity of the etalon trace. These breaks appear in Figure 55 and Figure 56 plots generated by Igor® during post-processing. Figure 55 shows the etalon trace after Igor® smoothes the etalon curve and identifies the peak. Around point 13,000,

two etalon traces appear close together. Around point 26,000, a larger gap appears between two traces.

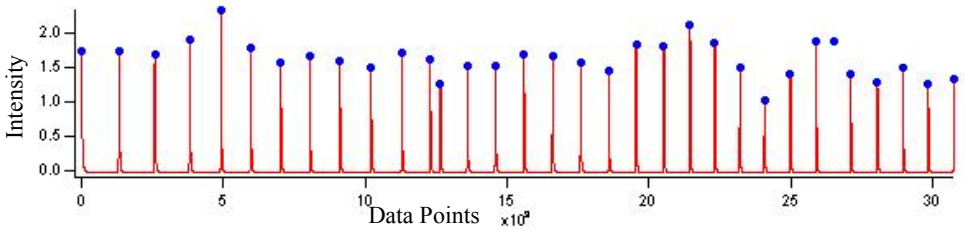

Figure 55. Igor® Plot of Etalon Traces.

Figure 56 shows the number of data points between etalon traces. Ideally, the plot should show a downward sloping straight line, indicating the number of points between traces is consistently decreasing. Instead, the plot shows a sharp decrease between points 10 and 11, and a sharp increase between points 25 and 26, matching the etalon traces in Figure 55.

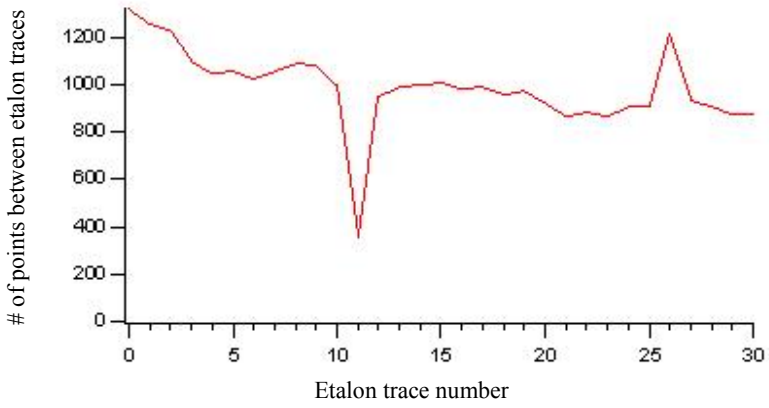

Figure 56. Number of Data Points Between Etalon Traces Before Processing.

All plots with wavemeter and etalon data correlate the discontinuous etalon traces with a jump in the frequency. A jump less than 1.5 GHz results in two etalon traces

spaced closer together. A jump greater than 1.5 GHz means a skipped etalon trace equating to a larger gap between traces.

The magnitude of jump determines how the user post-processes the etalon trace. The close traces are ignored as Igor® counts the number of etalon traces and multiplies by 1.5 GHz. Even though spaced close together, the double etalon trace accounts for the frequency hop. The only negative effects occur if the laser hopped at an absorption frequency as the case in Figure 51. Laser mode hopping may prevent the absorption or alters the shape introducing an error to the frequency center location.

In the other case, a skipped etalon trace leads Igor® into calculating a velocity using a separation frequency1.5 GHz less than the actual since the etalon count is one point short. This error equates to a ~1250 m/s reduction in the velocity calculation. Igor® solves this situation by inserting an additional etalon point between the gap, appearing as the floating point in Figure 55 and dip at points 26-27 in Figure 57.

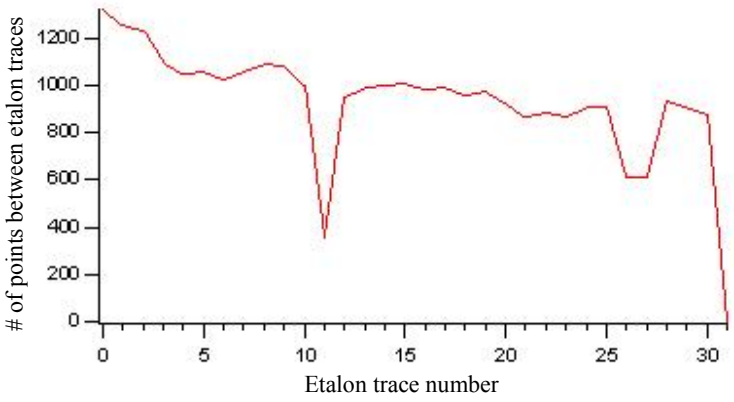

Figure 57. Number of Data Points Between Etalon Traces After Processing.

Statistical Error Analysis

Hargus uses an uncertainty of ±500 m/s but this value describes the overall error of the system. The statistical error quantifies the error of the data collected. The statistical error is the norm of the variance of the mean velocity, σ, and bias of the diagnostic tool, Δv.

A normal distribution curve provides σ and the type of curve depends on the number of samples taken at each point. For a limited sample size, a student-t with a 95% confidence provides the variance

$$\sigma = A\frac{\sigma_n}{\sqrt{n}} \tag{46}$$

where A is taken from a t-distribution table, σ_n, the variance of the sample and n, the sample size [70].

The bias takes into account the resolution of the etalon and rate of data point collection as defined by equation (47).

$$\Delta v = FSR + \frac{\text{Total Frequency Sweep}}{\#\text{ of data points}}\left[Ghz\right] \tag{47}$$

The statistical error is then calculated by

$$S.E. = \sqrt{\left(t\frac{\sigma}{\sqrt{n}}\right)^2 + \Delta v^{\,2}} \tag{48}$$

IV. Analysis and Results

Of the original objectives, this experiment completed the diagnostic tool and obtained comparable LIF data to previous research but was unable to fully validate the tool and collect new data on other thrusters. Absorption data was not taken.

This chapter details the LIF collection process, compares data collected with previous research and outlines the error correction process and results.

Collection Process

The first LIF signal at 823.16 nm provides a very strong and easy to work with absorption signal. Also, neutral xenon travels at speeds less than 300 m/s at thruster face in both radial and axial directions, a separation of ~0.36 GHz between the peaks [71]. Including the broadened line shape of neutral xenon from the isotopes, 823.16 nm provides a wavelength where both radial and axial LIF signals appear and fine-tuning of optics outside the chamber can be made to maximize LIF signals.

Figure 58 shows the etalon trace in blue, absorption in the table lamp in red and radial LIF in magenta for a collection at 823.16 nm in the center of the thruster channel at -13 mm on the Z-axis and 7 mm away from the thruster face on the X-axis. The changing diode temperature affects the etalon traces through thicker etalon traces, inconsistent spacing and a double trace near 180 seconds. This frequency inconsistency also influences the table absorption curve. The absorption curve does not display the four distinct peaks of neutral xenon at 823.16 nm as shown in Figure 11. The LIF signal reflects the humps of the absorption curve and may appear more distinct if the time

constant was set below 3000 ms. In this collection, axial LIF was not shown as a repressurization of the chamber revealed a misalignment of the axial laser.

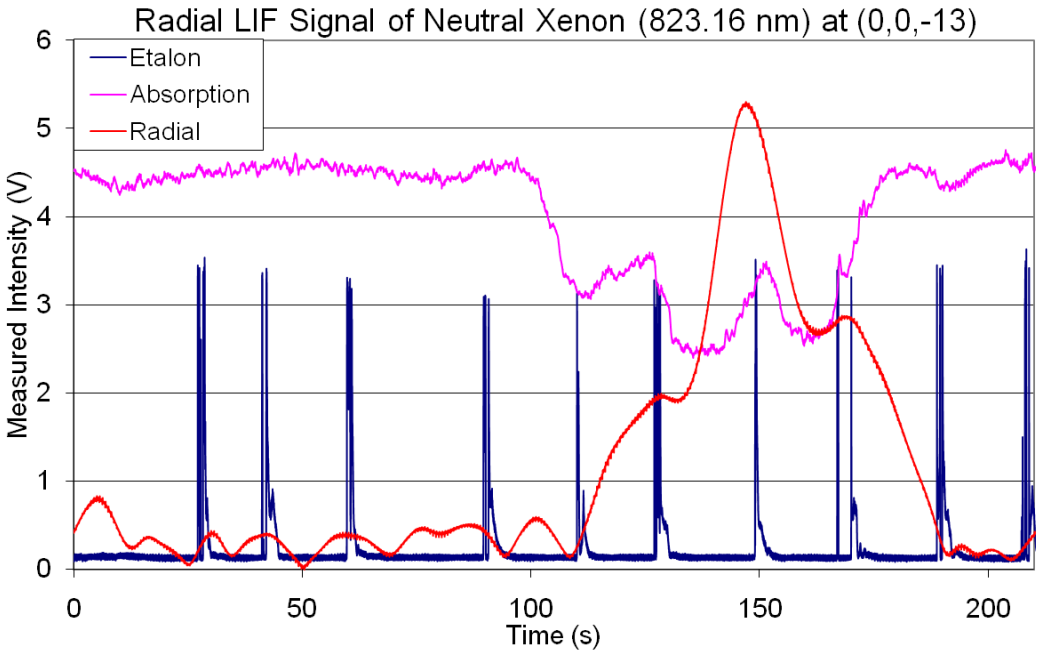

Figure 58. Table Absorption and Radial LIF Signal at 823.16 nm.

After repressurization, realigning and pumping down, inconsistent LIF signals appeared for axial and radial LIF at 823.16 nm. Switching to 834.68 nm revealed the strongest LIF signals collected during this experiment shown in Figure 59 and Figure 60, taken at the centerline with the thruster at 5 mm and 13 mm on the X-axis respectively. The table absorption curves are shown in magenta, the etalon and wavemeter in blue and green respectively and the LIF signals are red and cyan for axial and radial, respectively.

A comparison of the two plots shows absorption peaks at similar positions, not surprising since both plots used the same frequency sweep starting point, range and rate. The absorption curve also displays the power drift of the laser, increasing in intensity after 50 seconds and decreasing after 200 seconds.

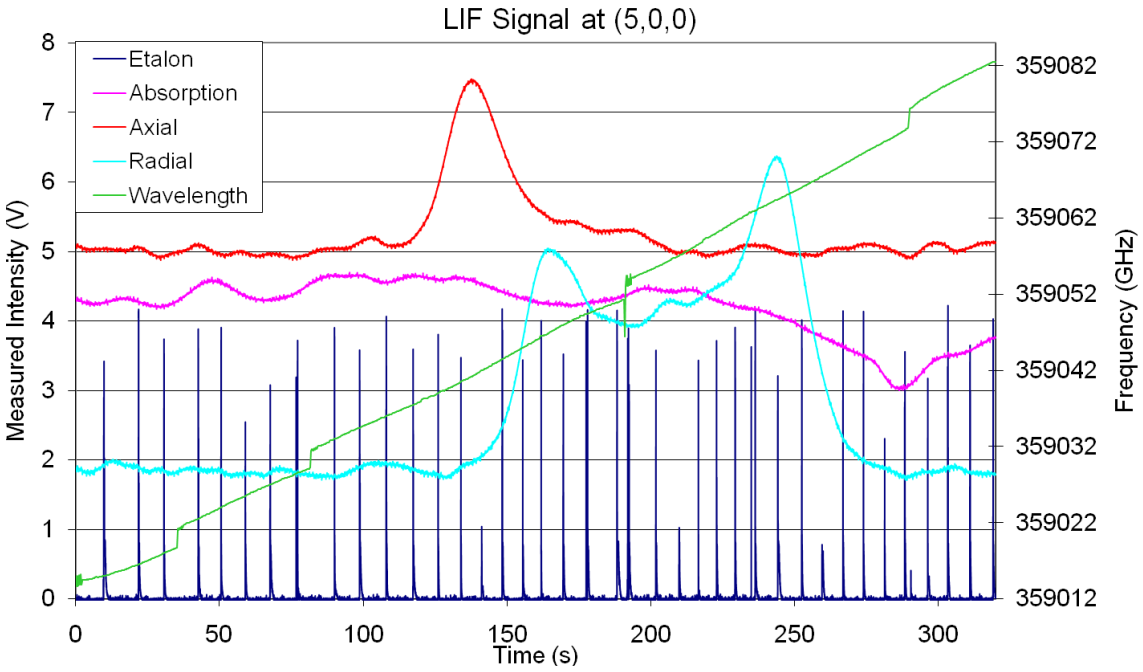

Figure 59. LIF at 834.68 nm on Thruster Centerline, +5 mm From Nose Cone.

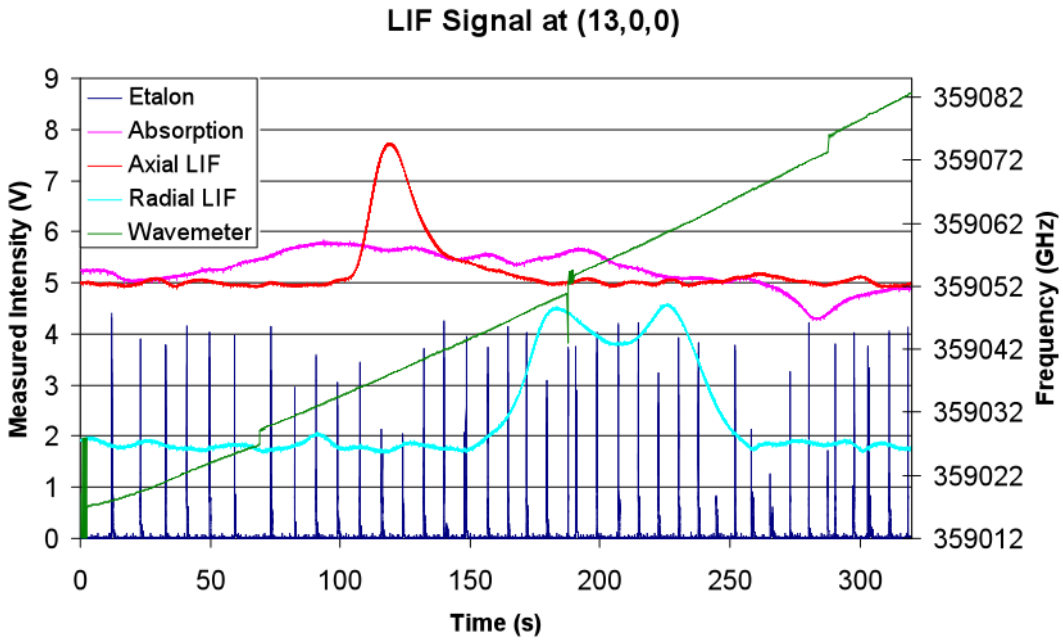

Figure 60. LIF at 834.68 nm on Thruster Centerline, +13 mm From Nose Cone.

The axial LIF plot for Figure 60 shifts to the left indicating a greater axial velocity at a farther distance from the exit plane, consistent with previous research on this 200W thruster, the Stanford Hall thruster and the 600W thruster [7, 28, 71-72]. The electric field extends out from the thruster face allowing the ionized xenon to accelerate outside the chamber. The axial velocities calculated to ~9934 m/s for the 5 mm and ~12,225 m/s for the 13 mm position and are aligned with the X-axis.

The radial LIF signal shows a double hump. Igor® analysis calculates radial velocities of -7599 m/s and 5134 m/s for the 5 mm position and -5114 m/s and 3018 m/s for the 13 mm position. These radial velocities are the Z-axis component of the velocity vector. These results indicate a bimodal response at the centerline and match the velocity plot of previous research on the same thruster [71]. The bimodal response results from the cross-channel interaction of the plasma and appears in a 600W thruster of the same geometry [28]. The divergence decreases farther down the plume and the separation angle at the 13 mm position is smaller than the 5 mm position.

Although opposite in direction, the radial velocities should have similar magnitudes. The 2000+ m/s separation indicates a bias caused by misalignment of the radial probe beam from the Z-axis or the collection lens not centered on the Y-axis. Another explanation is the asymmetry caused by the cathode placement had an effect on the radial velocities. Hargus' radial measurements were symmetric with respect to the cathode [71].

Final observation, a frequency hop exists in the middle of the absorption curves but these curves do not appear affected. The long time constant shifts the curves to the right; the sweep has already passed the absorption region before the frequency hop.

A series of data runs were programmed using the A3200 to translate the thruster and the LabVIEW® code to continually sweep the laser and write the data into individual files. This automated process collected 240 runs over six iterations and 24 hours. After 16 runs and 96 minutes, the DET10A battery died and only 129 runs were collected as room temperature and subsequent laser alignment prevented any additional data collect.

The detector provided feedback to the laser while in constant power mode. Without feedback, the laser intensity reduced and fluctuated as displayed in the magenta absorption curve in Figure 61. An absorption signal should have occurred between 250 and 300 seconds based on the scan settings. A closer look at ~260 seconds shows a slight dip, indicating a possible absorption signal, but the absorption is too small to fit a curve and determine the center peak location. The reduced laser output still provided enough power to generate LIF signals from the plume as indicated by the red and blue curves. Of the 129 runs collected, the absorption signal was unusable in 113 runs.

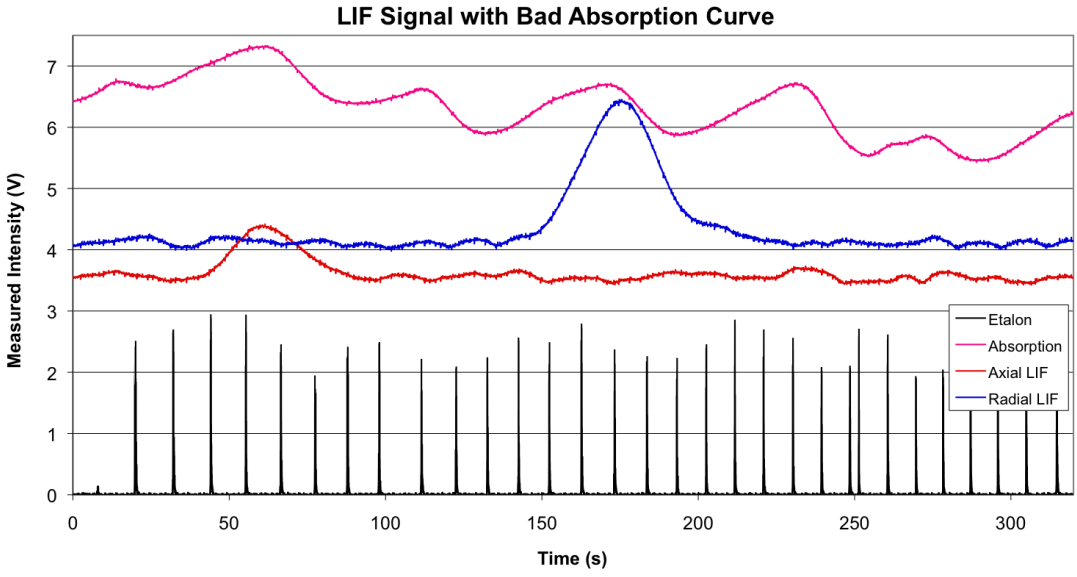

Figure 61. Data Run with Bad Absorption Curve But Good LIF Signals.

Comparison to Previous Research

Without a reference absorption curve, data analysis used the absorption results from an earlier run to process all the runs. All the scans started with the same settings so, the absorption curves and etalon traces should remain consistent between all the runs as was the case in Figures 59 and 60. Figure 62 shows the coordinate system and position of each run. A total of 40 different locations were scanned and divided into three groups, 1) across the thruster or acceleration channel in green from -8 to -16 mm at 1 mm increments on the Z axis and -2 mm on the X-axis, 2) across the thruster face in red from -16 to 16 mm using 2 mm increments on the Z-axis and +3mm on the X-axis, and 3) axially away from the thruster face by varying the X-axis while keeping the Z-axis position at -12 mm. The increments varied from 1 to 4 mm from an X position of -7 mm to + 30 mm. Each position had at least three scans while across the thruster face had four runs per position

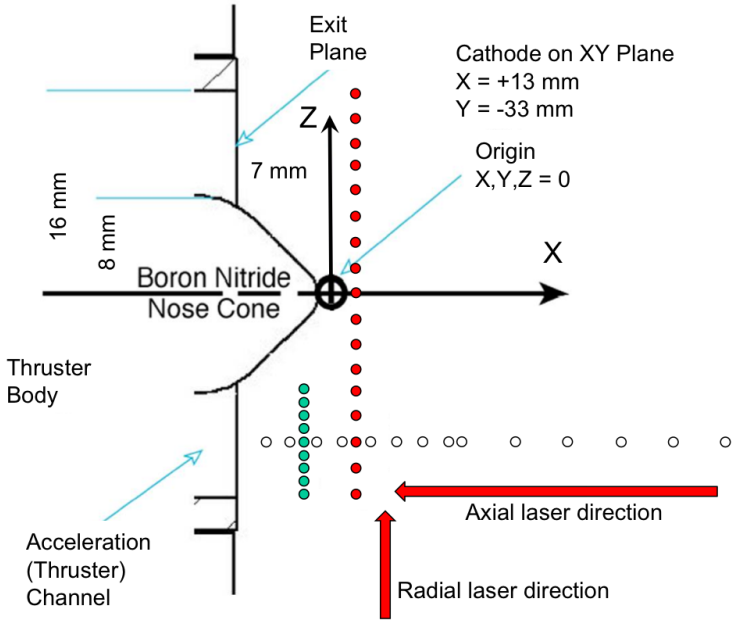

Figure 62. Coordinate System and Position of Each Run.

Figure 63 presents a sweep along the Z-axis near the thruster channel 5 mm away from the thruster face showing the velocity with each position on the Z-axis. The red marks indicate axial velocity and blue the radial. The thruster position partially obscures the collecting optics so -2 mm on the X-axis was the closest point near the thruster face providing consistent data. This plot also includes data taken by Hargus, depicted as an „x' or asterisk, at the thruster face at a distance of -7 mm from the origin or next to the thruster face [71].

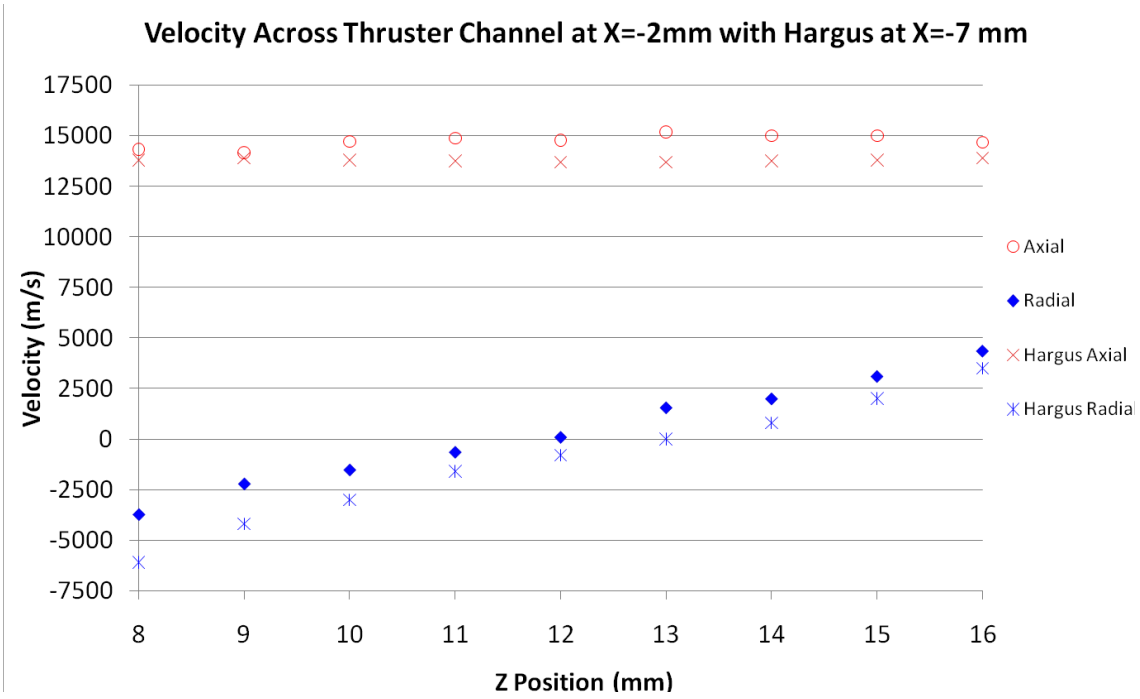

Figure 63. Comparison of Velocity Across Thruster Channel [71].

Comparison of the plots reveals similar trends and good agreement to Hargus, a constant axial velocity across the thruster channel and a radial velocity starting negative near the nose cone and becoming positive by the outer channel. The axial velocity is approximately 15,000 m/s while Hargus is closer to 14,000 m/s. Higher values are

expected since axial velocities increase further away in the near-field due to the extension of the electric field past the thruster channel opening.

The radial velocities follow a linear slope, starting negative closer to the nose cone and becoming positive near the thruster edge. The negative velocity indicates a red shift; the ions are traveling away from the probe beam towards the center of the thruster. The positive velocity points to the plume diverging to the thruster edge. The overall shape obtained agrees with previous research except for the location of the zero radial velocity. Previous research shows the zero radial velocity at 13 mm but data collected shows 12 mm as the crossover from a negative to positive radial velocity. This indicates the center of the thruster nose cone is positioned one mm higher than the XY-plane and explains the difference of the crossover locations. Another explanation is the LIF lens is not focused on the XY-plane but collecting just above this plane. This essentially creates the same bias as an off-centered nose cone and coordinate axis. More than likely, a combination of both biases yields the change in zero velocity position.

One similarity is the slope of the radial velocity trend line. Data shows a similar slope indicating the divergence is consistent across the thruster channel regardless of distance from the thruster face. Moving farther away at an X-axis position of 3 mm agrees with this as shown in Figure 64.

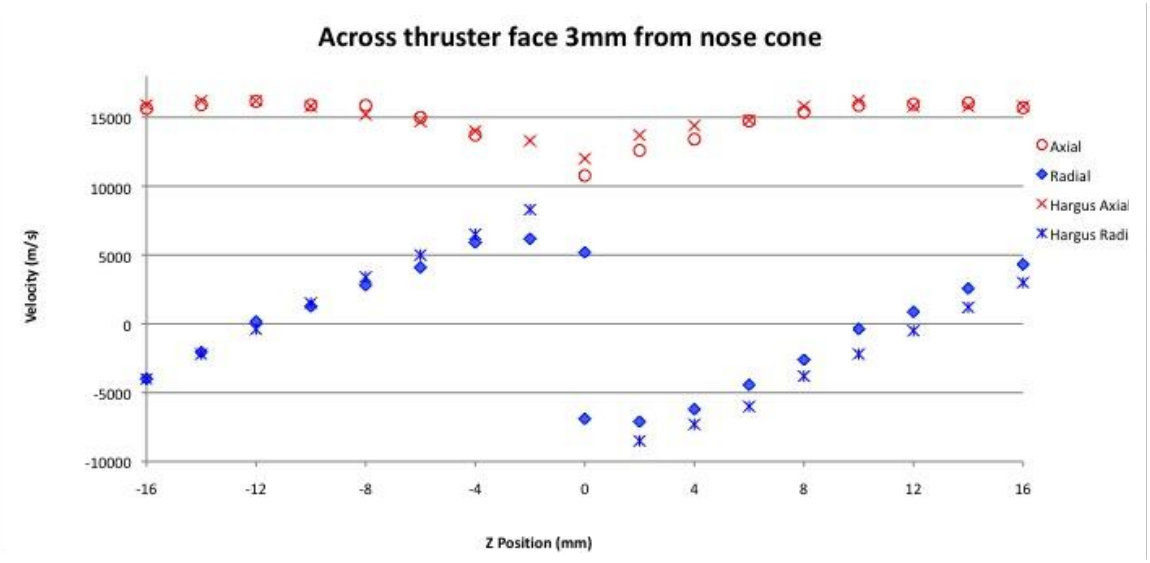

Figure 64. Velocity Field 3 mm Beyond Nose Cone Across Thruster Face [71].

Figure 64 illustrates a scan across the entire thruster face sweeping from -16 to 16 mm at a constant axial position of 3 mm away from the nose cone. As mentioned before, the slope of the radial velocity, in blue, remains consistent resulting in a greater magnitude near the nose cone.

The radial velocity shows a double point at the center of the thruster confirming the cross-channel plume interaction also seen in Figure 59 and Figure 60. The radial plot also displays a symmetry confirming the assumption this thruster is axisymmetric. In addition, a positive shift in the radial velocity occurs for the Z-axis between +2 to +16 mm similar to the sweep across thruster channel. This supports the notion of an off-centered coordinate system or LIF collection volume creating a positive bias. On the other side, the off-centered coordinate system and LIF collection volume biases cancel each other out for the negative Z-axis points between -2 to -16 mm. This cancellation results data points matching previous results.

The axial velocity, plotted in red, shows a maximum in the center of the acceleration channel and stays fairly constant across the entire channel from 8 to 16 mm and -8 to -16 mm. As the scan moves off the thruster channel and closer to the nose cone, axial velocities decrease and combined with the increasing radial velocities, the plume diverges near the thruster center, agreeing with previous results [71].

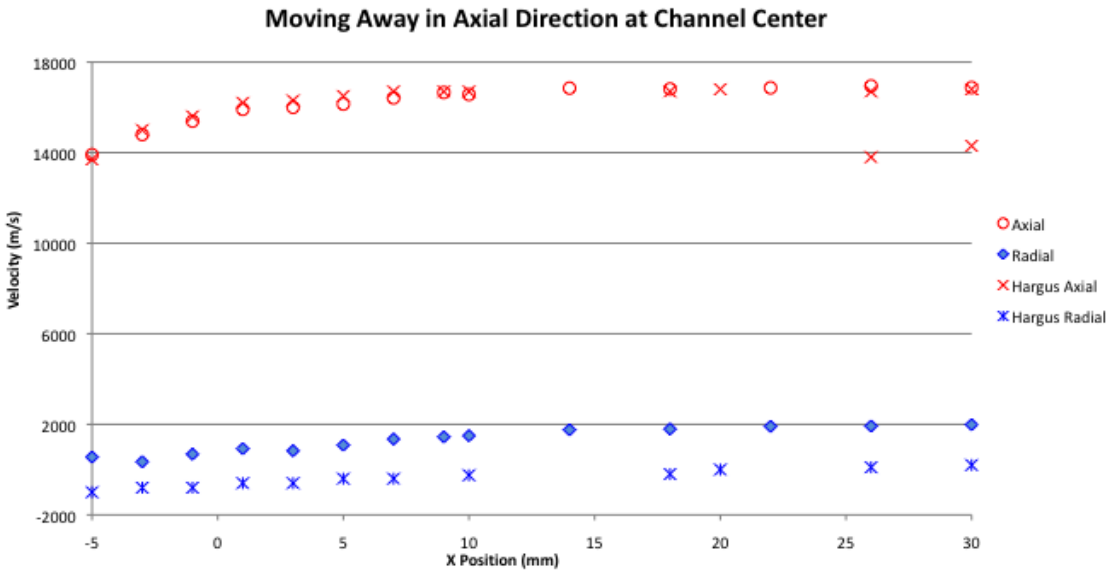

Figure 65. Velocity Moving Axially Away from Thruster Face [71].

Figure 65 displays a comparison with previous research of the velocity at the acceleration channel center, 12 mm from the nose cone. The data points represent a sweep axially away from the thruster face stopping at 30 mm on the X-axis. Both plots exhibit an increase in axial velocity from the thruster face to past the nose cone over the first 10 mm. The acceleration confirms the electric field extends outside the thruster chamber before the ions plateaus at a maximum velocity. Hargus calculates a plateau of 16,800 m/s compared to the 16,950 m/s measured by this research, within 1% difference [71]. The research did not capture the bimodal effects beyond 25 mm when mixing of

the plume occurs from the cross-channel interaction. These points appear as a secondary and slower point on the axial signal.

Finally, the radial velocities have similar trends of slightly increasing while moving farther from the thruster face. This indicates the center of the thruster channel is not aligned entirely with the X-axis downstream. In addition, Figure 65 shows a similar positive shift as the radial velocity in Figure 63 for the same reasons discussed before.

Applying an Error Correction

While processing the data, runs #121-129 seemed much higher than runs #1-9 although both sets covered the same data points across the thruster channel from 8 to 16 mm on the Z-axis with the X-axis at -2 mm. Figure 66 shows runs #1-9 in blue, #121-129 in magenta and the average of the four runs as red asterisks. Subtracting the corresponding data points and averaging yielded a difference of 1254 m/s, a 9% difference. Almost all the points in runs #1-9 and a couple of points from runs #121-129 were outside the 500 m/s error bars. The use of the same reference absorption curve had introduced an error.

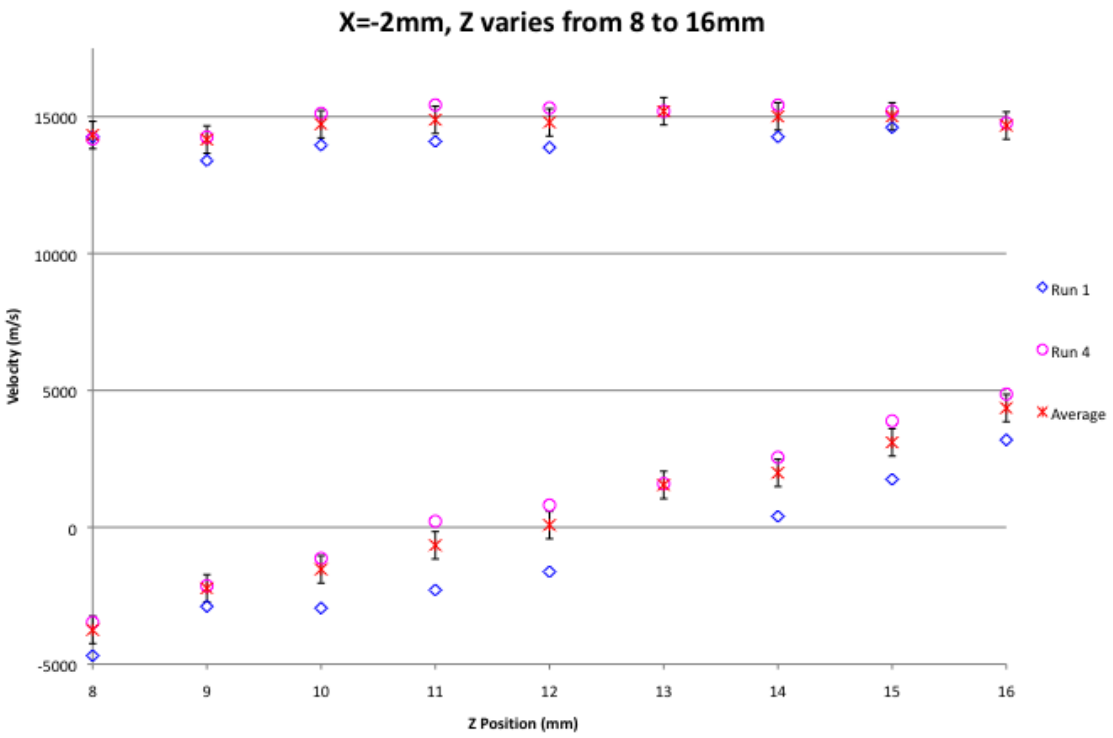

Figure 66. Plot of Runs 1-9 and 120-129 with Four Run Average.

This laser tended to frequency drift due to the diode laser temperature fluctuations. Wavemeter data was not recorded during the scan but data taken prior to run #1 and just after #129 showed the frequency sweep starting values were 35928.3 GHz and 35929.8 GHz respectively. The 1.5 GHz difference equated to a bias of ~1254 m/s.

The path length, l, within the etalon cavity is assumed to remain constant – in actuality, thermal conductivity and temperature changes slightly affect the path length. Therefore, etalon constructive interference occurs whenever the wavelength divides evenly into the cavity length or when equation (49) yields an integer value for m.

$$m = \frac{l}{\lambda_{air}} = \frac{lcn_{air}}{f} \tag{49}$$

Wavelength converts to frequency using speed of light and accounting for the index of refraction in air, n_{air}. Since each scan started using the same conditions, each etalon trace corresponds to a specific frequency. Comparing these traces for each run indicates how the frequency drifts as shown in Figure 67 (a-d). These plots represent the etalon traces plotted against the data points. At a 100 Hz collect, each data point equals 0.01 seconds.

While observing the plots, focus on the fourth etalon trace and its proximity to the 5000 data point on the X-axis. Plot a) is the first data point whose absorption curve acts as the reference to calculate velocity. In plot b), the fourth etalon point in #8 is after #1 indicating the frequency sweep started lower than 35928.3 GHz. In c), the #81absorption curve shifts to the left of #1 and plot d) displays #121 shifted much farther to the left. Both c) and d) signify the frequency sweep starts higher than 35928.3 GHz and in #121, much closer to 35929.8 GHz.

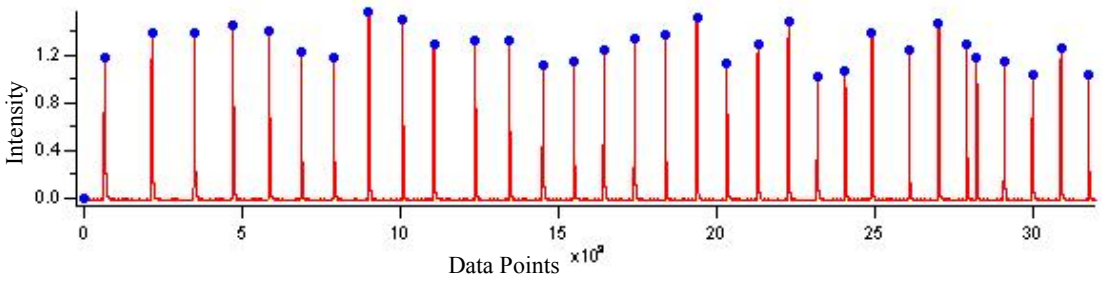

a. Etalon Plot from Data Point #1

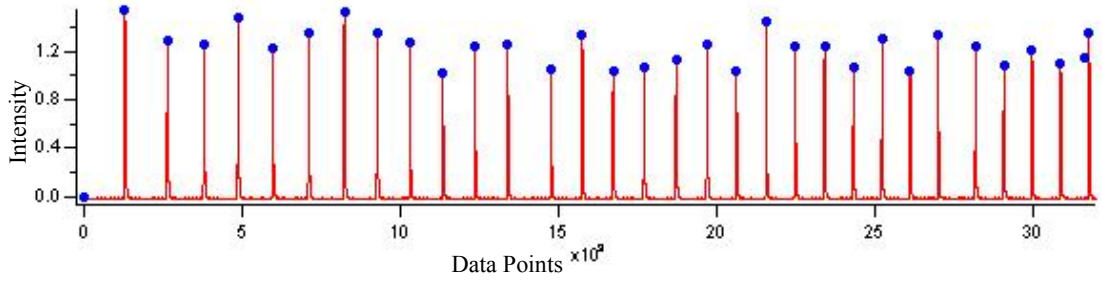

b. Etalon Plot from Data Point #8

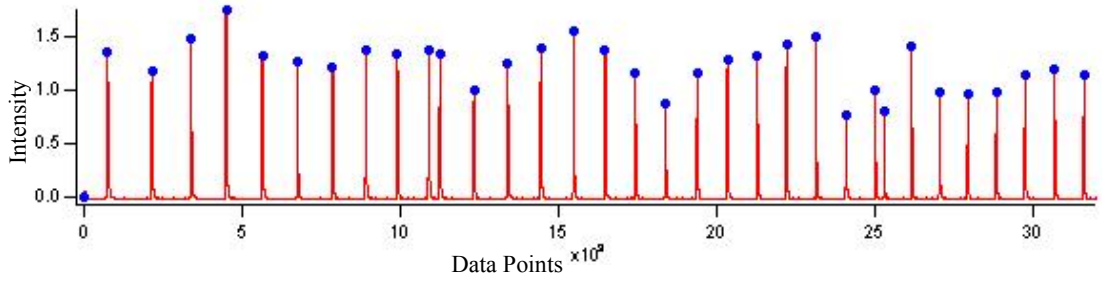

c. Etalon Plot from Data Point #81

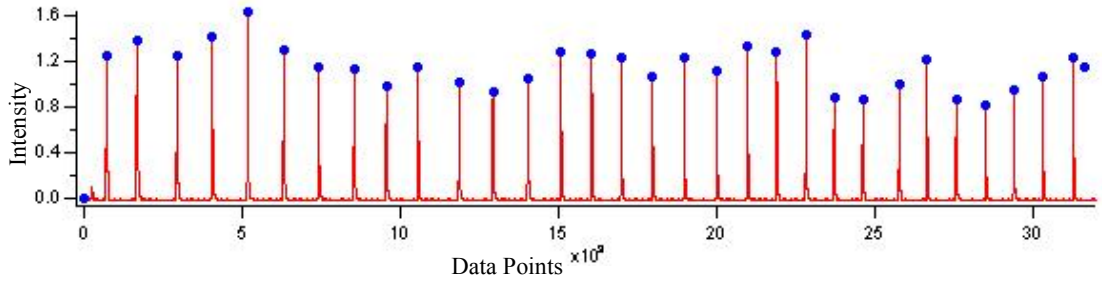

d. Etalon Plot from Data Point #121

Figure 67 (a-d). Different Etalon Plots Taken Throughout the Data Collection.

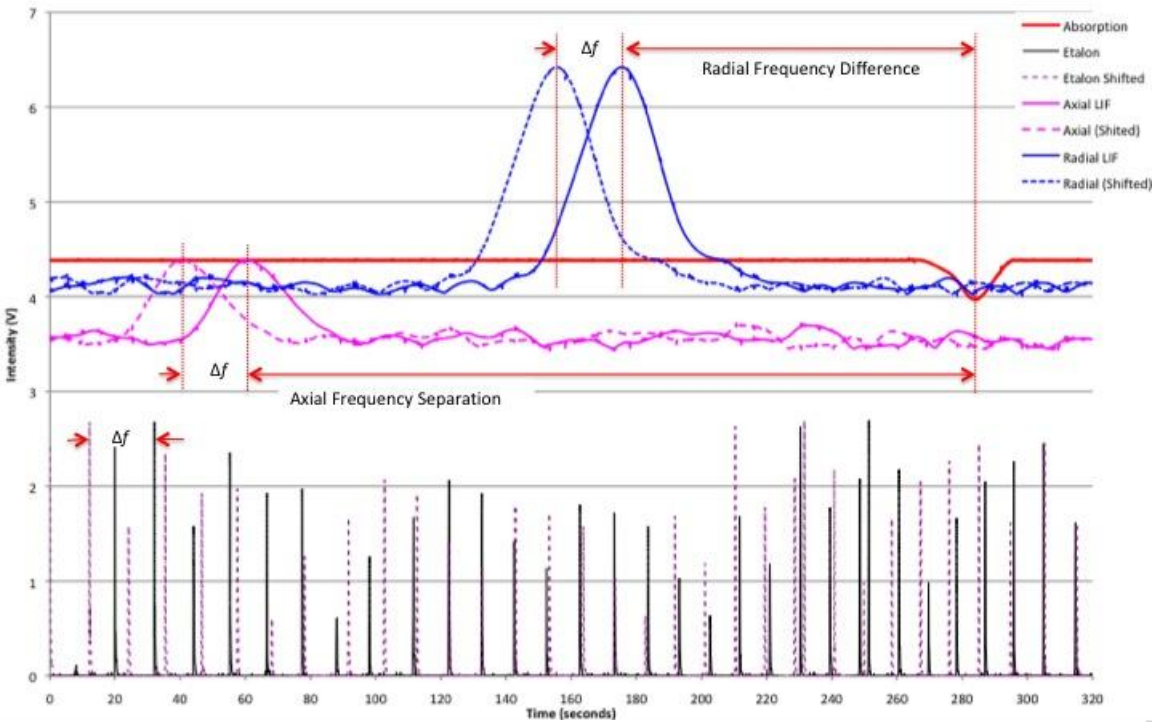

Figure 68. Example of Error if Using Same Absorption Curve.

Figure 68 shows the effects of using a common absorption curve and shift in starting frequency. The solid lines represent the original points and the dotted lines the LIF and etalon traces shifted to the left by Δf. A shift in the starting frequency will shift all the LIF curves and etalon trace by the same amount while the absorption curve stays at the same point. By calculating the etalon shift in Figure 67 (a-d), applying the Doppler shift equation converts the frequency shift to a velocity error for each run.

Figure 69 shows the correction from frequency shift converted to a velocity correction in m/s compared to time. The initial runs required additional velocity as the frequency started higher. Eventually, the etalon points swings to the left requiring removal of extra velocity. The last run shows a negative ~1100 m/s correction closely

matching the wavemeter data showing the ~1250 m/s difference due to the frequency shift from run #1 and #129.

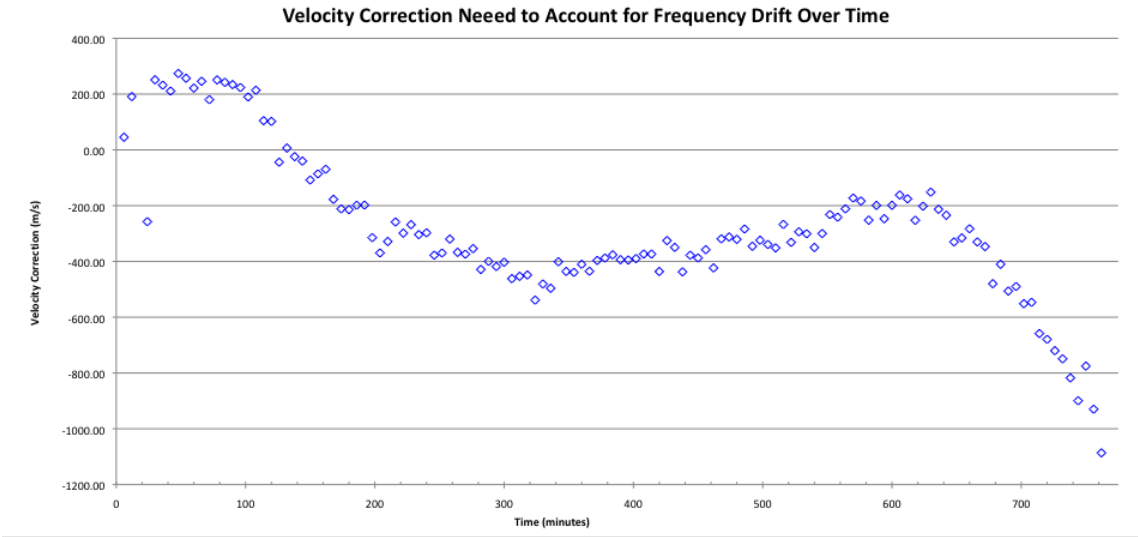

Figure 69. Plot of Velocity Correction to Account for Frequency Drift with Time.

Determining velocity correction starts with Igor® finding the data point locations of the etalon peaks for the first six etalon traces in all the runs. The shift is determined by the etalon shift from the first run. The data is averaged out and denoted as "avg drift." Next, the data points between the etalons is averaged out for each run and denoted as "avg space." The frequency shift is calculated by

$$\text{frequency shift} = \frac{\text{avg drift}}{\text{avg space}} \times 1.5 \text{ [Ghz]} \tag{50}$$

Equation (22) converts the frequency to a velocity correction using a f_o of 359028 GHz and this is plotted against time in Figure 69.

Applying the correction to each run results in Figure 70. Compared to Figure 66, many of the points outside the error bars reside inside the error. On the other hand, the

maximum velocity from Figure 66 reduces from 16,950 m/s to 16,570 m/s, just over 1% difference from the 16,800 m/s.

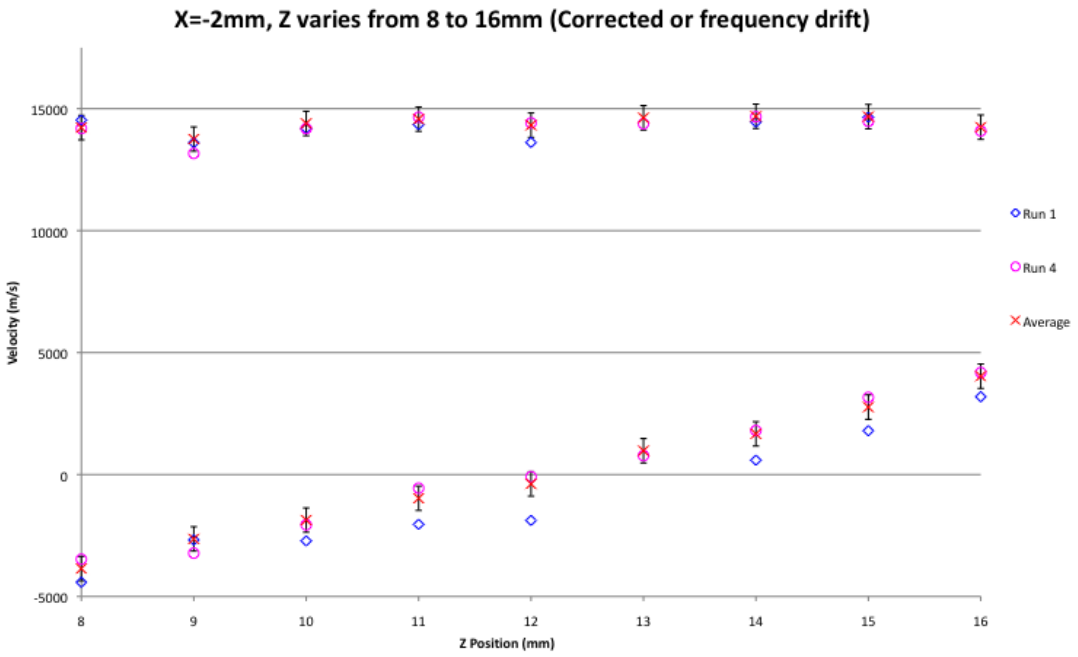

Figure 70. Plot of Runs 1-9 and 120-129 Corrected for Frequency Drift.

The statistical error calculates to ~506m/s, just over the 500 m/s error bar. The mean variance from the student-t distribution dominates the error as the etalon finesse and data points used resulted in a Δv equal to ~1m/s. Breaking down the mean variance, the small sample size (n = 3) results in a large student-t multiplier as the variance of the sample is only ~213 m/s. If additional data is taken and the sample size variance remained the same, increasing the sample size to n = 5 reduces the error to ~253 m/s. Table 2 lists the statistical error by varying sample size while keeping the sample variance of ~213 m/s and Δv constant.

Table 2. Statistical Error with Constant Sample Variance

# of Runs	2	3	4	5	6	7	10	15
Student t Multiplier (A)	12.71	4.303	3.182	2.776	2.571	2.447	1.812	1.753
Statistical Error (m/s)	1830	506	324	253	214	188	117	92

V. Conclusions and Recommendations

Conclusions of Research

The diagnostic tool has demonstrated the ability to collect both axially and radially LIF signals for both neutral and ionized xenon. The neutral xenon was excited at and LIF signals were collected at 834.16 nm. The ionized xenon was stimulated at 834.72 nm but the LIF collected at 541.9 nm. The neutral absorption line at 834.68 nm provided the stationary reference to measure the frequency shift.

In order to induce stimulated absorption, the laser needed to be brought into the vacuum chamber using fiber optics to prevent an etalon issue when passing the laser through the vacuum chamber window. The etalon feature affected the laser signal preventing absorption by the xenon.

Laser alignment, power setting and temperature control were other factors to consider in obtaining a good laser beam quality for absorption and LIF signal. Without the proper adjustments, the laser would multi-mode precluding absorption and causing frequency hops led to inconsistent etalon traces. Other factors affecting the etalon included the temperature fluctuations of the diode laser causing a random frequency change of the laser.

After making the proper adjustments for the laser, the LIF signals collected yielded velocity data and plume plasma characteristics similar to previous independent research on the same thruster. An analysis technique was developed to accurately measure the velocity. This technique incorporated error correction using the etalon traces to quantify frequency drift by the laser over time. This velocity data mapped out the

plasma plume and showed the bimodal effects near the thruster centerline caused by the cross-channel plume interactions.

Recommendations for Action

The reliability of the laser plays a significant factor in the functionality of the tool. Attaining laser performance consistency allows researchers to concentrate on data collection and analysis as opposed to maintenance. The laser ran consistently during the winter months when ambient air temperature was at 17-20° C (63-68° F). To improve dependability, install a water chiller to the base of the laser to maintain temperatures within temperatures during the winter. A chiller stabilizes the master diode laser temperature reducing the oscillation of the laser frequency and prevents the amplifier diode laser from overheating.

Keeping the laser running for longer periods allows for the collection of more data, especially during daytime temperatures when the laser can overheat. The shortened data inhibits statistical validation of this diagnostic tool. Before applying the tool to another thruster, collect more data to increase the confidence in the repeatability. Concentrate efforts in regions next to the thruster channel opening where thruster obscures optics. This concentration requires a repositioning of the collection optics closer to the axial axis and may provide velocities within the acceleration channel of the thruster.

The vacuum chamber windows may limit the rearrangement of the optics to desired location. For more flexibility, reinvestigate using fiber optics to collect the LIF signal. Previous attempts used 50.8 mm lens at 1000 mm away resulting in an *f*/20 and

focusing the light into a 0.6 μm fiber. To increase signal, switch to a larger lens with a small focal length to decrease the *f/#* and use a larger fiber core, i.e. 1-μm, to limit losses into the fiber. A 1-μm multi-mode fiber will improve collection of LIF on the table at 834.68 nm. The intensity of neutral xenon at 834.68 is comparable to the LIF signal at 541.9 nm for ionized xenon.

If replacing the fiber optics is under consideration, switch to single-mode fiber optics to increase the resolution of the tool by decreasing the waist size of the lasers. Single-mode fiber should reduce the divergence of light leaving the fiber and can collimate into a smaller waist. Experiment using off-the-shelf fibers and collimator combinations on the optical table before ordering custom fiber and feedthroughs for the vacuum chamber.

In addition to matching the collimator on the table, install the ideal collimator opposite the radial laser to allow measurements of the absorption of the laser from within the plume. Comparing intensity using Beer's law maps out the ion density of the plume. The current set-up limits collection to three signals, lamp absorption, axial LIF and radial LIF. Another lock-in amplifier dedicated for absorption within the plume will prevent separate runs and allow all the data to be written into one file.

With all the data in one file, take advantage of Igor® to automate the data analysis. Igor® has the ability to open, read, analyze and close sequentially numbered files. Format the output data into another file or into the command window in such a way to make importing into Excel simplified. The only concern is the etalon trace verification. Currently, processing the etalon traces requires manual observation to

decide if interpolation is required and where. Instead, the user can modify the function, which counts points between etalon traces, as a method to automate.

Recommendations for Future Research

Complete the objectives intended on the 1500W thruster. Previous research using different diagnostic techniques and intrusive probes provides another method to baseline this LIF and absorption tool. In particular, ascertain if this absorption and LIF technique can accurately measure thrust from doubly ionized xenon particles.

In addition to mapping out velocity from xenon as a propellant, this technique can adapt to measure the thruster using a different propellant. Currently, the SPASS Lab has capability to run the thrusters using krypton as the propellant. First step is to identify transitions of singly ionized krypton with a strong LIF signal. Then, determine which neutral absorption line to use as a reference to count the etalon traces. The frequency separation between the absorption and LIF lines need to fit within the laser's frequency sweep range. As with xenon, LIF collection frequency is not limited to the same laser frequency, Kr^+ has lines at 728.982 nm, 740.706 nm or 752.448 nm. Additional study would determine the best laser and LIF frequencies to excite and collect at respectively.

Besides flexibility for the propellant type, the LIF diagnostic tool coupled with fiber optics for the probe beams and LIF collection provides a versatile tool in terms of tool placement and testing location. The optics only requires an unobstructed view of the desired collection volume. Also, the addition of a third probe beam, orthogonal to the radial and axial beam, provides 3D measurements. 3D measurements are not as significant for an axisymmetric cylindrical thruster as the ones tested, but Busek is

building a three-axis Hall thruster. Many current diagnostic tools are spatially limited and the translation stage lacks any rotational capability, thereby, limiting the types of data collected from a three-axis thruster.

To measure the three-axis thruster, align the LIF optics at a vector 45° to the probe beams or at a vector (1,1,1) if the probe beams are vectored to (1,0,0), (0,1,0) and (0,0,1). Placing the corner common to all three thruster faces at (0,0,0) allows measurements across all discharge chambers without having to reposition the thruster. In particular, a 3-D tool can map the plasma interaction from each plume and uncover asymmetries or off-axis thrust.

Appendix A – Lab View® Software Description

Lab View® Virtual Interface (VI)

The LabVIEW® code control provides the voltage output to the laser piezo for the frequency sweep while simultaneously recording the data through the National Instrument Data Acquisition Devices. The program contains three loops to accomplish this effort.

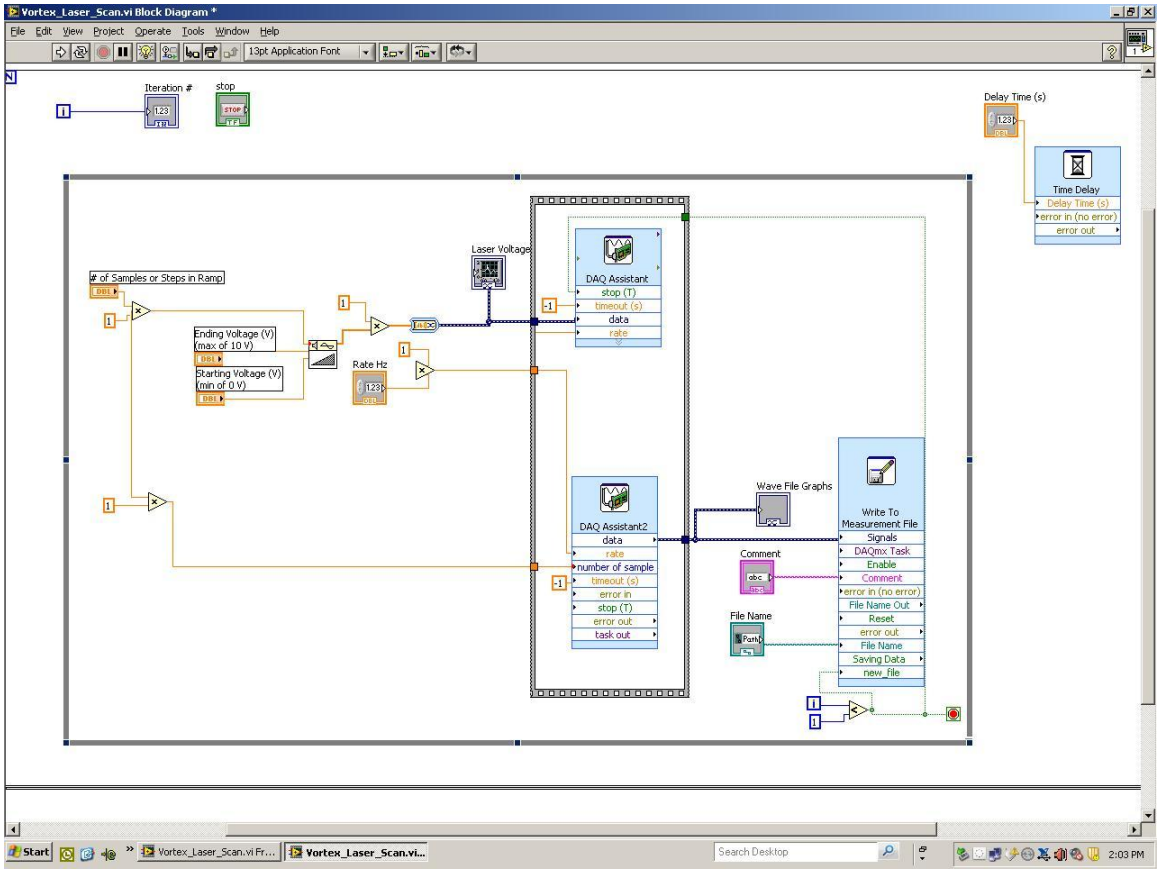

Figure 71. Screenshot of LabVIEW® Code, Back End, to Sweep and Collect Data.

The outermost loop is a FOR loop providing the user an iteration option without having to use the "continuously run" option in LabVIEW®. This also provides a counter incrementing the scan count. Each iteration saves into separate a file with sequential numbers appended to the end (i.e. Test_1.lvm, Test_2.lvm, Test_3.lvm, etc). A "Path"

button allows the user to choose destination and file name. The program separates the data into the following columns, A) time in seconds or blank, B) Etalon traces, C) Table Absorption Voltage, D) Axial LIF Voltage, D) Radial LIF Voltage and E) Vacuum Chamber Absorption Voltage. The user can change these options through the "Write to Measurement File" properties box.

Within the first FOR loop is another FOR loop and Time Delay. The FOR loop has a counter set to "1" and contains the blocks to set scan options, execute and record. The Time Delay allows the user to coordinate this LabVIEW® VI with the A3200 code commanding the translation stages, creating automated collection.

Within the second loop is the wire and block diagram controlling the laser and data collection, the "DAQ Assistant" and "DAQ Assistant2" blocks respectively. The user needs to define a starting and ending voltage. The voltage is limited to between -10V to +10V and is further constrained by the gain of the voltage amplifier and laser piezo limit. For instance, if the piezo has a -20V to +120V and the voltage amplification is -12×, the voltage setting is limited to -10V to +1.66V to prevent damage to the piezo.

The VI then creates a linear ramp based on the starting and ending voltage and divided into a number of steps equal to the "# of samples" as defined by the user. A "rate" option in Hz defines the collection speed so the scan time length is "#of samples" divided by the "rate". The code wires both the "# of samples" and "rate" numbers to both DAQ Assistants so the frequency sweep and data collections times are the same. A "Frame" loop encapsulates both DAQ Assistants to help with timing. Without the loop, one DAQ Assistant starts before the other. The scan and data collection will start after all

the required data is “gathered” at the frame border. Turning on the “light bulb” in LabVIEW® shows the progression of the code as it runs.

One unresolved issue is the disconnect between the “# of Samples” and the DAQ Assistants. For example, using 20,000 pts and 100 Hz on the “Front End” and the DAQ Assistants options set to 10,000 pts, “DAQ Assistant” performs a frequency scan in 100 seconds while “DAQ Assistant2” collects data for 200 seconds. The user needs to manually coordinate the DAQ assistants to match the “# of Samples”.

Of useful help is the manual voltage setting by viewing the “Properties” of “DAQ Assistant”. Here, a manual square or triangle voltage signal can be sent continuously to the laser for diagnostic purposes if the collection type is set to “Continuous” from “N Samples”. In conjunction with the wavemeter, this setting provides the quickest method to determine starting and stopping voltage values.

Timing for Automation

The code does not run instantaneously. LabVIEW® has a time delay, seen on the back end as the wiring diagram executes. In general, it takes ~14-16 seconds for the laser scan to start once executed. It takes an additional 5-8 seconds to write the data after the scan. Therefore, set the time delay to a value greater than 30 seconds plus the overall scan time. Note, there is a another holdup of ~3 seconds to execute the overall FOR Loop before one “Time Delay” finishes execution and the next “Time Delay” starts.

Appendix B – A3200 Translation Stage Software Description

The A3200 controls the translation stages within the chamber. It can be programmed or run manually. The following will describe using the A3200 program to calibrate and time the program for use with LabVIEW® to automate data collection.

Upon start-up, the program defaults the position to zero and needs to be "Home". Prior to calibrating the stages, ensure anything attached to the translation stage has a clear path as the A3200 moves the stage to the extreme -X, -Y and -Z position to reset the limiter.

The A3200 manual details the list of available commands. The commands used to help with automated data collecting are described below. See the manual for exact command structure.

- DWELL: instructs program to wait
- GLOBAL: defines a global variable. Used for the scan time.
- LINEAR X-2: moves the translation state
    - INCREMENTAL: Moves X by -2mm
    - ABSOLUTE: Moves to position of X = -2mm.
- RATE: Rate of movement. Movement time is ~distance/rate.
- REPEAT and ENDREPEAT commands defines loops
- G92 X0 Y0 Z0: Redefines the current position as the new local coordinate system point of (0,0,0)
- G82: Clears the local coordinate system

Automating A3200 with LabVIEW

Automating with LabVIEW is more about coordinating the time to repeat. As currently designed, LabVIEW requires 3 seconds plus the Time Delay for one iteration. Each A3200 run is the time to move plus the scan time.

For an example run, 32,000 data points collected at a 100 Hz rate requires 320 seconds to collect. A Time Delay set to 360 seconds provides a 40 second buffer between scans for moving the thruster. Total iteration in the LabVIEW is 363 seconds when including time to loop back into the Time Delay. For the A3200 side, all moves are made in 4 seconds and the DwellScanTime variable set to 359 seconds to equal 363 seconds.

The user can operate both programs from the same computer using Remote Desktop. Typically, start A3200 first and when the thruster reaches the initial starting point and DwellScanTime starts countdown, initiate the LabVIEW® program. This splits the buffer time so there are 20 seconds between collects and thruster movement.

Appendix C – Igor® Code and Description

Modification to Code

The current Igor® code, "v2.7_analysis_F_MASTER.pxp" comes from Dr. William Hargus at AFRL at Edwards AFB. This code has been modified and saved as "AFIT - v2.7_analysis_F_MASTER".pxp. The differences between the codes are, A) the etalon FSR and B) the names Igor® assigns the waves as it loads, C) the "Graph2:wfcheck" plot has minor tick units, and D) velocity and curve fit information displayed on the command window.

Edwards has an etalon with a FSR of 300 MHz while the current AFIT set-up has a 1.5 GHz. Throughout the code, IGOR will multiply by the FSR, so a global search was performed in the procedure file "Proc0" on "0.3" and manually replaced by "1.5".

The waves – what IGOR refers to as the columns in a file –are a) wave0 - the etalon, b) wave1 - the table absorption, c) wave2 - LIF1 and d) wave3 - LIF2. When loading the file, the appropriate columns require a naming to match that convention. IGOR® automatically names the columns in sequential order, "wave0, wave1, wave2, wave3, wave4, and etc." if no waves are currently loaded. The output file from LabVIEW has columns as follows, a) Time, b) Etalon, c) Table Absorption, d) Axial LIX and e) Radial LIF. Loading this file directly into IGOR, the user needs to rename each wave (b-e) to match previous naming conventions. To speed up the process, the IGOR procedure file is altered skipping the time column so the naming convention is as follows, a) wave1 - the etalon, b) wave2 - the table absorption, c) wave3 - LIF1 and d) wave4 - LIF2 allowing the user to "Load" the file without changing any wave names.

The following code, “ModifyGraph minor(bottom)=1,sep(bottom)=1” was added after “Check(ctrlName)” in “Proc0” to add minor tick lines to a graph assisting in resolving the etalon traces.

Finally, the curve fit information and velocities calculated are recorded into the command window facilitating cutting and pasting and keeps a historical record in the command window.

Additional Dependent Modification

The „Autofit’ function in the procedure file contains commands to automatically fit all three waves with a Gaussian curve. The commands for each curve are essentially copies except for the absorption curve. The absorption curve fluctuates causing Igor® to improperly fit the curve. If using the same run conditions, the absorption curve remains relatively fixed. This allows the modification of the curve fit command to change the fixed data range. For example, the command, “CurveFit/Q gauss wave_abs[20000,32000] /D” instructs Igor® to only look fit a curve between data points 20,000 to 30,000. These values change depending on the number of data points collected and location of the absorption curve.

Processing Data

The following lists the steps used to process each file.

1) Ensure all graphs and are killed by using the buttons on “Panel1”.
2) “Load” file through “Panel0”.
3) On “Panel”, go will process the etalon trace. Resolve any etalon trace anomalies, i.e. double points or missing points due to frequency hops, using the ouput plots for assistance.

a. If extra trace, select the etalon point number in “pt1” and press “delete”

b. If trace needs to be added, locate the starting and ending points in “pt1” and “pt2”

c. “Redo” will clean any mistakes and reset the plots and etalon traces

4) Click on “Trim” and select “Flat” or “Linear” to select the best presentation of the LIF and absorption curves.

5) “Autofit” will attempt to fit each signal with a Gaussian curve and calculate the peak location and width. Double-check these numbers in Panel0 for accuracy.

a. To manually fit a curve, under “Graph7” is a circle with a cross labeled “A” and a square with a X labeled “B”. Drag these cursers to the beginning and the end of the curve requiring bracketing.

b. Select the “Go” corresponding to the curve.

6) Calculate Velocity.

7) The “VDF” section in “Panel1” to calculate energies was not used in this experiment.

Bibliography

[1] M. Blair and D. DeGeorge, "Overview of the Integrated High Payoff Rocket Propulsion Technology (IHPRPT) Program," *51st International Astronautical Congress*, Rio de Janeiro, 2000, pp. 1-10.

[2] D. M. Goebel and I. Katz, *Fundamentals of Electric Propulsion: Ion and Hall Thrusters*, First Edition ed., Joseph H. Yuen, Ed. Pasadena, US, 2008.

[3] Busek Co. Inc.. (n.d.) Hall Effect Thruster Systems. [Online]. http://www.busek.com/halleffect.html

[4] Aerojet.. (n.d.) Spacecraft Propulsion. [Online]. http://www.aerojet.com/capabilities/spacecraft.php

[5] R. Hofer, I. Mikellides and I. Katz, "BPT-4000 Hall Thruster Discharge Chamber Erosion Model Comparison With Qualification Life Test Data," IEPC -2007- 267, *30th International Electric Propulsion Conference*, Florence, Sep 2007.

[6] R. G. Jahn, *Physics of Electric Propulsion,* First ed. New York, NY: McGraw Hill, 1968.

[7] W. A. Hargus, " Investigation of the Plasma Acceleration Mechanism Within a Coaxial Hall Thruster," Stanford University, Palo Altos, PhD Dissertation 2001.

[8] Princeton Plasma Physics Lab (n.d.) What,,s a Hall Thruster? [Online]. http://htx.pppl.gov/ht.html

[9] J. E. Rotter, "An Analysis of Multiple Configurations of Next Generation Cathodes in a Low Power Hall Thruster," Air Force Institute of Technology, Dayton, Thesis AFIT/GA/ENY/09-M07, 2009.

[10] AP*Tech. (2007, July) High Performance Electron Emitters (LaB6 CeB6). [Online]. http://www.kore.co.uk/aptech.htm

[11] R. Wirz, D. M. Goebel, C. Marrese, and J. Mueller, "Development of Cathode Technologies for a Miniature Ion Thruster," in *39th AIAA/ASME/SAE/ASEE Joint Propulsion Conference and Exhibit*, Huntsville, 2003, pp. 1-11.

[12] Kimball Physics, Inc. (n.d.) Kimball Physics Emitters (Cathodes, Filaments, Ion Sources) Product Guide. [Online]. http://www.kimphys.com/cathode/cath_prod.htm

[13] L. W. Swanson and D. R. McNeely, "Work Functions of the (001) Face of the Hexaborides of Ba, La, Ce, and Sm," *Surface Sciences*, vol. 83, pp. 11-28, 1979.

[14] D.M. Goebel, J.T. Crow and A.T. Forrester, "Lanthanum hexaboride hollow cathode for dense plasma production", *Rev. Sci. Instrum*., 49, p.469 (1978).

[15] M. J. Patterson, "Robust low-Cost Cathode for Commercial Applications," in *43rd AIAA/ASME/SAE/ASEE Joint Propulsion Conference and Exhibit*, Cincinnati, 2007, pp. 1-11.

[16] D. J. Warner, "Advanced Cathodes for Next Generation Electric Propulsion Technology," Air Force Institute of Technology, Dayton, Thesis AFIT/GA/ENY/08-M07, 2008.

[17] M. T. Domonkos, "Evaluation of Low-Current Orificed Hollow Cathodes," University of Michigan, Ann Arbor, PhD Dissertation 1999.

[18] D. M. Goebel, R. M. Watkins, and K. K. Jameson, "LaB6 Hollow Cathodes for Ion and Hall Thrusters," *Journal of Propulsion and Power*, vol. 23, no. 3, pp. 552-558, June 2007.

[19] D.M. Goebel and R. M. Watkins, "LaB6Hollow Cathodes for Ion and Hall Thrusters," IAA-2005-4239, *41st Joint Propulsion Conference*, Tucson, AZ, Jul 2005.

[20] J. E. Polk, D. M. Goebel, R. M. Watkins, K. K. Jameson, L. Yoneshige, J. Przybylowski and L. Cho, "Characterization of Hollow Cathode Performance and Thermal Behavior," *2006 Joint Propulsion Conference*, Sacramento, Arizona, July 9-12, 2006. AIAA-2006-5150

[21] S. Otani and Y. Ishizawa, “Thermionic emission properties of boron-rich LaB6 and CeB6 crystal cathodes,” *Journal of Alloys and Compounds*, vol 245, Issues 1-2, pp. L18-L20, 15 November 1996

[22] P. R. Davis, M. A. Gesley, G. A. Schwind, L. W. Swanson, J. J. Hutta, “Comparison of Thermionic Cathode Parameters of Low Index Single Crystal Faces of LaB6, CeB6, and PrB6” *Oregon Graduate Center*, 8 April 1989.

[23] L. W. Swanson and D. R. McNeely, "Work Functions of the (001) Face of the Hexaborides of Ba, La, Ce, and Sm," *Surface Sciences*, vol. 83, pp. 11-28, 1979.

[24] M. S. McDonald and A. D. Gallimore, "Cathode Positioning and Orientation Effects on Cathode Coupling in a 6-KW Hall Thruster," in *JANNAF 6th Modeling and Simulation/4th Liquid Propulsion/3rd Spacecraft Propulsion Joint Subcommittee Meeting*, Orlando, 2008.

[25] BK. Morgan, "Building of a Laser Diagnostic Tool to Measure the Ion Velocity in a Low Power Hall Thuster," Air Force Institute of Technology, Dayton, Thesis AFIT/GA/ENY/09-M04, 2009.

[26] G. P. Perram, S. J. Cusumano, R, L. Hengehold and S. T. Fiorino, *An Introduction to Laser Weapon Systems*, Directed Energy Professional Society, Albuquerque, US, 2009.

[27] W. Demtroder, *Laser Spectroscopy Basic concepts and Instrumentation*, Third Edition ed. Berlin, Germany: Springer-Verlag, 2003.

[28] W. A. Hargus Jr. and C. S. Charles, "Near Plume Laser Induced Fluorescence Velocity Measurements of a 600 W Hall Thruster," in *44th AIAA/ASME/SAE/ASEE Joint Propulsion Conference & Exhibit*, Hartford, 2008, pp. 1-10.

[29] Oracle Thinkquest Library (n.d.) [Online]. http://library.thinkquest.org/C006669/media/Chem/img/Series.gif

[30] R. D. Cowan, *The Theory of Atomic Structure and Spectra,* University of California Press, Berkley, California, 1981.

[31] H. R. Griem, *Spectral Line Broadening by Plasmas.* Academic Press, New York: *1974.*

[32] W. A Hargus, "Laser-Induced Fluorescence of Neutral Xenon in the NearField of a 200 W Hall Thruster," AIAA-2005-4400, *41st Joint Propulsion Conference*, Tucson, AZ, Jul 2005.

[33] R. W. Humble, G. N. Henry, and W. J. Larson, Eds., *Space Propulsion Analysis and Design*, 1st ed. New York, NY: McGraw Hill, 1995.

[34] PHPK Technologies, CBST 6.0 Scroll Compressor. Columbus, OH: PHPK Technologies/CVI, n.d.

[35] PHPK Technologies, TorrMaster TM500 Cryopump Instruction Manual. Columbus, OH: PHPK Technologies/CVI, n.d.

[36] Kurt J. Lesker Company, 300 Series Convection Vacuum Gauge User's Manual, 114th ed. Clairton, PA: Kurt J. Lesker Company, 2005.

[37] Extorr, Inc., Instruction Manual Extorr XT Series RGA. New Kensington, PA: Extorr, 2006.

[38] Kurt J. Lesker Company, Series 979 Atmosphere to Vacuum Transducer Operation and Maintenance Manual, 100014438th ed. Clairton, PA, 2003.

[39] Busek Co. Inc., BHT-HD-1500 Hall Thruster Operating and Maintenance Manual. Natick, MA: Busek Co. Inc., 2008.

[40] D. Kenan, "Xenon and Krypton Characterization in Satellite Thrusters," Air Force Institute of Technology, Dayton, Thesis AFIT/GAE/ENY/10-M14, 2010.

[41] J. T. Thurman, "Hall Thruster Plume Diagnostics Utilizing Microwave Interferometry," Air Force Institute of Technology, Dayton, Thesis AFIT/GAE/ENY/08-S03, 2008.

[42] Sacher Lasertechnik Group, *User Manual Pilot PC Laser Driver*. Marsburg, Germany: Sacher Lasertechnik Group, 2008.

[43] New Focus. *Users Guide 6000 Vortex Series Tunable Diode Laser*. San Jose: New Focus, 2002.

[44] Thorlabs (n.d.) Fabry-Perot Tutorial [Online]. http://www.thorlabs.com/tutorials.cfm?tabid=21118

[45] Thorlabs, *SA200-Series Scanning Fabry Perot Interferometer*. Newton: Thorlabs, 2005.

[46] Stanford Research Systems, *Model SR830 DSP Lock-in Amplifier*. Sunnyvale: Stanford Research Systems Inc., 1993.

[47] Thorlabs, *DET10A Operating Manual-High Speed Silicon Detector*, 2006.

[48] Jobin Yvon Horiba, *H10, H20 and DH10 Compact Monochromator User Manual*. Edison, NJ: Jobin Yvon Horiba, n.d.

[49] T. Hakamata, *PMT Handbook*, Third ed, Hamamatsu Photonics K.K., 2006.

[50] Stanford Research Systems, *Series PS300 High Voltage Power Supplies*. Sunnyvale: Stanford Research Systems Inc., 1998.

[51] Bristol Instruments, *Model 621 Laser Wavelength Meter User's Manual*, 2007

[52] Stanford Research Systems, *Model SR540 Optical Chopper*. Sunnyvale: Stanford Research Systems Inc., 2005.

[53] National Instrument, *NI-9263 Operating Instructions and Specifications*. Austin: National Instruments Corp., 2007.

[54] National Instruments, *NI-DAQ9172 Operating Instructions and Specifications*. Austin: National Instruments Corp., 2007.

[55] National Instruments, *NI-9215 Operating Instructions and Specifications*. Austin: National Instruments Corp., 2007.

[56] Stanford Research Systems, *Model SR570 Low-Noise Current Preamplifier*. Sunnyvale: Stanford Research Systems Inc., 1997.

[57] Ophir Optronics, *Vega Laser Power/Energy Monitor User Manual*. 2009

[58] Aerotech, *Model SR540 Optical Chopper*. Sunnyvale: Stanford Research Systems Inc., 2005.

[59] *IGOR® Pro version 6.0 Getting Started, Volume I. Lake Oswego*, OR: Wavemetrics Inc., 2007.

[60] E. Hecht, *Optics*, Fourth Edition ed. San Francisco, US: Pearson Education, Inc., 2002.

[61] Wikipedia (n.d.) Lens (Optics) [Online]. http://en.wikipedia.org/wiki/Lens_%28optics%29

[62] W. Huang and A. D. Gallimore, "Laser-induced Fluorescence Study of Neutral Xenon Flow Evolution inside a 6-kW Hall Thruster," IEPC-2009-087, *31st International Electric Propulsion Conference*, Ann Arbor, Sep 2009.

[63] C. Palmer and E. Loewen, *Diffraction Grating Handbook*, 6th Edition, Rochester, NY: New Focus, 2007.

[64] K. C. Harvey and C. J. Myatt, "External-cavity diode laser using a grazing-incidence diffraction grating," *Optics Letters*, vol. 16, pages 910–912, June 1991.

[65] M. G. Littman, "Single-mode operation of grazing-incidence pulsed dye laser," *Optics Letters*, vol. 3, no. 4, pp. 138-140, Oct 1978.

[66] F.J. Duarte, *Tunable Lasers Handbook*, Academic Press Inc., San Diego, California, 1st Edition, 1995.

[67] Molecular Expressions (n.d.) Diode Lasers [Online]. http://www.microscopy.fsu.edu/primer/java/lasers/diodelasers/index.html

[68] Shore Laser (n.d.) Laser Operation [Online]. http://www.shorelaser.com/Laser_Operation.html

[69] E. T. Soisson and G. A. Ruff, (n.d.) Practical Cavity Designs for Tunable Diode Lasers Used in Atom Trapping Experiments [Online]. http://abacus.bates.edu/~gruff/trap03.html

[70] W. Mendenhall and T. Sincich, *Statistics for Engineers and the Sciences*, Prentice-Hall Inc.. Upper Saddle River, NJ, 4th Edition, 1995.

[71] W. A Hargus and C. S. Charles, "Near Exit Plane Velocity Field of a 200W Hall Thruster," AIAA-2003-5154, *39th Joint Propulsion Conference*, Huntsville, AL, Jul 2003.

[72] W. A Hargus and M.R. Nakles, "Ion Velocity Measurements within the Acceleration Channel of a Low Power Hall Thruster," IEPC-2007-172, *30th International Electric Propulsion Conference*, Florence, Sep 2007.

Vita

Captain Daniel Lee graduated from the University of Illinois at Urbana-Champaign in 1998 with a General Engineering Degree. After stints in public service, teaching and working the private telecommunications industry, he entered the United States Air Force and attended Officer Training School at Maxwell AFB, Montgomery, Alabama in 2002.

His first assignment was as a Flight Test Engineer with the 40th Flight Test Squadron at Eglin AFB, Ft Walton Beach, FL, certifying weapon load-outs for the F-16 fighter. In 2006, he was assigned to the 1st Space Operations Squadron at Schriever AFB, Colorado Springs CO as a satellite test engineer.

In 2008, Captain Lee entered AFIT with a follow-on to teach at the United States Air Force Academy, Colorado Springs, CO, for the Department of Astronautics following graduation.

REPORT DOCUMENTATION PAGE

Form Approved
OMB No. 074-0188

PLEASE DO NOT RETURN YOUR FORM TO THE ABOVE ADDRESS.

1. REPORT DATE *(DD-MM-YYYY)*	2. REPORT TYPE	3. DATES COVERED *(From – To)*
17-06-2010	Master's Thesis	August 2008 – June 2010

6. TITLE AND SUBTITLE

Velocity Plume Profiles for Hall Thrusters Using Laser Diagnostic

5a. CONTRACT NUMBER

5b. GRANT NUMBER

5c. PROGRAM ELEMENT NUMBER

7. AUTHOR(S)

Lee, Daniel B., Captain, USAF

5d. PROJECT NUMBER

5e. TASK NUMBER

5f. WORK UNIT NUMBER

7. PERFORMING ORGANIZATION NAMES(S) AND ADDRESS(S)

Air Force Institute of Technology
Graduate School of Engineering and Management (AFIT/ENY)
2950 Hobson Way, Building 640
WPAFB OH 45433-8865

8. PERFORMING ORGANIZATION REPORT NUMBER

AFIT/GA/ENY/10-J01

9. SPONSORING/MONITORING AGENCY NAME(S) AND ADDRESS(ES)

Air Force Research Lab/Space and Missile Propulsion Div.
Att: Mr. Michael Huggins
1 Ara Rd.
Edwards, AFB CA 93524

10. SPONSOR/MONITOR'S ACRONYM(S)
AFRL/RZS

11. SPONSOR/MONITOR'S REPORT NUMBER(S)

12. DISTRIBUTION/AVAILABILITY STATEMENT

APPROVED FOR PUBLIC RELEASE; DISTRIBUTION UNLIMITED

13. SUPPLEMENTARY NOTES

14. ABSTRACT

This research built a non-intrusive laser diagnostic tool using Laser Induced Fluorescence (LIF) and absorption techniques to measure the velocity and density plume profiles of low powered Hall Thrusters. This tool was then applied to a Busek 200W Hall thruster to validate the performance against previous research on the same thruster. A laser frequency sweep through 834.72 nm produced LIF signals for ionized xenon –collected at 541.9 nm – in the thruster plume and absorption data outside the plume at a neutral transition at 834.68 nm. The absorption data provided a baseline reference to calculate the axial and radially velocity of the ions in the thruster plume using the Doppler shift. Initial results compared favorably to published values.

15. SUBJECT TERMS

Space Propulsion, Hall Thrusters, Laser Induced Fluorescence

16. SECURITY CLASSIFICATION OF:			17. LIMITATION OF ABSTRACT	18. NUMBER OF PAGES	19a. NAME OF RESPONSIBLE PERSON
a. REPORT	b. ABSTRACT	c. THIS PAGE			Richard Branam, Lt Col, USAF
U	U	U	UU	133	19b. TELEPHONE NUMBER *(Include area code)* (937) 255-6565, ext 7485 (Richard.branam@afit.edu)

Standard Form 298 (Rev. 8-98)
Prescribed by ANSI Std. Z39-18